Investigation of MPM inaccuracies, contact simulation and robust implementation for geotechnical problems

Gonzalez Acosta, J.L.

DOI
10.4233/uuid:f0be1724-3041-4214-bb7e-7be1c473b17f

Publication date
2020

Document Version
Final published version

Citation (APA)
Gonzalez Acosta, J. L. (2020). *Investigation of MPM inaccuracies, contact simulation and robust implementation for geotechnical problems*. [Dissertation (TU Delft), Delft University of Technology]. https://doi.org/10.4233/uuid:f0be1724-3041-4214-bb7e-7be1c473b17f

Important note
To cite this publication, please use the final published version (if applicable).
Please check the document version above.

INVESTIGATION OF MPM INACCURACIES, CONTACT SIMULATION AND ROBUST IMPLEMENTATION FOR GEOTECHNICAL PROBLEMS

INVESTIGATION OF MPM INACCURACIES, CONTACT SIMULATION AND ROBUST IMPLEMENTATION FOR GEOTECHNICAL PROBLEMS

Dissertation

for the purpose of obtaining the degree of doctor
at Delft University of Technology
by the authority of the Rector Magnificus prof. dr. ir. T.H.J.J. van der Hagen
chair of the Board for Doctorates
to be defended publicly on Tuesday 6 October at 15:00 o'clock

by

José León GONZÁLEZ ACOSTA

Master of Science in Geotechnical Engineering,
Universidad Nacional Autónoma de México, Ciudad de México, México,
born in Ensenada Baja California, México

This dissertation has been approved by the promotors

Composition of the doctoral committee:

Rector Magnificus,	chairperson
Prof. dr. M. A. Hicks,	Delft University of Technology, promotor
Dr. P. J. Vardon,	Delft University of Technology, promotor

Independent members:

Dr. M. Martinelli,	Deltares
Prof. dr. C. E . Augarde,	Durham University, UK
Prof. dr. K. G . Gavin,	Delft University of Technology
Prof. Dr.-Ing J. Grabe,	Technische Universiteit Hamburg, Germany
Prof. dr. ir. C. Vuik,	Delft University of Technology

Keywords: Double mapping, Implicit contact, Landslides, Large-strain simulations, Material point method, Soil-structure interaction, Stress oscillation

Printed by: Gildeprint Drukkerijen - Enschede

Author: José León González Acosta

Cover by: Grazia Tona

Email: J.L.GonzalezAcosta-1@tudelft.nl;lgonzalez.a87@gmail.com

ISBN: 978-94-6366-310-6

An electronic version of this dissertation is available at
http://repository.tudelft.nl/.

To my beloved family and friends

CONTENTS

SUMMARY

The material point method (MPM) is a numerical technique which has been demonstrated to be suitable for simulating numerous mechanical problems, particularly large deformation problems, while conserving mass, momentum and energy. MPM discretises material into points and solves the governing equations on a background mesh which discretises the domain space. The points are able to move through the mesh during the simulation. MPM is an improvement over other well-established numerical techniques, such as the finite element method (FEM), as it is able to simulate large deformations and therefore can simulate mechanical problems from initiation to the final outcome. It has the potential to become the preferred numerical tool to analyse many engineering problems. Nonetheless, it has been demonstrated throughout this thesis that the performance of MPM has often been far from the levels of accuracy desired in order to be considered a reliable technique for providing quantitative analyses for engineering problems. In this thesis, the implicit solution version of MPM has been taken as the starting point to investigate and solve its current main drawbacks, i.e. (i) the lack of accuracy when computing stresses (stress oscillations), and (ii) interaction between bodies, e.g. soil and structures.

The stress oscillation problem is well-known in the MPM community, and is attributed mostly to material points crossing background cell boundaries, termed the cell-crossing problem. It has been shown in this thesis that cell-crossing is indeed one of the primary sources of oscillation. However, there are also other aspects contributing to the observed inaccuracies. In the literature, cell-crossing has been addressed by creating a particle domain, e.g. in the generalised interpolated material point (GIMP) method. It has been shown in this thesis that major problems also include (i) the use of linear shape function (SF) gradients to calculate (material point) strains and (ii) non-Gauss numerical quadrature to integrate material stiffness. The integration is made worse when using GIMP. In order to reduce the inaccuracies caused by integration a double mapping (DM) technique has been developed, which reduces the errors when integrating nodal stiffnesses. This is shown to also work well with GIMP (DM-G method). Additionally, DM has been combined with a Lagrangian interpolation technique, which uses a larger solution domain (through the combination of background cells to form patches) to enhance the stresses computed at the material points (DM-C or DM-GC methods). The developed methods have been able to significantly improve the accuracy and stability of the simulated problems. This improvement will allow more robust use of more advanced constitutive models.

The interaction of bodies is of benefit in large deformation simulations, although MPM can roughly simulate contact without special treatment. An MPM contact algorithm was initially proposed by other researchers for explicit time integration schemes, but no method was available for the implicit time integration scheme. An implicit contact scheme has been developed based on the original (explicit) contact formulation in order to calculate the change of nodal velocity during the Newton–Raphson iterative procedure.

The results obtained with this contact methodology are shown to be as accurate as those computed using the explicit scheme, although generally with a larger time step. Additionally, it has been observed that, in most of the cases, implicit contact simulations are analysed faster than explicit simulations. However, the contact loads computed with this technique and the internal forces developed are inconsistent (i.e. not equal), reducing the energy conservation and remains an issue to be solved. An analysis of the problem is presented as a first step towards a solution. One challenge is that any method using consistent contact and internal forces is sensitive to stress oscillations, which can lead to highly unrealistic contact forces.

Using the improvements developed in this thesis (i.e. DM-GC combined with the contact algorithm), soil-structure interaction problems and landslides have been successfully simulated. Incorporating the contact algorithm into the model has allowed the simulation of complex failure mechanism development during slope failure. The impact on neighbouring structures was realistic, and captured expected behaviours such as the sliding and rotation of the rigid elements.

It has been demonstrated that (i) the accuracy in MPM has been improved via the combination of several (existing and novel) techniques, (ii) techniques developed for the explicit scheme (or other numerical methods) can be converted and introduced in implicit MPM, maintaining as much as possible the consistency of the formulation, and (iii) by improving diverse aspects of the formulation, more realistic simulations can be obtained. The work presented in this thesis makes several steps contributing to the improvement of MPM, which will lead towards it being used in engineering practice.

SAMENVATTING

De materiaal punt methode (MPM) is een numerieke methode die geschikt is voor het simuleren van verschillende mechanische problemen, in het bijzonder problemen met grote vervormingen. Hierbij worden massa, moment en energie behouden. MPM verdeelt materiaal over punten en lost de differentiaalvergelijkingen op met een rooster van achtergrondelementen, die het domein van de simulatie voorstelt. De punten bewegen door het rooster gedurende een simulatie. In tegenstelling tot gerenommeerde numerieke methodes, zoals de eindige elementen methode (EEM), kunnen met MPM grote vervormingen gesimuleerd worden. Dit biedt de mogelijkheid mechanische problemen van begin tot eind te onderzoeken, waardoor MPM de voorkeursmethode zou kunnen zijn voor de analyse van vele (civiel-)technische problemen. Desondanks is in dit proefschrift herhaaldelijk aangetoond dat de nauwkeurigheid van MPM in veel gevallen ondermaats is om een betrouwbare methode voor kwantitatieve analyses te zijn. In dit proefschrift is MPM met een impliciet oplossingsschema gebruikt als basis voor het onderzoeken en oplossen van (op dit moment) belangrijke nadelen van MPM, namelijk (i) een gebrek aan nauwkeurigheid in de spanningsberekeningen (spanningsoscillaties) en (ii) het niet kunnen simuleren van interactie tussen lichamen, bijvoorbeeld ondergrond en constructies.

Spanningsoscillaties zijn een bekend fenomeen in het MPM werkveld, en worden voornamelijk toegekend aan materiaal punten die de grens van een achtergrondelement overschrijden. Dit probleem wordt ook wel 'cell-crossing' genoemd. In dit proefschrift is aangetoond dat cell-crossing inderdaad één van de primaire oorzaken van oscillaties is, die in literatuur wordt opgelost door het gebruik van een materiaal punt domein, bijvoorbeeld in de 'gegeneraliseerde interpolatie materiaal punt' (GIMP) methode. Dit proefschrift presenteert echter twee andere oorzaken van oscillaties, namelijk (i) het gebruik van afgeleides van lineaire interpolatie functies (SF) voor de berekening van rek (in materiaal punten) en (ii) niet-Gauss numerieke integratie van materiaal stijfheid. De integratie van materiaal stijfheid verslechtert wanneer GIMP wordt gebruikt. Een dubbele interpolatie (DM) techniek is ontwikkeld om de fouten die ontstaan bij integratie van stijfheid te verminderen. Deze techniek werkt goed samen met GIMP (DM-G methode). Daarnaast is DM gecombineerd met een Lagrangiaanse interpolatie techniek die een groter domein gebruikt (door het combineren van achtergrond elementen) om de nauwkeurigheid van spanningsberekeningen te vergroten (DM-C or DM-GC methodes). De ontwikkelde methodes hebben de nauwkeurigheid en stabiliteit van de uitgevoerde simulaties significant vergroot en deze verbetering maakt het mogelijk om meer geavanceerde constitutieve modellen te gebruiken in MPM.

De interactie tussen lichamen is belangrijk in simulaties met grote vervormingen. MPM kan interacties tussen lichamen in de basis simuleren, maar voor ingewikkelde of meer preciese interacties moeten speciale methodes ontwikkeld worden. In de literatuur is een interactie methode voor MPM met een expliciet oplossingsschema beschreven.

Op basis van deze methode is in dit proefschrift een interactie methode voor het impliciete oplossingsschema ontwikkeld, waarin de snelheidsverandering van knooppunten van het achtergrondrooster wordt berekend gedurende een iteratieve Newton-Raphson procedure. Testresultaten laten zien dat de nauwkeurigheid van deze nieuwe methode overeenkomt met die van het expliciete oplossingsschema. Daarnaast is de benodigde simulatietijd van de impliciete interactie simulaties over het algemeen korter dan de expliciete simulaties. Echter, de interactie krachten berekend in deze methode zijn inconsistent met de interne krachten waardoor energie niet altijd behouden is. Dit probleem is nog niet opgelost, maar de gepresenteerde analyse van het probleem is de eerste stap naar een oplossing. Een uitdaging voor de ontwikkeling van een methode met consistente interactie en interne krachten, is dat deze methode sensitief is voor spanningsoscillaties, waardoor onrealistisch hoge interactie krachten berekend kunnen worden.

Met de ontwikkelingen uit dit proefschrift (DM-GC gecombineerd met de interactie methode) zijn succesvolle simulaties gedaan van grond-constructie interacties en aardverschuivingen. De toevoeging van de interactie methode in DM-GC maakt het mogelijk om complexe faalmechanismes tijdens afschuivingen te simuleren. De impact op nabijgelegen gebouwen beschreef verwacht gedrag, zoals schuiven en roteren van stijve elementen.

Het is aangetoond dat (i) de nauwkeurigheid van MPM is verbeterd door een combinatie van verschillende (bestaande en nieuwe) technieken, (ii) technieken ontwikkeld voor het expliciete oplossingsschema (of andere numerieke methodes) aangepast kunnen worden voor introductie in MPM met een impliciet oplossingsschema, waarbij de formulatie (zoveel mogelijk) consistent blijft, en (iii) door verbetering van diverse aspecten van MPM, meer realistische simulaties verkregen kunnen worden.

Het werk gepresenteerd in dit proefschrift maakt meerdere stappen in de verdere ontwikkeling van MPM, wat er toe leidt dat MPM uiteindelijk ook in de praktijk kan worden gebruikt.

LIST OF FIGURES

1

INTRODUCTION

Part of the inhumanity of the computer is that, once it is competently programmed and working smoothly, it is completely honest.

Isaac Asimov

1

1.1. NUMERICAL METHODS IN SCIENCE AND ENGINEERING

In the early days, the design of structures was based on experience rather than a concrete knowledge of equilibrium and failure mechanisms. As expected, this commonly leads to oversized structures or, in the worst case scenario, to inadequate designs causing failure. It was not until the 18th century that the first work on theoretical soil mechanics was conceived (Coulomb, 1773). In that work, an introduction to limit equilibrium theory was developed, in which the now well-known concepts of active and passive pressure (Rankine, 1857) were presented. Later, during the 20th century, the treatment of the soil as an engineering material began with the publication of *Erdbaumechanik auf Bodenphysikalischer* (Terzaghi, 1925), where the mechanical behaviour of soils was presented, and in which the knowledge of geology, geophysics and the theory of elasticity was considered. It can be stated that this is the point in which Geotechnical Engineering was born. After Terzaghi, many other researchers contributed to the development of geotechnical engineering, such as Arthur Casagrande (who contributed numerous works on apparatus and testing techniques for soils), Alec Westley Skempton (who performed numerous studies on the consolidation and residual strength of clays), and Harry Bolton Seed (pioneer in the field of Geotechnical Earthquake Engineering). With the increase in geotechnical knowledge, the level of confidence also grew, allowing the building of larger structures. Nevertheless, the complexity of the structures reached a point in which hand calculations were not feasible, and more sophisticated and faster solutions were needed.

Then, starting from the late 1940s, with the appearance of the first computers, and later between the late 1960s and the early 1980s, with the appearance of the personal computer, the possibility of performing large numbers of computations was possible. The implementation of numerical techniques, such as those developed by Newton, Euler, and Gauss, to study and solve engineering problems was also possible. It was at this time when techniques such as the Finite Element Method (FEM), the Finite Difference Method (FDM), and the Finite Volume Method (FVM), were born. Identifying the first implementation of such techniques using computers is rather difficult, but some of the early works using FEM, FDM and FVM can be traced to Courant *et al.* (1943), Turner *et al.* (1956), Synge (1957), Argyris & Kelsey (1960), Forsythe & Wasow (1960), Richtmyer & Dill (1959), Collatz (1960), McDonald (1971) and Samarskii (1965). Each one of these methods has its own advantages with respect to another, and much interesting research was produced. Among these techniques, FEM is generally the most used in civil engineering, due to its robustness, and is the one that will be taken as a reference in the following chapters, since the material point method (MPM) shares the same continuum mechanics background as FEM.

1.2. NUMERICAL METHODS FOR LARGE DEFORMATIONS

FEM is nowadays the most used numerical technique and its use extends to a large number of problems in every branch of engineering. Nevertheless, FEM is far from being perfect and suffers from several limitations (as does every numerical technique developed so far). The main limitation in FEM (which has prompted new developments, including the one studied in this thesis) is the necessity of using elements to simulate the geometry of the problem analysed. The elements are attached to each other at fixed points, or nodes,

and without special treatments are unable to separate or handle large deformations. Due to this inconvenience, the range of engineering problems that can be solved using FEM is constrained, and new techniques are needed.

One of the first solutions proposed to simulate large deformation problems was to combine the Lagrangian method (in which each individual node of the computational mesh follows the associated material particle during motion) and the Eulerian method (in which the computational mesh is fixed and the continuum moves with respect to the grid) into one technique, that would later be called the Arbitrary Lagrangian-Eulerian (ALE) method. Some of the initial work using ALE can be found in Noh (1963), Franck & Lazarus (1964), and Trulio (1966). Later, this method was used in the FEM context to simulate mechanical problems (e.g. Belytschko & Kennedy 1978, Belytschko *et al.* 1982, Ghosh & Kikuchi 1991, Nazem *et al.* 2009). Unfortunately, the ALE method has not become widely adopted, mainly due to its complexity.

Another family of (continuum and non-continuum) methods formulated to simulate large deformations are those based on the use of particles to discretise the material domain. Some of these techniques are:

- The Particle Finite Element Method (PFEM) (Idelsohn *et al.* 2004, Oñate *et al.* 2004), which can be seen as an FEM technique with a re-meshing step. In this technique, the FEM elements which have suffered severe distortion are rebuilt, keeping the elements as undistorted as possible. This technique is relatively easy to implement since all FEM developments are already included in PFEM. Some examples of the implementation and accuracy of the PFEM can be found in Aubry *et al.* (2005), Idelsohn *et al.* (2006), Carbonell *et al.* (2009), and Papakrivopoulos (2018);

- The Smoothed Particle Hydrodynamics (SPH) method (Lucy 1977, Gingold & Monaghan 1977) and the Vortex Method (Chorin 1973) which are two particle techniques known as "meshless"methods. This is because structured meshes are not used, and the differential equations are solved through the use of radial or polynomial basis functions;

- The Discrete Element Method (DEM) (Cundall & Strack 1979), a powerful technique which can consider the geometry of particles (Chang 1992, Tavarez & Plesha 2007). Nevertheless, implementing DEM is not as straightforward as the other large deformation techniques. Its main disadvantage is the difficulty in approximating the real shape of the particles, especially when particles have sharp edges or large aspect ratios. Additionally, the computational cost when such geometries are simulated grows markedly, making DEM almost infeasible.

Finally, a particle technique which has gained particular recognition due to its simplicity and robustness is the material point method (MPM). MPM is the evolution of two particle techniques, the Particle-in-Cell (PIC) method (Buneman 1959, Dawson 1962, Harlow 1964), and the FLuid Implicit Particle (FLIP) method (Brackbill & Ruppel 1986, Brackbill *et al.* 1988). MPM (Sulsky *et al.* 1994, Sulsky *et al.* 1995) is a fully Lagrangian particle method which utilizes the advantages of both Eulerian and Lagrangian methods. Compared with Eulerian methods, the numerical dissipation normally associated with the Eulerian approach is reduced, while the complete deformation history of material

points is tracked. Unlike Lagrangian methods, excessive mesh distortion and element entanglement are avoided by restoring the background mesh to its original position at the end of each computational step. Therefore, MPM has obvious advantages in tackling extreme events such as impact, blast, penetration, perforation, machining, fragmentation, and multi-phase interaction involving failure evolution (Zhang *et al.* 2016).

The use of MPM has been growing over the last fifteen years (Fern *et al.* 2019). Many of the developments which have been implemented in other numerical techniques have been successfully reproduced in MPM, such as multi-phase material behaviour, contact simulation using Lagrangian multipliers, regularization techniques, etc. Moreover, with the continuous growth of computational power of the new computers, the use of fine unstructured meshes is becoming feasible. Unfortunately, due to the lack of computers able to handle a large number of calculations rapidly, techniques capable of ensuring the accuracy of the results without the need of refining the computational mesh or increasing the number of material points are needed. Some of these techniques are the generalized interpolation material point (GIMP) method (Bardenhagen & Kober 2004), the convected particle domain interpolation (CPDI) method (Sadeghirad *et al.* 2011), and the B-Spline MPM (Steffen *et al.* 2008), which can significantly improved the accuracy of MPM. Nonetheless, most MPM developments still use the explicit scheme, which has numerous disadvantages compared to the implicit scheme. In this thesis, the work of Wang *et al.* (2016), an implicit version of MPM, is taken as the starting point for the developments here elaborated.

1.3. AIMS AND OBJECTIVES

The aims of this thesis are to study, and mitigate for, numerical inaccuracies occurring in MPM, to develop novel contact techniques, and to apply the developed techniques to practical problems in geotechnical engineering. This is achieved by combining new and existing techniques in MPM. In detail, this thesis is focused on:

- Studying the causes of stress oscillations. To date, most of the inaccuracies in MPM are attributed to the jumping of material points between elements. Nonetheless, an exhaustive study dedicated to this problem has not been done;
- Studying the use of mapping techniques. These mapping techniques will be focused on oscillation problems; in particular, for implicit solution schemes, in which the stiffness matrix also contributes to the inaccuracy of the results;
- The development of a methodology to simulate contact using the implicit scheme. To date, existing solutions have mainly been developed for the explicit scheme; implementation and testing for implicit schemes is needed;
- Studying the use of MPM to simulate soil-structure interaction problems. In particular, the collision of a vertical cutting against a retaining wall and the penetration of a rigid footing into a cohesive soil will be investigated;
- The study of landslides.

1.4. OUTLINE

The outline of the remainder of this thesis is as follows:

- Chapter 2: Elaborates the MPM background. The formulations of the static, explicit and implicit MPM are delineated. The algorithm for each solution scheme is given, and the accuracy of each technique is tested against several benchmark problems;
- Chapter 3: Elaborates on the inaccuracies in MPM, particularly stress and stiffness inaccuracies (oscillation), and their elimination or reduction. A description of the causes of such oscillations is given, and a series of benchmarks are introduced to measure the oscillations. A combination of mapping procedures and a high order interpolation technique is used to reduce the oscillations. Finally, insights into the implementation of this new oscillation reduction technique and its computational performance are given;
- Chapter 4: Elaborates on the developments required to simulate contact in the implicit scheme. Existing formulations for the explicit scheme are used as the basis. Then, a number of benchmarks are introduced to validate the implicit contact algorithm. Finally, the implicit contact solution is tested against two geotechnical problems;
- Chapter 5: Demonstrates the applicability of implicit MPM to solve geotechnical problems. In particular, the simulation of a landslide triggered by construction procedures is studied;
- Chapter 6: Summarises the main conclusions of the thesis and gives recommendations for further research.

REFERENCES

Argyris, J. H. & Kelsey, S. (1960). *Energy theorems and structural analysis*. Springer US.

Aubry, R., Idelsohn, S. & Onate, E. (2005). Particle finite element method in fluid-mechanics including thermal convection-diffusion. *Computers & Structures* **83**, No. 17-18, 1459–1475.

Bardenhagen, S. G. & Kober, E. M. (2004). The generalized interpolation material point method. *Computer Modeling in Engineering and Sciences* **5**, No. 6, 477–496.

Belytschko, T., Flanagan, D. & Kennedy, J. (1982). Finite element methods with user-controlled meshes for fluid-structure interaction. *Computer Methods in Applied Mechanics and Engineering* **33**, No. 1-3, 669–688.

Belytschko, T. & Kennedy, J. M. (1978). Computer models for subassembly simulation. *Nuclear Engineering and Design* **49**, No. 1-2, 17–38.

Brackbill, J. U., Kothe, D. B. & Ruppel, H. M. (1988). Flip: a low-dissipation, particle-in-cell method for fluid flow. *Computer Physics Communications* **48**, No. 1, 25–38.

Brackbill, J. U. & Ruppel, H. M. (1986). Flip: A method for adaptively zoned, particle-in-cell calculations of fluid flows in two dimensions. *Journal of Computational Physics* **65**, No. 2, 314–343.

Buneman, O. (1959). Dissipation of currents in ionized media. *Physical Review* **115**, No. 3, 503–517.

Carbonell, J. M., Oñate, E. & Suárez, B. (2009). Modeling of ground excavation with the particle finite-element method. *Journal of Engineering Mechanics* **136**, No. 4, 455–463.

Chang, C. S. (1992). Discrete element method for slope stability analysis. *Journal of Geotechnical Engineering* **118**, No. 12, 1889–1905.

Chorin, A. J. (1973). Numerical study of slightly viscous flow. *Journal of Fluid Mechanics* **57**, No. 4, 785–796.

Collatz, L. (1960). *The numerical treatment of differential equations*. Springer-Verlag Berlin Heidelberg.

Coulomb, A. (1773). Essay on the application of the rules of maxima and minima to certain statics problems relavant to architecture. *Memoires presentes a l'Academie* , 343–384.

Courant, R. *et al.* (1943). Variational methods for the solution of problems of equilibrium and vibrations. *Bulletin of the American Mathematical Society* **49**, No. 1, 1–23.

Cundall, P. A. & Strack, O. D. (1979). A discrete numerical model for granular assemblies. *Géotechnique* **29**, No. 1, 47–65.

Dawson, J. (1962). One-dimensional plasma model. *The Physics of Fluids* **5**, No. 4, 445–459.

Fern, J., Rohe, A., Soga, K. & Alonso, E. (2019). *The material point method for geotechnical engineering: a practical guide*. CRC Press.

Forsythe, G. E. & Wasow, W. R. (1960). *Finite-difference methods for partial differential equations*. John Wiley & Sons.

Franck, R. M. & Lazarus, R. B. (1964). Mixed Eulerian-Lagrangian method. *Methods in Computational Physics* **3**, 47–67.

Ghosh, S. & Kikuchi, N. (1991). An arbitrary Lagrangian-Eulerian finite element method for large deformation analysis of elastic-viscoplastic solids. *Computer Methods in Applied Mechanics and Engineering* **86**, No. 2, 127–188.

Gingold, R. A. & Monaghan, J. J. (1977). Smoothed particle hydrodynamics: theory and application to non-spherical stars. *Monthly Notices of the Royal Astronomical Society* **181**, No. 3, 375–389.

Harlow, F. H. (1964). The particle-in-cell computing method for fluid dynamics. *Methods in Computational Physics* **3**, 319–343.

Idelsohn, S. R., Oñate, E. & Del Pin, F. (2004). The particle finite element method: a powerful tool to solve incompressible flows with free-surfaces and breaking waves. *International Journal for Numerical Methods in Engineering* **61**, No. 7, 964–989.

Idelsohn, S. R., Oñate, E., Del Pin, F. & Calvo, N. (2006). Fluid-structure interaction using the particle finite element method. *Computer Methods in Applied Mechanics and Engineering* **195**, No. 17-18, 2100–2123.

Lucy, L. B. (1977). A numerical approach to the testing of the fission hypothesis. *The Astronomical Journal* **82**, 1013–1024.

McDonald, P. (1971). The computation of transonic flow through two-dimensional gas turbine cascades. In *ASME paper*, American Society of Mechanical Engineers, pp. 71–GT–89.

Nazem, M., Carter, J. P. & Airey, D. W. (2009). Arbitrary Lagrangian–Eulerian method for dynamic analysis of geotechnical problems. *Computers and Geotechnics* **36**, No. 4, 549–557.

Noh, W. F. (1963). CEL: A time-dependent, two-space-dimensional, coupled Eulerian-Lagrange code. *Technical report*, Lawrence Radiation Lab., University of California, Livermore.

Oñate, E., Idelsohn, S. R., Del Pin, F. & Aubry, R. (2004). The particle finite element method—an overview. *International Journal of Computational Methods* **1**, No. 02, 267–307.

Papakrivopoulos, V. (2018). *Development and preliminary evaluation of the main features of the particle finite element method (PFEM) for solid mechanics*. M.Sc. thesis, Delft University of Technology.

Rankine, W. J. M. (1857). On the stability of loose earth. *Philosophical Transactions of the Royal Society of London* , No. 147, 9–27.

Richtmyer, R. D. & Dill, E. (1959). Difference methods for initial-value problems. *Physics Today* **12**, 50.

Sadeghirad, A., Brannon, R. M. & Burghardt, J. (2011). A convected particle domain interpolation technique to extend applicability of the material point method for problems involving massive deformations. *International Journal for numerical methods in Engineering* **86**, No. 12, 1435–1456.

Samarskii, A. A. (1965). Monotonic difference schemes for elliptic and parabolic equations in the case of a non-self adjoint elliptic operator. *USSR Computational Mathematics and Mathematical Physics* **5**, No. 3, 212–217.

Steffen, M., Kirby, R. M. & Berzins, M. (2008). Analysis and reduction of quadrature errors in the material point method (MPM). *International Journal for Numerical Methods in Engineering* **76**, No. 6, 922–948.

Sulsky, D., Chen, Z. & Schreyer, H. L. (1994). A particle method for history-dependent materials. *Computer Methods in Applied Mechanics and Engineering* **118**, No. 1-2, 179–196.

Sulsky, D., Zhou, S.-J. & Schreyer, H. L. (1995). Application of a particle-in-cell method to solid mechanics. *Computer Physics Communications* **87**, No. 1-2, 236–252.

Synge, J. (1957). *The hypercircle in mathematical physics: A method for the approximate solution of boundary value problems*. Cambridge University Press.

Tavarez, F. A. & Plesha, M. E. (2007). Discrete element method for modelling solid and particulate materials. *International Journal for Numerical Methods in Engineering* **70**, No. 4, 379–404.

Terzaghi, K. (1925). *Erdbaumechanik auf bodenphysikalischer grundlage*. F. Deuticke.

Trulio, J. G. (1966). Theory and structure of the afton codes. *Technical report*, Nortronics Newbury Park CA.

Turner, M. J., Clough, R. W., Martin, H. C. & Topp, L. (1956). Stiffness and deflection analysis of complex structures. *Journal of the Aeronautical Sciences* **23**, No. 9, 805–823.

Wang, B., Vardon, P. J., Hicks, M. A. & Chen, Z. (2016). Development of an implicit material point method for geotechnical applications. *Computers and Geotechnics* **71**, 159–167.

Zhang, X., Chen, Z. & Liu, Y. (2016). *The material point method: a continuum-based particle method for extreme loading cases*. Academic Press.

2

MPM Background

The derivation of the explicit, static and implicit dynamic MPM equations is presented. The algorithmic procedures followed in a typical MPM code are presented, and a number of benchmark problems are introduced to demonstrate the accuracy and advantages of using MPM.

2.1. INTRODUCTION

During the late 1950s and early 1960s, the Particle-in-Cell (PIC) method was developed (Harlow *et al.* 1956; Harlow 1957, 1964), in which the advantages of grid and particle methods were combined for fluid mechanics problems. In this method (and the methods developed later), particles are used to carry some transported variables whereas the mesh is used to solve the equilibrium equations. Since the original PIC method was not fully Lagrangian (because some information was stored in the particles and other information in the element nodes) the FLuid Implicit Particle (FLIP) method was developed (Brackbill & Ruppel 1986, Brackbill *et al.* 1988). In the FLIP method, the particles carry all the information related to the fluid. As a consequence of this change, the FLIP maintained the advantages of the original PIC but eliminated the major source of numerical inaccuracies. Later, due to the necessity of including history-dependent effects (such as stresses and plastic strains in the simulations), MPM was developed. MPM (Sulsky *et al.* 1994, Sulsky *et al.* 1995) is a method in which the mechanical framework is similar to the FEM. In MPM, two discretisations are implemented: one is a finite element (FE) mesh covering the entire computational space (whereas in FEM the mesh models the shape of the structure), and the other is a set of (material) points, which discretises the body (or bodies) analysed. The mesh covering the computational space is used to solve the equation of equilibrium (in term of accelerations, velocities or displacements). The material points perform the same role as FEM Gauss integration points, i.e. stress/strain recovery and integration to form nodal equations, while carrying state variables of the bodies throughout the simulation, e.g. kinematics, stresses, properties. At this point, MPM and FEM characteristics are almost the same. Nevertheless, since in MPM all variables are stored at the (material) points, it is possible to reset the FE mesh to its original position to avoid large mesh distortions, and, using the data stored in the points and their new positions, a new solution step (i.e. set of equations) can be formed. This MPM attribute allows the material points to move large distances through the mesh (due to the accumulation of relatively small displacements every solution step), making possible the solution of a large variety of problems. Besides simulating large deformations, MPM also has the following advantages:

- Since MPM is formulated similarly as FEM, the majority of methods developed in FEM can be easily included in MPM;
- It allows the use of several constitutive relations;
- Due to the partition of unity property of the shape functions (SFs), the conservation of mass is guaranteed;
- It allows the use of multiple bodies which can interact via contact conditions.

It has been demonstrated that MPM can be used to simulate and study a large variety of problems. As an example, MPM has been used in computer graphics (Stomakhin *et al.* 2013), aerospace (Gao *et al.* 2018, Mason *et al.* 2014), and medicine (Chong *et al.* 2017) professions to simulate snow, fluid sediment mixture flow, gas flows at high speeds, and body injuries. Regarding geomechanical implementations, MPM has been used to simulate slope stability problems and landslides (Beuth *et al.* 2008, Andersen & Andersen 2010, Mast *et al.* 2014, Soga *et al.* 2015, Alonso *et al.* 2015, Bandara & Soga 2015, Wang *et al.*

2016a, González Acosta *et al.* 2018, Woo & Salgado 2018, Müller & Vargas 2019), shallow foundation problems (Sołowski & Sloan 2015), anchor pull-out (Coetzee *et al.* 2005), hydro-geotechnical problems (Abe *et al.* 2013, González Acosta *et al.* 2019), tunnelling excavation (Cheng *et al.* 2015, Fern 2019) and pile installation (Phuong *et al.* 2016, Lorenzo *et al.* 2017), as well as many more applications.

2.2. MPM DISCRETISATION AND COMPUTATIONAL STEPS

To demonstrate the implementation of MPM, two examples are used. The first example illustrates the discretisation used in MPM (Figure 2.1) and the second illustrates the solution steps (Figure 2.2). Figure 2.1a shows two structural elements (bodies), i.e. a foundation lying on the soil surface. It is seen that, when FEM is used (Figure 2.1b), the mesh discretises both structural elements, which interact through common nodes. In contrast, using MPM (Figure 2.1c), the mesh covers the entire computational space in which the bodies are able to move and interact, and the material points discretise the bodies. Since equilibrium is computed at the nodes, the interaction between the bodies is still occurring at some common nodes (as in FEM), but they must be updated every solution step.

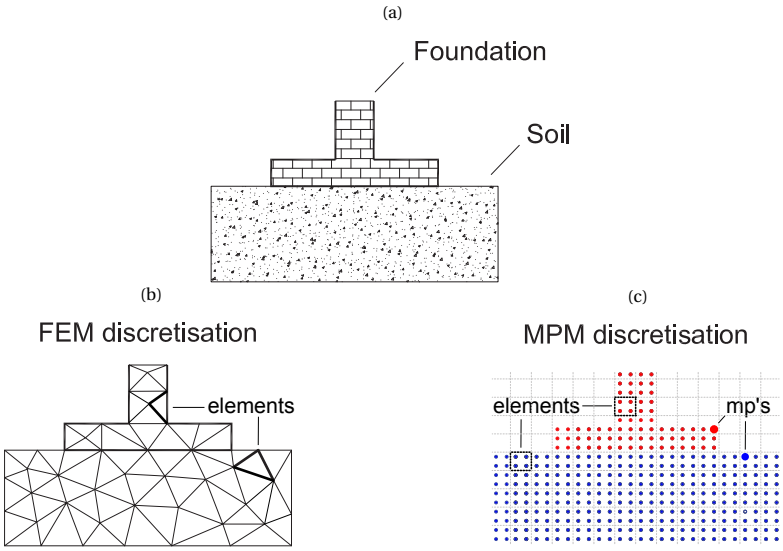

Figure 2.1: a) Example geotechnical problem, b) FEM discretisation, and c) MPM discretisation

Next, the solution steps followed in typical FEM and MPM are studied using a beam fixed at the left end and carrying a load at the right end. Figure 2.2 shows the beam deformation after one step in the analysis using FEM and MPM. The red crosses inside each mesh element represent the (FEM) Gauss integration points and the (MPM) material points. Additionally, the shaded elements indicate the activated elements used for calculations when the MPM scheme is used. Figures 2.2a and 2.2b show the initial phase, in which the values from the Gauss or material point are integrated to form nodal equations. Since external loads (or tractions) are also part of material point information, they should be placed at the nodes via SFs. After nodal integration, a solution phase is performed (Figures 2.2c and 2.2d). In this step, the nodes move (or elements deform) due to the external loads and the increment of internal forces. This movement reduces as the internal forces equilibrate the external loads, and equilibrium is reached when the deformations are small enough. The elements around the beam are highly stretched (when using MPM), but this is not a problem, since these elements are not part of the solution and they do not contribute to the updating of material point internal variables.

At this point, MPM is identical to FEM; the same steps have been followed and the same solution has been obtained. In Figures 2.2e and 2.2f, equilibrium has been reached, and the next load increment must be applied. When using FEM, the next load increment can be applied immediately since the Gauss point variables and the mesh nodes remain unchanged after equilibrium. On the other hand, when using MPM, an intermediate step is performed, in which the material point variables (e.g. position, velocity, acceleration) are updated, followed by the restoration of the mesh to its original position. Since the mesh is restored, the material points end up inside a new set of elements, and an activation procedure is initiated, in which the new set of elements are activated, including their nodal connectivity and boundary conditions. After these steps, the next load increment can be applied and the new solution can be computed. In Figure 2.2f, the activated elements make up an irregular shape, no longer resembling or representing the shape of the beam. Therefore, using this new arrangement of active elements to compute the beam response can cause numerical inaccuracies, but this problem will be discussed later.

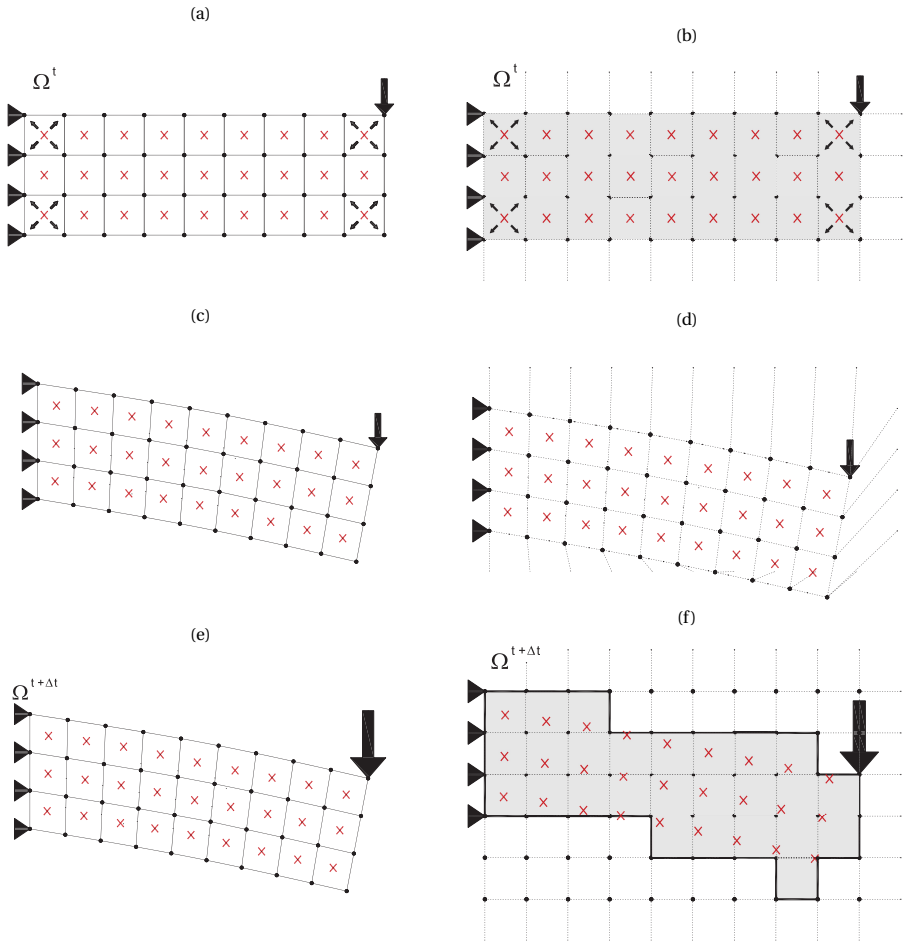

Figure 2.2: a) FEM integration phase, b) MPM integration phase, c) FEM solution phase, d) MPM solution phase, e) next FEM solution step, and f) MPM convection (upgrade) phase

2.3. MPM FORMULATION

The solution to the equation of equilibrium using MPM (or FEM) can be achieved using the explicit scheme (in terms of nodal accelerations) or the implicit scheme (in terms of nodal displacements). The implicit scheme is known to be unconditionally stable and has no restriction on the time step other than that required for accuracy. The explicit approach, on the other hand, is known for being conditionally stable, which means that a small time step is needed to maintain the accuracy of the solution (Lindgren & Edberg, 1990).

The explicit scheme is the most used in MPM, since it is relatively easy to implement. The implicit scheme is not as developed as the explicit scheme despite its advantages; mainly due to the construction and storage of large matrices, which (i) adds complexity to its implementation and (ii) increases the computational time during the solution step.

The static scheme which is also relatively frequently used, is also an implicit scheme, but, in this case, the accelerations are excluded from the formulation, which means that the kinematics are not part of the solution.

In this chapter, the formulation of each MPM scheme is presented (for a single body). First, the explicit formulation is elaborated followed by the implicit formulation. The conservation properties of the implicit MPM are presented. A summary of the algorithm for each technique is added to illustrate the structure of the codes used. In order to demonstrate the performance of the MPM formulations, three benchmark problems are simulated and compared to analytical solutions or the Updated Lagrangian FEM (UL-FEM), which is a version of FEM that formulates the discrete equations in the current nodal configuration (i.e. the position of nodes is updated after each solution step). Note that the formulation presented is limited to small strains, although large displacements are allowed. For a detailed elaboration of the equations, the reader is directed to Bathe (2006), Belytschko *et al.* (2013), Sulsky *et al.* (1995), Wang *et al.* (2016b), and González Acosta *et al.* (2020).

2.3.1. EXPLICIT MPM

The equations of mass and momentum conservation are

$$\frac{d\rho}{dt} + \rho\nabla\cdot\mathbf{v} = 0 \tag{2.1}$$

$$\rho\mathbf{a} = \nabla\cdot\boldsymbol{\sigma} + \rho\mathbf{b} \tag{2.2}$$

where ρ is the mass density, $\mathbf{v}$ is the velocity vector, t is time, $\mathbf{a}$ is the acceleration vector, $\boldsymbol{\sigma}$ is the Cauchy stress tensor, $\mathbf{b}$ is the body force (which in this case accounts only for gravity), and $\nabla\cdot$ denotes the divergence of a vector. Besides the conservation laws, stress-strain laws should hold. Considering small-strain theory, the strain increment computed from the velocities, and the resulting stresses, are given as

$$d\boldsymbol{\epsilon} = \frac{1}{2}\left(\nabla\mathbf{v} + \nabla\mathbf{v}^{T}\right)dt \tag{2.3}$$

$$d\boldsymbol{\sigma} = \mathbf{D}d\boldsymbol{\epsilon} \tag{2.4}$$

where $\boldsymbol{\epsilon}$ represents the strain increment vector, ∇ indicates the gradient operator, and $\mathbf{D}$ is the material elastic matrix. Furthermore, the total strain increment ($\boldsymbol{\epsilon}$) can be divided into two parts for non-linear material behaviour; the elastic increment and the plastic increment (i.e. $\boldsymbol{\epsilon} = \boldsymbol{\epsilon}^{e} + \boldsymbol{\epsilon}^{p}$). Assuming $\frac{dY}{d\sigma}$ as the rate of change of the yield function for plastic behaviour, then

$$d\boldsymbol{\epsilon}^{p} = d\lambda\frac{dY}{d\boldsymbol{\sigma}} \tag{2.5}$$

where $d\lambda$ is a scalar defining the magnitude of the plastic strain increment (which must satisfy the condition $dY = 0$, where Y is the yield function).

Using the principle of virtual power, the weak form of eq. 2.2, considering traction, is found by taking the product of a test function with the equation of conservation of momentum and integrating over the current configuration:

$$\int_V \rho \mathbf{a} \delta \mathbf{v} dV = \int_V \boldsymbol{\sigma} \nabla \delta \mathbf{v} dV + \int_V \rho \mathbf{b} \delta \mathbf{v} dV + \int_\Gamma \mathbf{s}^s \delta \mathbf{v} d\Gamma \tag{2.6}$$

where $\delta \mathbf{v}$ is the test function, $\mathbf{s}^s$ is the traction load at the body surface Γ (i.e. boundary condition), and V is the current body volume. Then, since in MPM two discretisations are used (i.e. material points representing the computational body and elements representing the computational space), the integrals in 2.6 can be expressed as nodal equations via the summation of material point values in the elements, leading to the (element) equation

$$\begin{aligned} &\delta \bar{\mathbf{v}} \sum_{p=1}^{nmp} \rho_p \mathbf{N}^T(\mathbf{x}_p) \mathbf{N}(\mathbf{x}_p) \bar{\mathbf{a}} |\mathbf{J}| W_p = \\ &\delta \bar{\mathbf{v}} \left[- \sum_{p=1}^{nmp} \mathbf{B}^T(\mathbf{x}_p) \boldsymbol{\sigma}_p |\mathbf{J}| W_p + \sum_{p=1}^{nmp} \rho_p \mathbf{N}^T(\mathbf{x}_p) \mathbf{b} |\mathbf{J}| W_p + \sum_{p=1}^{bmp} \mathbf{N}^T(\mathbf{x}_p) \mathbf{s}_p^s \Gamma \right] \end{aligned} \tag{2.7}$$

where ρ_p is the material point mass density, $\mathbf{N}$ is the element matrix of shape functions (SFs), $\mathbf{B}$ represent the strain-displacement matrix, $\bar{\mathbf{a}}$ is the vector of nodal accelerations, $\mathbf{x}_p$ is the position of each material point, $\boldsymbol{\sigma}_p$ is the material point stress tensor, $\mathbf{J}$ is the Jacobian matrix, W_p is the material point integration weight (which is dimensionless and equal to the volume of the material point in isoparametc parent element coordinates), s_p^s is the material point traction force, nmp is the number of material points p, and bmp is the number of boundary material points having a concentrated traction load. Note that the shape functions are used to interpolate the material point variables to the element nodes (i.e. $\mathbf{N}\delta\bar{\mathbf{v}}(\mathbf{x}_p) = \delta\mathbf{v}(\mathbf{x}_p)$, where $\delta\bar{\mathbf{v}}$ is the vector of nodal test function velocities) and the volume of each material point is represented by the Jacobian determinant and the material point weight (i.e. $v_p = |\mathbf{J}| W_p$, where v_p is the material point volume), which results from implementing the quadrature rule. Finally, since the element test function ($\delta\bar{\mathbf{v}}$) in eq. 2.7 should hold for any arbitrary virtual velocity that satisfies all boundary conditions, it vanishes from eq. 2.7 since $\delta\bar{\mathbf{v}}\mathbf{A} = \delta\bar{\mathbf{v}}\mathbf{B}$, in which $\mathbf{A}$ and $\mathbf{B}$ represent the left and right side of eq. 2.7, respectively. Then eq. 2.7 reduces further and may be expressed for an element $|_{elem}$ using matrix notation as

$$\mathbf{m}|_{elem} \bar{\mathbf{a}}|_{elem} = \mathbf{F}^{ext}|_{elem} - \mathbf{F}^{int}|_{elem} \tag{2.8}$$

where

$$\mathbf{m}|_{elem} = \sum_{p=1}^{nmp} \rho_p \mathbf{N}^T(\mathbf{x}_p) \mathbf{N}(\mathbf{x}_p) |\mathbf{J}| W_p \tag{2.9}$$

$$\mathbf{F}^{ext}|_{elem} = \sum_{p=1}^{nmp} \rho_p \mathbf{N}^T(\mathbf{x}_p) \mathbf{b} |\mathbf{J}| W_p + \sum_{p=1}^{bmp} \mathbf{N}^T(\mathbf{x}_p) \mathbf{s}_p^s \Gamma \tag{2.10}$$

$$\mathbf{F}^{int}|_{elem} = \sum_{p=1}^{nmp} \mathbf{B}(\mathbf{x}_p) \boldsymbol{\sigma}_p |\mathbf{J}| W_p \tag{2.11}$$

In eq. 2.8 and 2.9, $\mathbf{m}$ represents the elemental consistent mass matrix, which can increase the solution time. Hence, the element lumped mass matrix is used here, and is computed using the “row-summation” technique as

$$\mathbf{m}_{ii} = \sum \mathbf{m}_{ij} \tag{2.12}$$

Furthermore, the lumped mass matrix can be replaced by an element mass vector ($\bar{\mathbf{m}}_i = \mathbf{m}_{ii}$). This replacement improves the computational time, since matrix operations (i.e. matrix inverse computation) are replaced by linear operation. Finally, note that the use of $\bar{\mathbf{m}}$ is particular to the explicit scheme, whereas in the implicit scheme $\mathbf{m}$ will be used.

2.3.2. NODAL INTEGRATION, SOLUTION AND UPDATE PHASE (EXPLICIT)

At the beginning of each solution step, state variables are mapped to the nodes. For example, the velocity at node i is computed as

$$\mathbf{v}_i^t = \frac{\sum_{p=1}^{nmp} \rho_p \mathbf{v}_p^t N_i(\mathbf{x}_p) |\mathbf{J}| W_p}{\sum_{p=1}^{nmp} \rho_p N_i(\mathbf{x}_p) |\mathbf{J}| W_p} \tag{2.13}$$

where N_i is the nodal SF, and the summation is over all the material points in the elements surrounding the node. After nodal mapping and integration to form the element equations, an assembly operation over the mesh is undertaken (as in FEM), yielding global vectors and matrices at time t, i.e. the global mass matrix $\mathbf{m}^t$, the global external force $\mathbf{F}^{ext,t}$ and global internal force $\mathbf{F}^{int,t}$, which can be solved to find the global acceleration vector. Since the vector of nodal masses is used, the solution of the equation of equilibrium (in terms of accelerations) is computed as

$$\bar{\mathbf{a}}^t = \frac{\mathbf{F}^{ext,t} - \mathbf{F}^{int,t}}{\bar{\mathbf{m}}^t} \tag{2.14}$$

and, using the Euler time integration technique, material point variables are updated at time $t + \Delta t$ as

$$\mathbf{v}_p^{t+\Delta t} = \mathbf{v}_p^t + \mathbf{N}(\mathbf{x}_p)\bar{\mathbf{a}}^t |_{elem} \, \Delta t \tag{2.15}$$

$$\mathbf{x}_p^{t+\Delta t} = \mathbf{x}_p^t + \mathbf{v}_p^{t+\Delta t} \Delta t \tag{2.16}$$

$$\boldsymbol{\sigma}_p^{t+\Delta t} = \mathbf{D}_p \nabla \mathbf{N}(\mathbf{x}_p) \bar{\mathbf{v}}^{t+\Delta t} |_{elem} + \boldsymbol{\sigma}_p^t \tag{2.17}$$

where $\boldsymbol{\sigma}_p^t$ is the previous material point stress. Furthermore, the vector of (element) nodal velocities at time $t + \Delta t$ in eq. 2.17 is computed from the material point velocities at time $t + \Delta t$ as

$$\bar{\mathbf{v}}^{t+\Delta t} |_{elem} = \frac{\sum_{p=1}^{nmp} m_p \mathbf{v}_p^{t+\Delta t} \mathbf{N}(\mathbf{x}_p)}{\sum_{p=1}^{nmp} m_p \mathbf{N}(\mathbf{x}_p)} \tag{2.18}$$

where m_p is the material point mass. Note that this vector of nodal velocities is computed from the material point velocities at time $t + \Delta t$ rather than using the Euler time integration method (i.e. $\bar{\mathbf{v}}^{t+\Delta t} = \bar{\mathbf{v}}^t + \bar{\mathbf{a}}^{t+\Delta t} \Delta t$) to ensure conservation of momentum.

2.3.3. IMPLICIT MPM

To derive the equation for implicit equilibrium, the principle of virtual work is used. This states that the difference between the internal and external work should be equal to zero ($\Pi = W^{int} - W^{ext}$), and is written as

$$\Pi = \frac{1}{2}\int_V \boldsymbol{\epsilon}^T \mathbf{D}\boldsymbol{\epsilon} dV - \left(\int_V \mathbf{u}^T \rho(\mathbf{b}-\mathbf{a}) dV + \int_\Gamma \mathbf{u}^T \mathbf{s}^s d\Gamma\right) \tag{2.19}$$

where $\mathbf{u}$ represents the continuous displacement field. In the second term on the right hand side of eq. 2.19, the inertia term (i.e. $\mathbf{a}$) is included as part of the body forces using D'Alembert's principle. Then, by evaluating $\Pi\delta = 0$ with respect to the displacements and knowing that $\delta\boldsymbol{\epsilon}^2 = 2\boldsymbol{\epsilon}\delta\boldsymbol{\epsilon}$ (Davies 2011, Bathe 2006), eq. 2.19 becomes

$$\int_V \delta\boldsymbol{\epsilon}^T \mathbf{D}\boldsymbol{\epsilon} dV = \int_V \delta\mathbf{u}^T \rho\,(\mathbf{b}-\mathbf{a})\, dV + \int_\Gamma \delta\mathbf{u}^T \mathbf{s}^s d\Gamma \tag{2.20}$$

where $\delta\mathbf{u}$ and $\delta\boldsymbol{\epsilon}$ represent the test function in terms of displacements and strains. Then, following similar procedures as in eq. 2.7 and expressing the total material point stresses as functions of the previous material point stresses $\left(\text{i.e.}\boldsymbol{\sigma} = \boldsymbol{\sigma}^0 + \Delta\boldsymbol{\sigma}\right)$, eq. 2.20 is written as

$$\begin{aligned}\left[\sum_{i=1}^{nmp} \mathbf{B}^T(\mathbf{x}_p)\mathbf{D}_p\mathbf{B}(\mathbf{x}_p)\,|\mathbf{J}|\,W_p\right]\bar{\mathbf{u}} - \sum_{i=1}^{nmp} \rho_p \mathbf{N}^T(\mathbf{x}_p)\mathbf{N}(\mathbf{x}_p)\bar{\mathbf{a}}\,|\mathbf{J}|\,W_p = \\ -\sum_{i=1}^{nmp} \mathbf{B}^T(\mathbf{x}_p)\boldsymbol{\sigma}^t\,|\mathbf{J}|\,W_p + \sum_{i=1}^{nmp} \rho_p \mathbf{N}^T(\mathbf{x}_p)\mathbf{b}\,|\mathbf{J}|\,W_p + \sum_{p=1}^{bmp} \mathbf{N}^T(\mathbf{x}_p)\mathbf{s}^s\Gamma\end{aligned} \tag{2.21}$$

where $\mathbf{B}$ is used to interpolate the virtual strains using virtual nodal displacements, i.e. $\mathbf{B}\delta\bar{\mathbf{u}}\left(\mathbf{x}_p\right) = \delta\boldsymbol{\epsilon}\left(\mathbf{x}_p\right)$, where $\delta\bar{\mathbf{u}}$ are the virtual displacements, $\boldsymbol{\sigma}^0$ represents the vector of initial stress, and $\bar{\mathbf{u}}$ represents the vector of (element) nodal displacements, which is obtained from the interpolation of strains, i.e. $\mathbf{B}\bar{\mathbf{u}} = \boldsymbol{\epsilon}$. As for eq. 2.8, the previous equation can be expressed in matrix form as

$$\mathbf{K}\Delta\bar{\mathbf{u}}\,|_{elem} + \mathbf{m}\bar{\mathbf{a}}\,|_{elem} = \mathbf{F}^{ext}\,|_{elem} - \mathbf{F}^{int}\,|_{elem} \tag{2.22}$$

where the element stiffness matrix is

$$\mathbf{K}\,|_{elem} = \sum_{p=1}^{nmp} \mathbf{B}^T(\mathbf{x}_p)\mathbf{D}\mathbf{B}(\mathbf{x}_p)\,|\mathbf{J}|\,Wp \tag{2.23}$$

and $\mathbf{F}^{ext}\,|_{elem}$ and $\mathbf{F}^{int}\,|_{elem}$ are similar to eq. 2.10 and eq. 2.11, respectively.

2.3.4. STATIC SCHEME

To obtain the static scheme, the inertia term (i.e. $\mathbf{ma}$) in eq. 2.19 should be ignored, then the equation of equilibrium reduces to

$$\mathbf{K}\Delta\bar{\mathbf{u}}\,|_{elem} = \mathbf{F}^{ext}\,|_{elem} - \mathbf{F}^{int}\,|_{elem} \tag{2.24}$$

which represents quasi-static equilibrium. Finally, details of the matrices used in previous sections are elaborated in Appendix A

2.4. NEWMARK'S TIME INTEGRATION SCHEME

By using the Newmark (1959) time integration technique, which is recognised to be highly effective (Bathe 2007), eq. 2.22 can be computed as a function of time. Velocities and displacements at time $t + \Delta t$ are computed as

$$\bar{\mathbf{v}}^{t+\Delta t} = \bar{\mathbf{v}}^{t} + \left[(1-\gamma)\bar{\mathbf{a}}^{t} + \gamma\bar{\mathbf{a}}^{t+\Delta t}\right]\Delta t \tag{2.25}$$

$$\bar{\mathbf{u}}^{t+\Delta t} = \bar{\mathbf{u}}^{t} + \bar{\mathbf{v}}^{t}\Delta t + \left[\left(\frac{1}{2}-\alpha\right)\bar{\mathbf{a}}^{t} + \alpha\bar{\mathbf{a}}^{t+\Delta t}\right]\Delta t^{2} \tag{2.26}$$

where $\bar{\mathbf{u}}^{t+\Delta t}$, $\bar{\mathbf{v}}^{t+\Delta t}$, and $\bar{\mathbf{a}}^{t+\Delta t}$ are the respective vectors of displacements, velocities and accelerations at time $t + \Delta t$, and α and γ are time stepping parameters that are chosen to be $\alpha = 0.25$ and $\beta = 0.5$ (giving a constant-average-acceleration approach). Then, isolating $\bar{\mathbf{a}}^{t+\Delta t}$ from equation eq. 2.26 leads to

$$\bar{\mathbf{a}}^{t+\Delta t} = \left(\frac{4\bar{\mathbf{u}}^{t}}{\Delta t^{2}} - \frac{4\bar{\mathbf{v}}^{t}}{\Delta t} - \bar{\mathbf{a}}^{t}\right) \tag{2.27}$$

where $\Delta\bar{\mathbf{u}} = \bar{\mathbf{u}}^{t+\Delta t} + \bar{\mathbf{u}}^{t}$ is the vector of total displacements as a function of the incremental and initial displacements. Then, substituting eq. 2.27 into eq. 2.25 results in

$$\bar{\mathbf{v}}^{t+\Delta t} = \frac{2\bar{\mathbf{u}}^{t}}{\Delta t} - \mathbf{v}^{t} \tag{2.28}$$

Finally, substituting eq. 2.27 into eq. 2.22 and adding the Newton-Raphson iteration procedure, the equilibrium equation is written as

$$\left(\mathbf{K}^{t} + \frac{4\mathbf{m}^{t}}{\Delta t^{2}}\right)^{\mathbf{k}}\Delta\bar{\mathbf{u}} = {}^{(k-1)}\left(\mathbf{F}^{ext,t+\Delta t} - \mathbf{m}^{t}\left(\frac{4^{(k-1)}\bar{\mathbf{u}}^{t}}{\Delta t^{2}} - \frac{4\bar{\mathbf{v}}^{t}}{\Delta t} - \bar{\mathbf{a}}^{t}\right) - {}^{(k-1)}\mathbf{F}^{int,t+\Delta t}\right) \tag{2.29}$$

or

$$\bar{\mathbf{K}}^{\mathbf{k}}\Delta\bar{\mathbf{u}} = {}^{(k-1)}\left(\mathbf{F}^{ext} - \mathbf{F}^{kin} - \mathbf{F}^{int}\right)^{t+\Delta t} \tag{2.30}$$

where

$$\bar{\mathbf{K}}^{t} = \mathbf{K}^{t} + \frac{4\mathbf{m}^{t}}{\Delta t^{2}} \tag{2.31}$$

and

$${}^{k}\mathbf{F}^{kin,t+\Delta t} = \mathbf{m}^{t}\left(\frac{4^{(k-1)}\bar{\mathbf{u}}^{t}}{\Delta t^{2}} - \frac{4\bar{\mathbf{v}}^{t}}{\Delta t} - \bar{\mathbf{a}}^{t}\right) \tag{2.32}$$

In the previous equations, $\bar{\mathbf{K}}$ represents a modified stiffness matrix, $\mathbf{F}^{kin}$ are the kinetic forces, and the left superscript k refers to the Newton-Raphson iteration step, which can be stopped after the desired convergence criterion has been reached, which in this thesis is computed as (Guilkey & Weiss 2003)

$$\frac{\left\|{}^{k}\Delta\bar{\mathbf{u}}\right\|}{\left\|{}^{k}\bar{\mathbf{u}}\right\|} < \text{tol} \tag{2.33}$$

where tol is the tolerance value. There are several alternative convergence criteria which could be used, but this has been selected due to simplicity. It is noted that this convergence criterion is susceptible to false convergence due to iteration stagnation.

2.4.1. NODAL INTEGRATION AND UPDATE PHASE (DYNAMIC)

The integration of nodal external loads, mass, velocity and stiffness has already been shown in eq. 2.10, 2.12, 2.13 and 2.23, respectively. In addition, in contrast to the explicit scheme, nodal accelerations are needed and are computed as

$$\bar{\mathbf{a}}_i^t = \frac{\sum_{p=1}^{nmp} \rho_p \mathbf{a}_p^t N_i(\mathbf{x}_p) |\mathbf{J}| W_p}{\sum_{p=1}^{nmp} \rho_p N_i(\mathbf{x}_p) |\mathbf{J}| W_p} \tag{2.34}$$

After assembling the stiffness and mass matrices (eq. 2.31), the equilibrium in terms of displacements is computed (eq. 2.30) and the vectors of internal forces, nodal accelerations and kinetic forces are updated every iteration step using eq. 2.11, 2.27 and 2.32, respectively. Finally, after the desired tolerance is reached (i.e. the change of incremental displacements is nearly zero), the updates of material point acceleration, velocity, position and stress are computed as

$$\mathbf{a}_p^{t+\Delta t} = \mathbf{N}(\mathbf{x}_p)\bar{\mathbf{a}}^{t+\Delta t}|_{elem} \tag{2.35}$$

$$\mathbf{v}_p^{t+\Delta t} = \mathbf{v}_p^t + \frac{\left[\mathbf{N}(\mathbf{x}_p)\bar{\mathbf{a}}^{t+\Delta t}|_{elem} + \mathbf{a}_p^t\right]}{2}\Delta t \tag{2.36}$$

$$\mathbf{x}_p^{t+\Delta t} = \mathbf{x}_p^t + \mathbf{N}(\mathbf{x}_p)\bar{\mathbf{u}}|_{elem} \tag{2.37}$$

$$\boldsymbol{\sigma}_p^{t+\Delta t} = \mathbf{D}\mathbf{B}(\mathbf{x}_p)\bar{\mathbf{u}}|_{elem} + \boldsymbol{\sigma}_p^t \tag{2.38}$$

2.5. CONSERVATION OF MASS AND MOMENTUM IN THE IMPLICIT MPM

In MPM, because of the partition of unity of the SFs, mass is automatically conserved in mapping:

$$\sum_{i=1}^{nn} m_i = \sum_{i=1}^{nn}\sum_{p=1}^{nmp} m_p N_i(\mathbf{x}_p) = \sum_{p=1}^{nmp} m_p \tag{2.39}$$

where m_p is the material point mass, which is computed as $m_p = \rho_p |\mathbf{J}| W_p$. Regarding the conservation of momentum, the method uses the FEM approach to solve the equation of motion on the nodes, which conserves momentum, and therefore it is the updating of the material point momentum that is considered here. The total linear momentum of a material point at the end of a time step is determined considering Newmark's scheme, and is computed as

$$\sum_{p=1}^{nmp} m_p \mathbf{v}_p^{t+\Delta t} = \sum_{p=1}^{nmp} m_p \left[\mathbf{v}_p^t + \frac{1}{2}\left[\mathbf{a}_p^t + \sum_{i=1}^{nn} \bar{\mathbf{a}}_i^{t+\Delta t} N_i(\mathbf{x}_p)\right]\right] \tag{2.40}$$

In MPM, the total nodal momentum and change of momentum are equal to the total material point momentum and change of momentum, due to the partition of unity of the SF, as

$$\sum_{i=1}^{nn} m_i \bar{\mathbf{v}}_i^t = \sum_{i=1}^{nn} \sum_{p=1}^{nmp} m_p \mathbf{v}_p^t N_i(\mathbf{x}_p) = \sum_{p=1}^{nmp} m_p \mathbf{v}_p^t \tag{2.41}$$

and

$$\sum_{i=1}^{nn} m_i \bar{\mathbf{a}}_i^t = \sum_{i=1}^{nn} \sum_{p=1}^{nmp} m_p \mathbf{a}_p^t N_i(\mathbf{x}_p) = \sum_{p=1}^{nmp} m_p \mathbf{a}_p^t \tag{2.42}$$

Substituting eq. 2.41 and eq. 2.42 into eq. 2.40, and rearranging, leads to

$$\begin{aligned} \sum_{p=1}^{nmp} m_p \mathbf{v}_p^{t+\Delta t} = \sum_{p=1}^{nmp} m_p \mathbf{v}_p^t + \frac{1}{2}\Delta t \sum_{p=1}^{nmp} m_p \mathbf{a}_p^t + \\ 2\sum_{i=1}^{nn} m_i \frac{\Delta \bar{\mathbf{u}}_i}{\Delta t} - 2\sum_{i=1}^{nn} m_i \bar{\mathbf{v}}_i^t - \frac{1}{2}\Delta t \sum_{p=1}^{nmp} m_p \mathbf{a}_p^t \end{aligned} \tag{2.43}$$

which reduces further to

$$\sum_{p=1}^{nmp} m_p \mathbf{v}_p^{t+\Delta t} = 2\sum_{i=1}^{nn} m_i \frac{\Delta \bar{\mathbf{u}}_i}{\Delta t} - \sum_{i=1}^{nn} m_i \bar{\mathbf{v}}_i^t \tag{2.44}$$

Considering that the equation of equilibrium has reached convergence (the right-hand side of eq. 2.30 reduces to zero within a specified tolerance), the following is true:

$$\mathbf{F}_i^{ext,t+\Delta t} - \mathbf{m}_i^t \left(\frac{4\Delta \bar{\mathbf{u}}_i^{t+\Delta t}}{\Delta t^2} - \frac{4\bar{\mathbf{v}}_i^t}{\Delta t} - \bar{\mathbf{a}}_i^t \right) - \mathbf{F}_i^{int,t+\Delta t} = \{0\} \tag{2.45}$$

Then, considering an isolated system, i.e. where momentum would not be altered by external forces, it can be stated that

$$\mathbf{F}^{ext,t+\Delta t} = \{0\} \tag{2.46}$$

At the beginning of the time step, for an isolated system, there is no net rate of change of momentum:

$$\sum_{p=1}^{nmp} m_p \mathbf{a}_p^t = \sum_{i=1}^{nn} m_i \bar{\mathbf{a}}_i^t = \{0\} \tag{2.47}$$

Moreover, acknowledging that $\sum_i^{nn} \mathbf{B}_i(\mathbf{x}_p) = \{0\}$, then

$$\mathbf{F}_{i,int}^{t+\Delta t} = -\sum_{i=1}^{nn} \sum_{p=1}^{nmp} \boldsymbol{\sigma}_p \mathbf{B}_i(\mathbf{x}_p) |\mathbf{J}| W_p = \{0\} \tag{2.48}$$

Summing eq. 2.45 over all the nodes, and substituting in eq. 2.46 - 2.48, yields

$$\sum_{i=1}^{nn} m_i \frac{4\Delta \bar{\mathbf{u}}_i}{\Delta t^2} - \sum_{i=1}^{nn} m_i \frac{4\Delta \bar{\mathbf{v}}_i}{\Delta t} = \{0\} \tag{2.49}$$

Finally, substituting eq. 2.49 into eq. 2.44 leads to the conservation of momentum for the isolated system as

$$\sum_{p=1}^{nmp} m_p \mathbf{v}_p^{t+\Delta t} = 2\sum_{i=1}^{nn} \mathbf{m}_i \bar{\mathbf{v}}_i^t - \sum_{i=1}^{nn} m_i \bar{\mathbf{v}}_i^t = \sum_{p=1}^{nmp} m_p \mathbf{v}_p^t \tag{2.50}$$

2.6. IMPLEMENTATION OF MPM

In Table 2.1, the main steps followed in the explicit MPM are shown, and several minor steps have been ignored (e.g. setting vector and matrix sizes, upgrading material point local coordinates, activation of elements, initialization of nodal values, etc.) to keep the structure of the steps followed as simple as possible. As can be seen, the steps followed in this scheme are relatively few and large matrices are not constructed. As previously mentioned, this simplicity is what makes the scheme attractive to many engineers.

Table 2.1: Steps followed in the explicit MPM scheme

Integrate nodal mass and velocity: $\bar{\mathbf{m}}^t$ and $\bar{\mathbf{v}}^t$
Integrate nodal external and internal loads: $\mathbf{F}^{ext,t}$ and $\mathbf{F}^{int,t}$
Estimate nodal accelerations: $\bar{\mathbf{a}}^t$
Update material point velocity at time $t+\Delta t$: $\mathbf{v}_p^{t+\Delta t}$
Update nodal velocities: $\bar{\mathbf{v}}^{t+\Delta t}$
Evaluate material point trial stresses: $\boldsymbol{\sigma}_p^{trial}$
Loop 1: if $Y(\boldsymbol{\sigma}_p^{trial}) > 0$: return stresses to the yield surface Y
Plastic iteration loop
IF $Y(\boldsymbol{\sigma}_p^{trial(t+\Delta t)}) = 0$: EXIT Loop 1
END Loop 1
Update material point stresses $\boldsymbol{\sigma}_p^{t+\Delta t} = \boldsymbol{\sigma}_p^{trial(t+\Delta t)}$
Update material point positions: $\mathbf{x}_p^{t+\Delta t}$

In Table 2.1, the trial stress is computed as in eq. 2.17, and then it is tested to determine if plasticity is encouraged. If plasticity occurs, several plastic iterative steps must be followed to return the stresses to the elastic region. These iterative plastic steps are indicated in the table but not elaborated, since they are outside the scope of this work. The reader is directed to Sloan (1987) and Sloan *et al.* (2001), where the plastic procedures implemented in this thesis are elaborated.

In Table 2.2, the steps followed in the static scheme are shown. In this solution scheme, the nodal displacements ($\bar{\mathbf{u}}$) cannot be computed directly as the nodal accelerations are in the explicit scheme. Instead, an additional numerical procedure must be employed to compute the nodal displacements as a function of the nodal loads and stiffness. Similar to the plastic iterative steps, elaboration of this numerical procedure is out of the scope of this work. Nevertheless, a detailed description of some of these procedures can be found in Smith *et al.* (2013). Finally, the vectors and matrices which remain the same during the iterative solution procedure are kept outside the loop. Including these elements in the iterative loop would not have an impact on the accuracy of the solution, but would increase the computational time. In Table 2.3, the steps followed in the implicit scheme are shown. In this scheme, the steps followed are similar to the static scheme, but with the difference that the kinematics are included as part of the solution.

Table 2.2: Steps followed in the static MPM scheme

Integrate nodal external loads: $\mathbf{F}^{ext}$
Integrate nodal stiffness: $\mathbf{K}$
Loop 1: over the max number of iteration steps
Integrate nodal internal loads: ${}^{k-1}\mathbf{F}^{int}$
Estimate nodal displacements: ${}^{k}\bar{\mathbf{u}}$
Evaluate material point trial stresses: ${}^{k}\boldsymbol{\sigma}_p^{trial}$
Loop 2: if $Y(\boldsymbol{\sigma}_p^{trial}) > 0$: return stresses to the yield surface Y
Plastic iteration loop
IF $Y(\boldsymbol{\sigma}_p^{trial}) = 0$: EXIT Loop 2
END Loop 2
Update material point stresses $\boldsymbol{\sigma}_p = \boldsymbol{\sigma}_p^{trial}$
IF converge or max number of iterations is reached: EXIT Loop 1
END Loop 1
Update material point positions: $\mathbf{x}_p$

Table 2.3: Steps followed in the implicit MPM scheme

Integrate nodal mass, velocity and acceleration: $\mathbf{m}^t$, $\bar{\mathbf{v}}^t$, $\bar{\mathbf{a}}^t$
Integrate nodal external loads: $\mathbf{F}_{ext}^t$
Integrate nodal stiffness: $\bar{\mathbf{K}}^t$
Initialize total displacement vector: $\bar{\mathbf{u}} = 0$
Loop 1: over the max number of iteration steps
Integrate nodal internal loads: ${}^{k-1}\mathbf{F}_{int}^{t+\Delta t}$
Integrate nodal kinetic loads: ${}^{k-1}\mathbf{F}_{kin}^{t+\Delta t}$
Estimate nodal displacements: ${}^{k}\Delta\bar{\mathbf{u}}^{t+\Delta t}$
Update nodal accelerations: ${}^{k}\bar{\mathbf{a}}^{t+\Delta t}$
Evaluate material point trial stresses: ${}^{k}\boldsymbol{\sigma}_p^{trial}$
Loop 2: if $Y(\boldsymbol{\sigma}_p^{trial}) > 0$: return stresses to the yield surface Y
Plastic iteration loop
IF $Y(\boldsymbol{\sigma}_p^{trial(t+\Delta t)}) = 0$: EXIT Loop 2
END Loop 2
Update material point stresses $\boldsymbol{\sigma}_p^{t+\Delta t} = \boldsymbol{\sigma}_p^{trial(t+\Delta t)}$
IF converge or max number of iterations is reached: EXIT Loop 1
END Loop 1
Update material point accelerations: $\mathbf{a}_p^{t+\Delta t}$
Update material point velocities: $\mathbf{v}_p^{t+\Delta t}$
Update material point positions: $\mathbf{x}_p^{t+\Delta t}$

2.7. EVALUATION OF MPM

To demonstrate the potential and limitations of MPM, three benchmark problems are studied. These problems are simulated using the schemes previously described (if applicable), followed by a discussion of the results obtained.These problems are selected to investigate different aspects of MPM, such as large displacements, energy conservation, and accuracy of the results. Also, some of the main limitations in MPM and early treatments are introduced. The first benchmark investigated is a block which falls due to gravity loading and bounces over a rigid surface. This problem is introduced to demonstrate the conservative qualities of MPM, using plots of the material point's position, velocity and energy conservation. The second benchmark is the simulation of a 1D bar (using 2D elements) undergoing compression due to an increment of the gravity force. The objective of this benchmark is to show that, independently of the observed realistic deformation of the bar, the results are far from the real results. These inaccuracies are demonstrated by comparing MPM results against those obtained with UL-FEM and the analytical solution. Finally, the third benchmark consists of a vertical cutting, which fails due to its self-weight and the low strength of the material. The importance of this problem is to demonstrate the feasibility of simulating geotechnical problems including post-failure behaviour. The results for the vertical cutting are compared to the FEM results, and the similarity of the results is promising.

In this thesis, the consequences of using different (i) numbers of material points, (ii) element sizes, and (iii) time steps is not extensively studied. The main objective in this work is to understand MPM, its advantages and sources of inaccuracies, in order to develop adequate improvements. Most of the problems studied use conventional mesh discretisation (i.e. equal-sized four noded structured meshes), with four material points equally distributed inside the elements (i.e. initially located at the local coordinates $\xi \pm 0.5$ and $\eta \pm 0.5$), and reasonably small time steps (i.e. time steps that are large enough to return accurate results in less computational time). Finally, all the benchmark and problems solved in this and the following sections use the plane strain condition and do not consider damping.

2.7.1. FREE FALL BLOCK

This problem consists of a block made up material points which is in free-fall due to the gravity force, and bounces over a rigid surface. Figure 2.3a shows a sketch of the problem, and Figure 2.3b shows the MPM discretisation including the boundary conditions. In this simulation, the background mesh is constructed using elements of size $\Delta x = \Delta y = 0.20$ m, and the block is modelled by placing material points inside 25 elements, forming a square of 1 m side length. The distance between the block and the rigid surface is $h_2 = 0.8$ m. The behaviour of the material is linear elastic, and the parameters used are Young's modulus, E = 1000 kPa, and Poisson's ratio, $\upsilon = 0.45$. The material unit weight and gravity load are, $\gamma_{block} = 15\,kN/m^3$ and $g = 10\,m/s^s$, respectively. The time step used in the explicit and the implicit schemes is $\Delta t = 1.0 \times 10^{-5}$ s. The use of the same time step in the explicit and the implicit schemes is for comparison purposes. Note that the rigid surface is considered by fixing the boundary nodes, while the nodes at the left and right sides of the computational domain are fixed only in the horizontal direction.

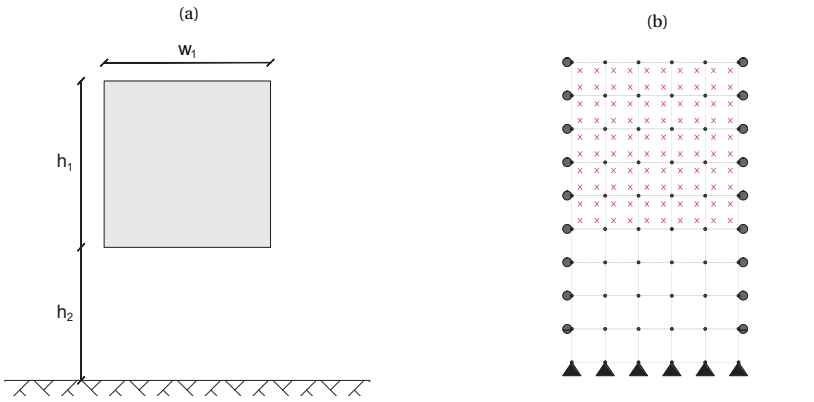

Figure 2.3: a) Sketch of the free fall block, and b) MPM discretization considering boundary conditions

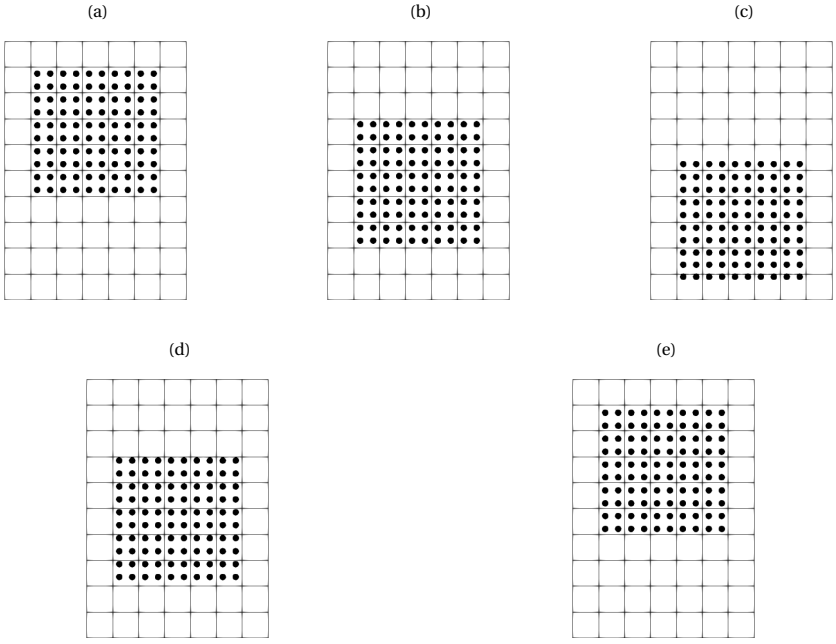

Figure 2.4: Position of the falling block using the explicit scheme after a) 0.0, b) 0.28, c) 0.4, d) 0.5, and e) 0.78 seconds

Figure 2.4 shows the explicit simulation of the falling block throughout 0.8 s of simulation. It is observed that the material points are able to move a relatively significant distance, crossing several elements without experiencing perturbations. Moreover, it is observed that at time t = 0.78 s (Figure 2.4e), the block is able to reach its original position, which means that the energy in the system is conserved. Note that the bouncing occurs due to the fixed boundary, which prevents the displacement of the block, causing the

development of strain energy which consequentially pushes the block upwards. Contact begins as soon as a material point enters an element where a boundary condition is applied.

Figure 2.5 shows the average displacement of the block using the explicit and implicit schemes, in which the positions of the block illustrated in Figure 2.4 are indicated. Compared to the results shown in Figure 2.4, these results are extended until the block has bounced three times. It is seen that both solutions are identical and, after each bounce, the block almost recovers its original position, demonstrating energy conservation. Figure 2.6 shows the mean velocity of the block. Again, the results of the explicit and implicit solutions are similar. Moreover, it is observed that the maximum (absolute) velocities reached before and after each bounce (v_{max} and $-v_{max}$, respectively) are almost equal (as expected), and that these values remain constant at each bounce. Finally, in Figure 2.7, the plot of the total energy (TE) is shown. In this case, TE is computed by adding the kinetic energy (KE), the potential energy (PE), and the strain energy (SE). Each energy can be computed as

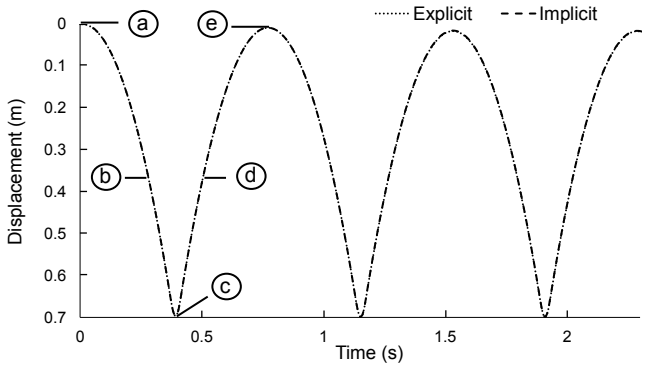

Figure 2.5: Position of the block throughout the simulation using the explicit and the implicit scheme, where labels a-e indicate the results shown in Figure 2.4

$$KE = \frac{1}{2}\sum_{p=1}^{nmp} m_p \mathbf{v}_p^2 \tag{2.51}$$

$$PE = \mathbf{g}\sum_{p=1}^{nmp} m_p h_p \tag{2.52}$$

$$SE = \frac{1}{2}\sum_{p=1}^{nmp} V_p \boldsymbol{\sigma}_p \boldsymbol{\epsilon}_p \tag{2.53}$$

where h_p is the distance between the material point and the rigid surface. Note that the material point volume and velocity are depicted using an uppercase V and a lowercase v, respectively. It is seen that the results using the explicit and implicit schemes are not equal, and that the energy with the implicit scheme reduces a fraction after each bounce (B.1, B.2, and B.3, respectively). Since this loss of energy is small, its effect is not evident

in Figure 2.5. Also, it is assumed that this loss of energy is caused by using the constant-average-acceleration approach in a non-linear event (contact), as this causes numerical instability (as studied in Deuflhard *et al.* 2008).

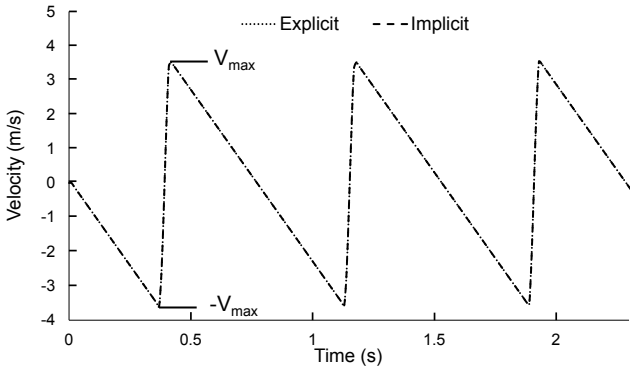

Figure 2.6: Velocity of the block throughout the simulation using the explicit and the implicit scheme

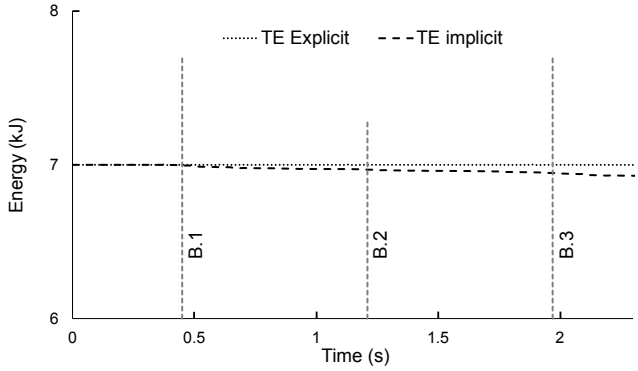

Figure 2.7: Energy conservation of the free fall block using the explicit and the implicit scheme

2.7.2. 1D COMPRESSION BAR

This problem consists of a 1D bar which is compressed due to an increase of the gravity force. Figure 2.8 shows a sketch of the bar including the boundary conditions. The bar is constructed using square elements of size $\Delta x = \Delta y = 0.25$ m. The nodes at the bottom are fully fixed, while the nodes at the left and right vertical boundary are fixed in the horizontal direction to prevent lateral displacements. The dimensions of the bar are a height of $h_1 = 5$ m and a width of $w_1 = 0.25$ m. The behaviour of the material is linear elastic, and the parameters used are a Young's modulus of E = 1000 kPa and a Poisson's ratio of $\upsilon = 0.35$. The bar is initially loaded using a material unit weight of $\gamma_{bar} = 15$ kN/m^3 and an initial gravity force of 1 g. The compression of the bar is achieved by adding gravity load increments every step of $\Delta \mathbf{g} = 1.0 \times 10^{-3}$ g (for the static scheme), and $\Delta \mathbf{g} = 1.0 \times 10^{-5}$

g (for the dynamic schemes). The time step used in the dynamic scheme is $\Delta t = 1.0 \times 10^{-3}$ s.

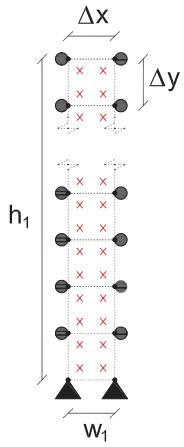

Figure 2.8: Initial condition of the bar problem

Figure 2.9 shows the deformation of the bar during the simulation and using the static scheme. Figure 2.9a show the initial configuration of the bar, in which the gravity load is equal to 1 g. Figures 2.9b and 2.9c show the bar after strains of 10 and 20 %, in which the gravity loads are 27 g and 49 g, respectively. These results appear to be realistic due to the almost uniform distribution of the material points. Figure 2.10 shows the vertical displacement of the material point at the top of the column (labelled top mp), for each solution scheme. The vertical dotted line indicates the instant at which the top material point crosses an element boundary. It is seen that the movement of the top material point increases with gravity, and that the results between the schemes are similar.

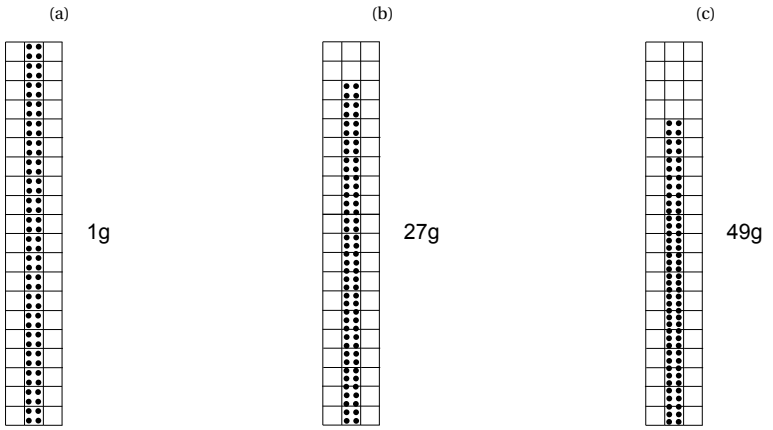

Figure 2.9: 1D bar after a deformation of a) 0, b) 0.5, and c) 1.0 m. Note the gravitational load in g next to each figure

Nonetheless, after including the results using UL-FEM, it is seen that MPM results are highly inaccurate. In Figure 2.11, the results using UL-FEM are added to the MPM results of Figure 2.10. It is seen that, initially, the results are the same. However, when the element crossing problem begins, the MPM results deviate strongly from UL-FEM results and, at the end of the simulation, the deformation is ≈ 50% below that with UL-FEM. Furthermore, Figure 2.12 shows the vertical stress of a material point located close to the centre of the bar (labelled centre mp) compared to the vertical stress of a Gauss point located initially at the same position. It is seen that the stresses are oscillating (i.e. deviating from the real stresses) during the entire simulation, and that this oscillation increases due to the element boundary-crossing problem, where the material point stress experiences large increments and decrements (with the stress at some instants being equal to zero).

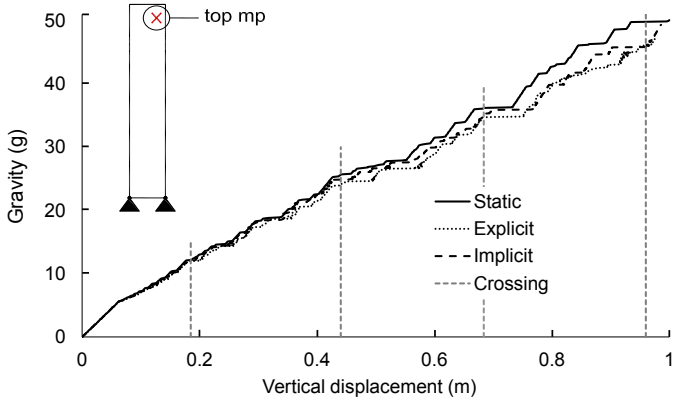

Figure 2.10: Top material point deformation using the static, the explicit and the implicit scheme

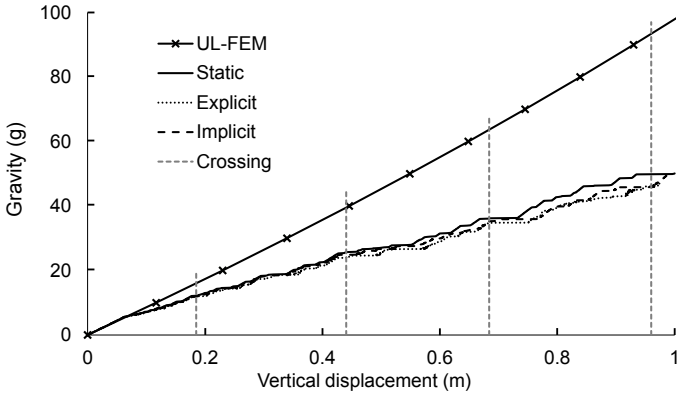

Figure 2.11: Top material point deformation including the UL-FEM solution

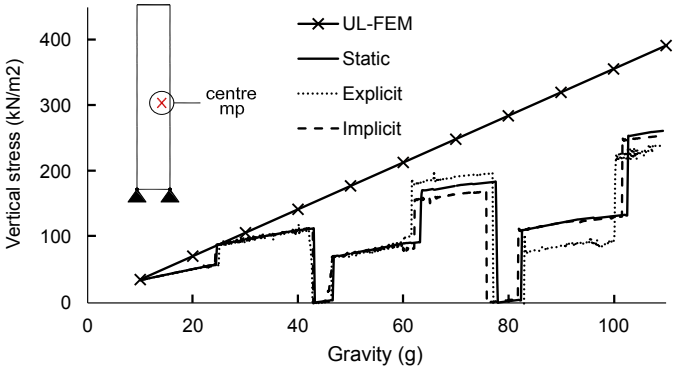

Figure 2.12: Vertical stress of a material point mp and a Gauss Point

The inaccuracies observed in Figures 2.10-2.12 are caused mainly by the use of bi-linear FE SFs (the properties of which are investigated in the next chapter). Moreover, these inaccuracies grow with the element boundary-crossing problem. In Wang (2017) these problems have been reduced by using the following solutions: (i) adding a background stiffness (i.e. each activated element has a minimum constant stiffness close to 5% of the initial element stiffness), and (ii) using incremental stresses rather than accumulated stresses (i.e. the MP stresses obtained at the end of each solution step are erased, starting the new solution step with zero MP stresses). Using these simplifications, the errors caused by using the inadequate positions of the material points to perform nodal integration can be partially removed. However, it should be noted that the problem is then not identical to the original problem. In Figures 2.13 and 2.14, the results using UL-FEM and the simplified MPM are plotted. It is clear that, compared to the previous results, the results are improved significantly. Nevertheless, the use of the simplified MPM is limited to the static scheme, and its use with dynamic schemes is not possible in many cases.

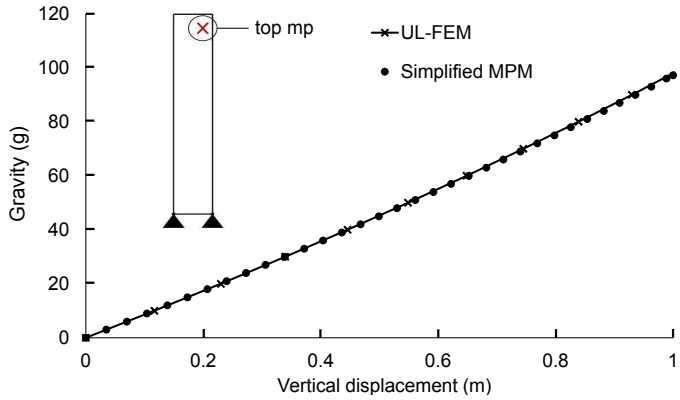

Figure 2.13: Vertical displacement of the top material point using UL-FEM and the simplified MPM

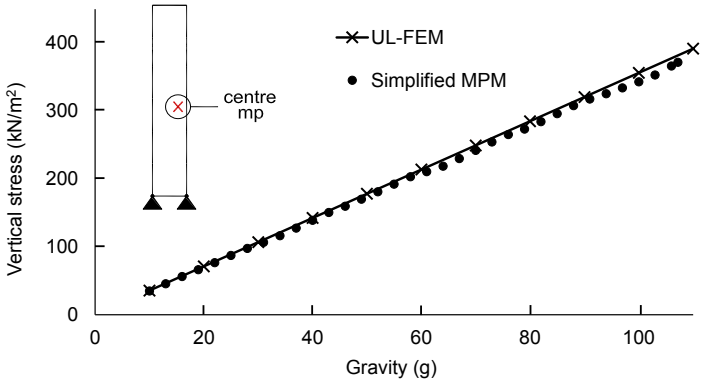

Figure 2.14: Vertical stress of the centre material point using UL-FEM and the simplified MPM

2.7.3. VERTICAL CUT

The failure of a 2D elasto-plastic vertical cutting has been simulated using a linear elastic von Mises soil incorporating linear post-peak softening, as described in Wang *et al.* (2016a). The cutting has been loaded by gradually increasing the gravity load at a rate of $\Delta g = 0.01 g/s$, and the failure occurs due to the low strength of the material. Figure 2.15 shows the boundary conditions and discretisation of the vertical cut. The cut has a height of H = 2.5 m and a length of L = 6.0 m. The size of the elements are $\Delta x = \Delta y = 0.10$ m, and each element contains(initially) four material points that are equally distributed. The material parameters are Young's modulus, E = 1000 kPa, Poisson's ratio, $\upsilon = 0.35$, and soil unit weight, $\gamma_{soil} = 20$ kN/m^3. The strength parameters are peak cohesion, $c_p = 10$ kPa, residual cohesion, $c_r = 5$ kPa, and softening modulus, $H_s = -16$ kPa. Regarding the boundary conditions, the nodes at left boundary are partly fixed to prevent displacement in the horizontal direction, whereas the nodes are fully fixed at the bottom boundary. The time discretization used in the explicit and implicit simulations are $\Delta t = 1.0 \times 10^{-3}$ s and $\Delta t = 0.1$ s, respectively.

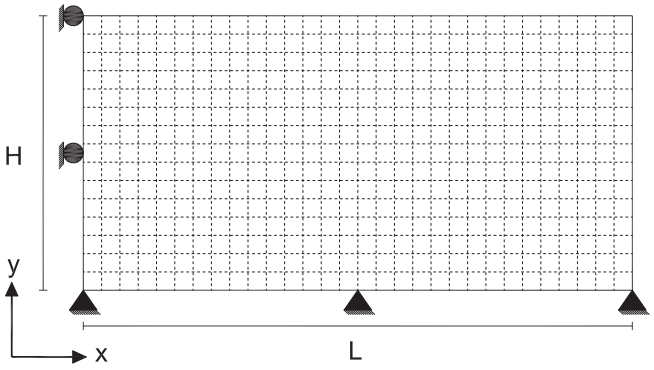

Figure 2.15: Sketch of the cutting stability problem (mesh indicative and not to scale)

Figure 2.16 shows the failure of the cutting including plastic deviatoric strains. These results correspond to the static scheme. Figure 2.16a shows the first failure at a gravity of 0.87 g. Since this failure occurs before the gravity force reaches 1g, it can be stated that the factor of safety of the cutting is below 1 (i.e. the external loads are larger than the resisting soil properties). After the first failure, and due to the continuous increase of the gravity load, two more failures occur. Figures 2.16b and 2.16c show a second and a third failure at a gravity force of 1.22 g and 1.65 g, respectively. This multi-failure mechanism is known as retrogressive failure, which has been reported in the literature (Mitchell & Klugman 1979, Kohv *et al.* 2010, Locat *et al.* 2011) and simulated using numerical techniques (Wang 2017, Zhang *et al.* 2017, Tran & Sołowski 2019). Additionally, note that the soil can slide over the bottom boundary regardless of the fully fixed boundary condition. This is because the bottom boundary elements can undergo shear deformation, which allows the displacement of the material points.

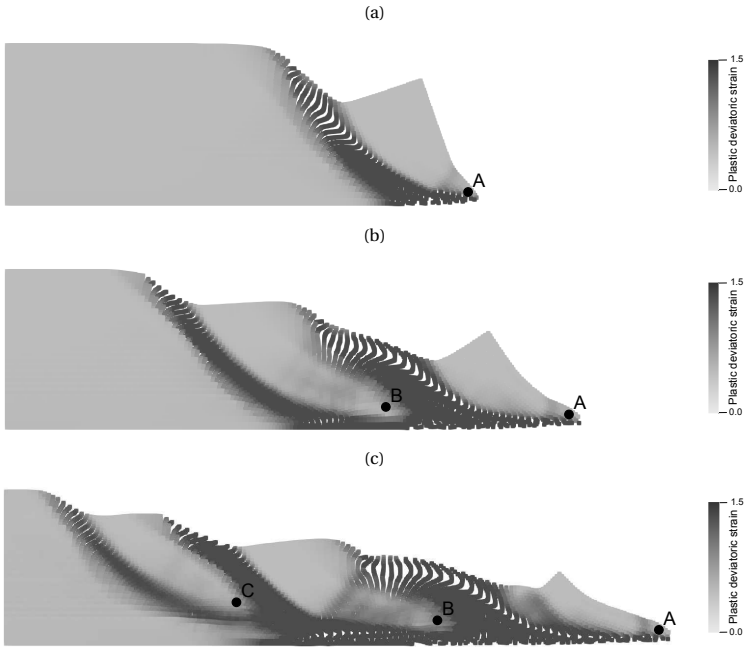

Figure 2.16: Deformation and plastic deviatoric strains of the vertical cut at a gravity load of a) .87, b) 1.22, and c) 1.65 g

These results demonstrate MPM can reasonably simulate large deformation mechanical problems. In an attempt to quantifiably validate the MPM results, three FEM simulations have been performed. These FEM results were obtained using the Total Lagrangian FEM (TL-FEM), in which the initial configuration of the vertical cut is considered in each solution step to compute equilibrium. In the first simulation (Figure 2.17a), a TL-FEM vertical cut (which has the same discretisation as the MPM vertical cut) has been simulated. Then, to replicate the progressive failure mechanism, a second simulation has been performed (Figure 2.17b) in which the elements comprising the

block of soil that has failed were removed. In the last simulation (Figure 2.17c), the same procedure as in the second simulation was carried out, i.e. the elements comprising the second block of soil that has failed have been removed. To compare both simulations (i.e. TL-FEM and MPM reults), Figure 2.18 is included, in which the displacement of each failing block of soil is shown at the points A, B and C from Figure 2.16. The first failure (1st Failure) displacements are obtained from point A. In this case, both simulations show similar results; the failure is triggered at almost the same gravity load, and the distance reached is almost the same. The second failure (2nd Failure) displacements are obtained from point B. Again, MPM and TL-FEM results are similar. The third failure (3rd Failure) displacements are obtained from point C. In this case, it is seen that the TL-FEM slope is triggered well before the MPM slope, which can be attributed to the lack of support at the right side of the slope (where the soil has been removed). Also, the distance reached by the soil using TL-FEM is larger compared to the MPM analysis.

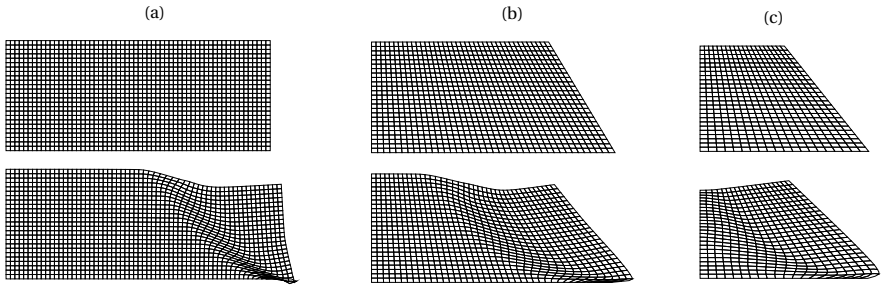

Figure 2.17: Initial and final mesh configurations after and before the a) 1st Failure, b) 2nd Failure, and c) 3rd Failure

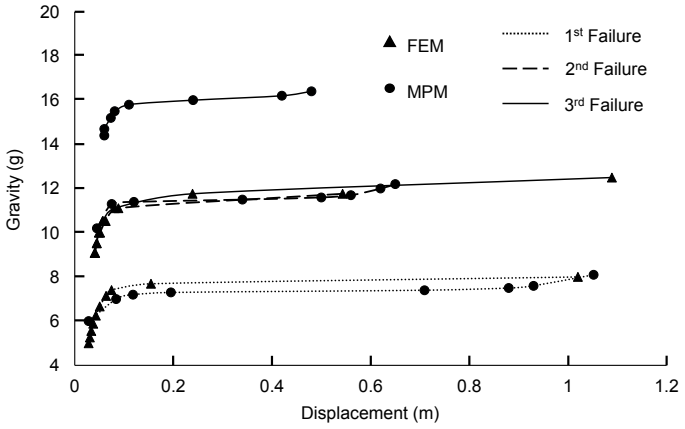

Figure 2.18: Gravity versus displacement for MPM and FEM simulations of retrogressive failure

Although the deformations of the vertical cut appear similar to the results presented

in literature, the inaccuracies observed in Figure 2.12 are also observed in this simulation. Figure 2.19 shows the deviatoric stresses developed inside the slope for the same steps presented in Figure 2.16. In Figure 2.19a, large oscillations are observed at the left side of the shear band. These oscillations are not large enough to cause the material to yield and therefore have limited influence in the simulation. However, the use of a different constitutive model could cause significant errors in the results. Figures 2.19b and 2.19c show the deviatoric stresses in the second and third failures of the vertical cut. In these figures, it is observed that the stresses in the failing body are also erratic.

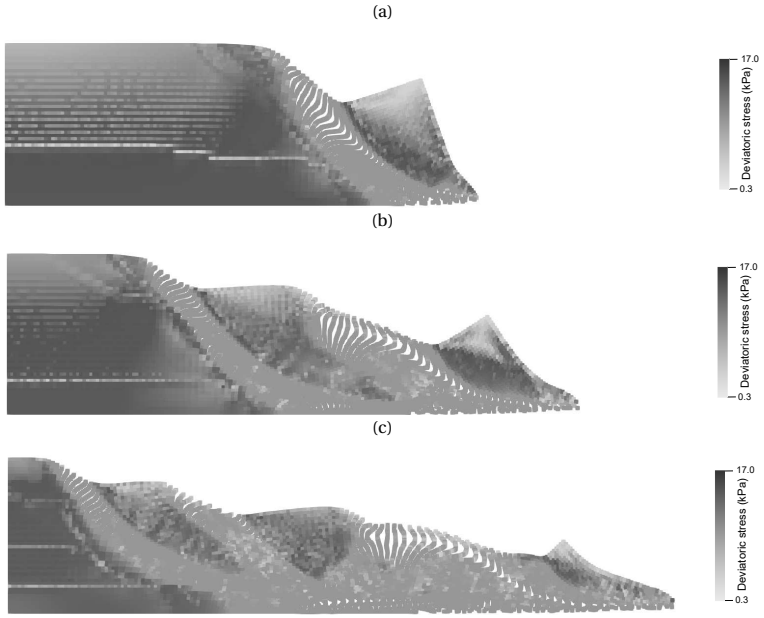

Figure 2.19: Deformation and deviatoric stresses of the vertical cut at a gravity load of a) .87, b) 1.22, and c) 1.65 g

2.8. CONCLUSIONS

The formulation of the static, explicit and implicit MPM has been elaborated, including the Newton-Raphson iteration procedure (static and implicit schemes) and Newmark's time integration scheme (implicit scheme). A proof of mass and momentum conservation for implicit MPM is given, adding to that available in the literature for the other methods. A summary of the algorithm steps followed in each solution scheme has been presented, and the key differences between the schemes were explained. Afterwards, three benchmark problems were introduced and analysed to demonstrate MPM behaviour and the behaviour of each solution scheme. It has been observed that the three schemes can simulate large deformations and the results obtained between the schemes are similar, which was expected. The first benchmark has demonstrated that MPM can convert kinetic energy to strain energy accurately and conserve the total energy in the system. Nevertheless, it has been observed that, using the implicit scheme, contact within simulations can cause numerical inaccuracies. These inaccuracies are associated with the

use of a constant-average-acceleration assumption. The second problem demonstrated inaccuracies caused by the movement of the material points through the domain. A typical solution used elsewhere in literature for this problem was introduced; however this solution is not generally applicable. Finally, the third benchmark has demonstrated that it is possible to simulate typical geomechanical problems using MPM. Using a material model which included softening, the simulation of progressive and retrogressive failures was shown to be feasible, and delivered results which are difficult or impossible to recreate using other numerical techniques such as FEM.

REFERENCES

Abe, K., Soga, K. & Bandara, S. (2013). Material point method for coupled hydromechanical problems. *Journal of Geotechnical and Geoenvironmental Engineering* **140**, No. 3, 04013033.

Alonso, E., Yerro, A. & Pinyol, N. (2015). Recent developments of the material point method for the simulation of landslides. In *IOP Conference Series: Earth and Environmental Science*, vol. 26, IOP Publishing, p. 012003.

Andersen, S. & Andersen, L. (2010). Modelling of landslides with the material-point method. *Computational Geosciences* **14**, No. 1, 137–147.

Bandara, S. & Soga, K. (2015). Coupling of soil deformation and pore fluid flow using material point method. *Computers and Geotechnics* **63**, 199–214.

Bathe, K.-J. (2006). *Finite element procedures*. Prentice Hall.

Bathe, K.-J. (2007). Conserving energy and momentum in nonlinear dynamics: a simple implicit time integration scheme. *Computers & Structures* **85**, No. 7-8, 437–445.

Belytschko, T., Liu, W. K., Moran, B. & Elkhodary, K. (2013). *Nonlinear finite elements for continua and structures*. John wiley & sons.

Beuth, L., Benz, T., Vermeer, P. A. & Więckowski, Z. (2008). Large deformation analysis using a quasi-static material point method. *Journal of Theoretical and Applied Mechanics* **38**, No. 1-2, 45–60.

Brackbill, J. U., Kothe, D. B. & Ruppel, H. M. (1988). Flip: a low-dissipation, particle-in-cell method for fluid flow. *Computer Physics Communications* **48**, No. 1, 25–38.

Brackbill, J. U. & Ruppel, H. M. (1986). Flip: A method for adaptively zoned, particle-in-cell calculations of fluid flows in two dimensions. *Journal of Computational physics* **65**, No. 2, 314–343.

Cheng, X., Zheng, G., Soga, K., Bandara, S., Kumar, K., Diao, Y. & Xu, J. (2015). Post-failure behavior of tunnel heading collapse by MPM simulation. *Science China Technological Sciences* **58**, No. 12, 2139–2152.

Chong, K., Jiang, C., Ram, D., Santhanam, A., Terzopoulos, D., Benharash, P., Dutson, E., Teran, J. & Eldredge, J. D. (2017). Visualization of vascular injuries in extremity trauma. *Medical & Biological Engineering & Computing* **55**, No. 9, 1709–1718.

Coetzee, C., Vermeer, P. & Basson, A. (2005). The modelling of anchors using the material point method. *International Journal for Numerical and Analytical Methods in Geomechanics* **29**, No. 9, 879–895.

Davies, A. J. (2011). *The finite element method: An introduction with partial differential equations*. Oxford University Press, Oxford.

Deuflhard, P., Krause, R. & Ertel, S. (2008). A contact-stabilized newmark method for dynamical contact problems. *International Journal for Numerical Methods in Engineering* **73**, No. 9, 1274–1290.

Fern, E. J. (2019). Modelling tunnel-induced deformations with the material point method. *Computers and Geotechnics* **111**, 202–208.

Gao, M., Pradhana, A., Han, X., Guo, Q., Kot, G., Sifakis, E. & Jiang, C. (2018). Animating fluid sediment mixture in particle-laden flows. *ACM Transactions on Graphics (TOG)* **37**, No. 4, 149.

González Acosta, J. L., Vardon, P. J., Guido, R. & Hicks, M. A. (2020). An investigation of stress inaccuracies and proposed solution in the material point method. *Computational Mechanics* **65**, No. 2, 555–581.

González Acosta, J. L., Vardon, P. J., Hicks, M. A. & Pantev, I. (2018). The use of MPM to estimate the behaviour of rigid structures during landslides. In *NUMGE 2018: 9th European Conference on Numerical Methods in Geotechnical Engineering*, vol. 9, CRC Press.

González Acosta, J. L., Zheng, X., Vardon, P., Hicks, M. & Pisano, F. (2019). On stress oscillation in MPM simulations involving one or two phases. *Proceedings of the 2nd International Conference on the Material Point Method for "Modelling Large Deformation and Soil–Water–Structure Interaction"* , 135–139.

Guilkey, J. E. & Weiss, J. A. (2003). Implicit time integration for the material point method: Quantitative and algorithmic comparisons with the finite element method. *International Journal for Numerical Methods in Engineering* **57**, No. 9, 1323–1338.

Harlow, F. H. (1957). Hydrodynamic problems involving large fluid distortions. *Journal of the ACM (JACM)* **4**, No. 2, 137–142.

Harlow, F. H. (1964). The particle-in-cell computing method for fluid dynamics. *Methods in Computational Physics* **3**, 319–343.

Harlow, F. H., Evans, M. W. & Harris Jr, D. (1956). The particle-in-cell method for two-dimensional hydrodynamic problems. *Technical report*, Los Alamos Scientific Lab., N. Mex.

Kohv, M., Talviste, P., Hang, T. & Kalm, V. (2010). Retrogressive slope failure in glaciolacustrine clays: Sauga landslide, western Estonia. *Geomorphology* **124**, No. 3-4, 229–237.

Lindgren, L. E. & Edberg, J. (1990). Explicit versus implicit finite element formulation in simulation of rolling. *Journal of Materials Processing Technology* **24**, 85–94.

Locat, A., Leroueil, S., Bernander, S., Demers, D., Jostad, H. P. & Ouehb, L. (2011). Progressive failures in eastern Canadian and Scandinavian sensitive clays. *Canadian Geotechnical Journal* **48**, No. 11, 1696–1712.

Lorenzo, R., da Cunha, R., Cordão Neto, M. & Nairn, J. (2017). Numerical simulation of installation of jacked piles in sand using material point method. *Canadian Geotechnical Journal* **55**, No. 1, 131–146.

Mason, M., Chen, K. & Hu, P. G. (2014). Material point method of modelling and simulation of reacting flow of oxygen. *International Journal of Computational Fluid Dynamics* **28**, No. 6-10, 420–427.

Mast, C. M., Arduino, P., Miller, G. R. & Mackenzie-Helnwein, P. (2014). Avalanche and landslide simulation using the material point method: flow dynamics and force interaction with structures. *Computational Geosciences* **18**, No. 5, 817–830.

Mitchell, R. & Klugman, M. (1979). Mass instabilities in sensitive canadian soils. *Engineering Geology* **14**, No. 2-3, 109–134.

Müller, A. & Vargas, E. A. (2019). Stability analysis of a slope under impact of a rock block using the generalized interpolation material point method (gimp). *Landslides* **16**, No. 4, 751–764.

Newmark, N. (1959). A method of computation for structural dynamics. *Journal of the Engineering Mechanics Division* **85**, No. 3, 67–94.

Phuong, N., Van Tol, A., Elkadi, A. & Rohe, A. (2016). Numerical investigation of pile installation effects in sand using material point method. *Computers and Geotechnics* **73**, 58–71.

Sloan, S. W. (1987). Substepping schemes for the numerical integration of elastoplastic stress–strain relations. *International Journal for Numerical Methods in Engineering* **24**, No. 5, 893–911.

Sloan, S. W., Abbo, A. J. & Sheng, D. (2001). Refined explicit integration of elastoplastic models with automatic error control. *Engineering Computations* **18**, No. 1/2, 121–194.

Smith, I. M., Griffiths, D. V. & Margetts, L. (2013). *Programming the finite element method*. John Wiley & Sons.

Soga, K., Alonso, E., Yerro, A., Kumar, K. & Bandara, S. (2015). Trends in large-deformation analysis of landslide mass movements with particular emphasis on the material point method. *Géotechnique* **66**, No. 3, 248–273.

Sołowski, W. & Sloan, S. (2015). Evaluation of material point method for use in geotechnics. *International Journal for Numerical and Analytical Methods in Geomechanics* **39**, No. 7, 685–701.

Stomakhin, A., Schroeder, C., Chai, L., Teran, J. & Selle, A. (2013). A material point method for snow simulation. *ACM Transactions on Graphics (TOG)* **32**, No. 4, 102.

Sulsky, D., Chen, Z. & Schreyer, H. L. (1994). A particle method for history-dependent materials. *Computer Methods in Applied Mechanics and Engineering* **118**, No. 1-2, 179–196.

Sulsky, D., Zhou, S.-J. & Schreyer, H. L. (1995). Application of a particle-in-cell method to solid mechanics. *Computer Physics Communications* **87**, No. 1-2, 236–252.

Tran, Q. A. & Sołowski, W. (2019). Generalized interpolation material point method modelling of large deformation problems including strain-rate effects–application to penetration and progressive failure problems. *Computers and Geotechnics* **106**, 249–265.

Wang, B. (2017). *Slope failure analysis using the material point method*. Ph.D. thesis, Delft University of Technology.

Wang, B., Vardon, P. J. & Hicks, M. A. (2016a). Investigation of retrogressive and progressive slope failure mechanisms using the material point method. *Computers and Geotechnics* **78**, 88–98.

Wang, B., Vardon, P. J., Hicks, M. A. & Chen, Z. (2016b). Development of an implicit material point method for geotechnical applications. *Computers and Geotechnics* **71**, 159–167.

Woo, S. I. & Salgado, R. (2018). Simulation of penetration of a foundation element in tresca soil using the generalized interpolation material point method (gimp). *Computers and Geotechnics* **94**, 106–117.

Zhang, X., Sheng, D., Sloan, S. W. & Bleyer, J. (2017). Lagrangian modelling of large deformation induced by progressive failure of sensitive clays with elastoviscoplasticity. *International Journal for Numerical Methods in Engineering* **112**, No. 8, 963–989.

3

AN INVESTIGATION OF STRESS INACCURACIES AND PROPOSED SOLUTIONS IN THE MATERIAL POINT METHOD

Stress inaccuracies (oscillations) are one of the main problems in the material point method (MPM), especially when advanced constitutive models are used. The origins of such oscillations are a combination of poor force and stiffness integration, stress recovery inaccuracies, and cell crossing problems. These are caused mainly by the use of shape function gradients and the use of material points for integration in MPM. The most common techniques developed to reduce stress oscillations consider adapting the shape function gradients so that they are continuous at the nodes. These techniques improve MPM, but problems remain, particularly in two and three dimensional cases. In this chapter, the stress inaccuracies are investigated in detail, with particular reference to an implicit time integration scheme. Three modifications to MPM are implemented, and together these are able to remove almost all of the observed oscillations.

Parts of this chapter have been published in González Acosta *et al.* 2017 and González Acosta *et al.* 2020.

3.1. INTRODUCTION

Many researchers have shown that MPM can be used to analyse some of the most common geotechnical problems, such as slope stability (Beuth *et al.* 2008, Alonso *et al.* 2015, Wang *et al.* 2016a, Bandara & Soga 2015, González Acosta *et al.* 2018), foundation installation (Phuong *et al.* 2016, Lorenzo *et al.* 2017, Sołowski & Sloan 2015) and anchors (Coetzee *et al.* 2005). However, the accuracy of MPM, in particular relating to the stress fields, is still far from the desired level. Indeed, it is noted that many publications do not display full results of the stresses, either presenting only deformations or limited data, and that the majority of work presented in the literature so far uses simple constitutive models. In some work, the stress oscillations and inaccuracies are acknowledged, and mainly attributed to the use of discontinuous finite element (FE) shape function (SF) gradients (e.g. Steffen *et al.* 2008a, Steffen *et al.* 2008b, Zhang *et al.* 2011, Andersen & Andersen 2009). Hence, a number of techniques have been developed to keep the SF gradients continuous between element boundaries, i.e. C1-continuous, for example:

- GIMP (Bardenhagen & Kober 2004), which distributes the influence of each material point over a characteristic or support domain, possibly extending the influence to multiple elements at a time. Both the SF and the SF gradients are modified.
- CPDI (Sadeghirad *et al.* 2011), which is an extension of GIMP in which the material point support domain can deform, maintaining the interaction between particles even after large extension. There are a number of CPDI variants, with different orientations and behaviour of the support domain.
- B-spline MPM (Steffen *et al.* 2008a), which replaces the linear SFs by functions with higher-order B-spline basis functions, which are at least C1-continuous and positive definite.
- DDMP (Zhang *et al.* 2011), which preserves the linear SFs and replaces the SF-gradients by smooth continuous functions, thereby allowing the usage of a local integration procedure rather than having a material point support domain.

These techniques have been proven to reduce the impact of cell-crossing. Meanwhile, other techniques use material point integration together with Gauss point integration to reduce numerical inaccuracies (Jassim 2013, Liang *et al.* 2019). However, a complete investigation of the causes of the stress inaccuracies has not been presented. Moreover, these techniques typically involve explicit MPM schemes, thereby ignoring the errors the proposed solutions can cause in the integration of the stiffness matrix in implicit schemes and in not exploiting the advantages of implicit time integration. Finally, examples have often been investigated only for 1D cases (usually with 2D elements), so that oscillations caused by other deformations, e.g. material rotation or distortion, have not been examined.

This chapter first presents two benchmark problems to illustrate the oscillation problem. In Section 3.3, the main causes of stress oscillations are investigated. Then, a series of existing and novel solutions are presented and investigated. Finally, a comparison of regular MPM and the new proposed oscillation-free MPM is given for the

simulation of a vertical cut failure, in order to demonstrate the relative performance for a problem involving both 2D geometry and elasto-plasticity.

3.2. BENCHMARKS

Two benchmarks are introduced to demonstrate and investigate the inaccuracies which occur in MPM. The first benchmark consists of an elastic quasi-static axisymmetric problem. The second benchmark is a 2D dynamic, elasto-plastic, vertical cut problem.

3.2.1. AXISYMMETRIC BENCHMARK

The first benchmark is similar to that presented by Naylor (1974) and Mar & Hicks (1996) to explore stress recovery. It consists of a hollow cylinder which deforms due to an incremental pressure (Δp_s) applied on the internal boundary (s). The main benefit of this benchmark is that, unlike a 1D plane strain problem, the stresses inside the elements are not constant; moreover, they deviate from the real solution and, depending on the material point position, the deviation may be large or small.

Figures 3.1a and 3.1b show the initial conditions of the benchmark; that is, the top view of the cylinder and the finite element discretization of the cylinder wall, respectively. In both Figures, the position of the boundary material point is shown (i.e. the material point nearest to the cylinder axis), which is used to determine the position of the boundary (s). Figure 3.1c and 3.1d illustrate that, during the loading, the distance r_i to the inner wall (s) changes, and is equal to the distance between the cylinder axis and the nearest active node (this implies that r_i remains constant until the boundary material point jumps to the next element). To enable the numerical (large deformation) solution to be interpreted in terms of the analytical (small strain) solution, the methodology includes the following three features: 1) The applied pressure (Δp_s) on the boundary (s) is applied to the outer nodes of the elements containing the outer most material points; 2) Due to the new location of the inner wall, Δp_s is re-evaluated as $\Delta p_s(r_i) = A/r_i^2 + 2\Psi$, where A and Ψ are constants associated with the initial geometry and boundary conditions of the benchmark, as shown in Figure 3.2 (a description of the analytical solution and the constants A and Ψ are presented in Appendix A.2); 3) Instead of accumulated stresses, incremental stresses at the material points are used throughout the analysis. These three features ensure that the incremental stress at the material points, for an arbitrary position of the cylinder wall, can be compared to the analytical stress related to the original geometry of the cylinder. The inner (initial) and outer cylinder boundaries are located at $r_i = 0.5$ m and $r_e = 1.5$ m, respectively. The cylinder domain is discretised by elements of dimension $\Delta r = \Delta y = 0.20$ m, and each element initially contains four material points equally spaced. The elastic properties are Young's modulus, $E = 1000 kN/m^2$, and Poisson's ratio, $\upsilon = 0.3$. The initial applied pressure increment is $\Delta p_s = 100$ kPa, and A and C are 19.56 and 10.87, respectively.

In Figure 3.3, the incremental stress invariants (deviatoric stress Δq and mean stress Δp) at material point mp_1 are plotted and compared to the analytical solution over 25 Δp_s increments. It is evident that the stress invariants can deviate strongly from the analytical solution.

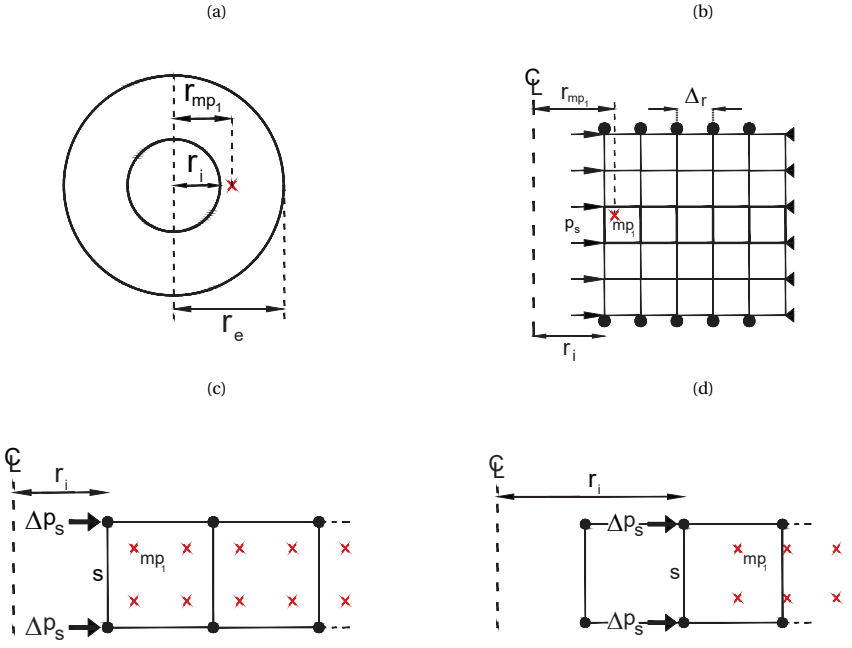

Figure 3.1: Axisymmetric model of a hollow cylinder under internal pressure. a) top view of the benchmark, b) domain and boundary conditions, c) initial internal boundary location, and d) internal boundary location at a given step

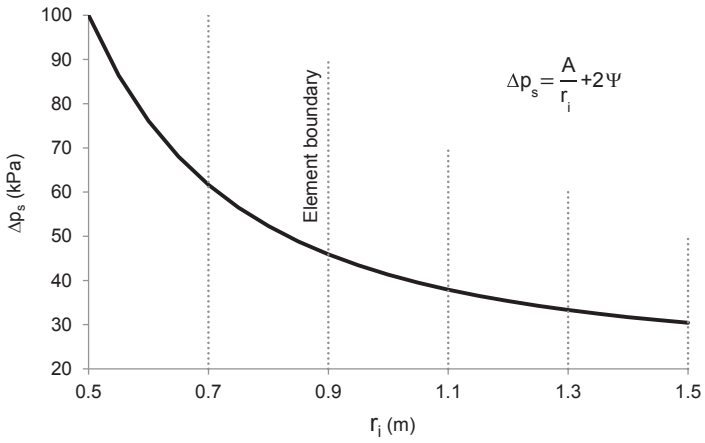

Figure 3.2: Incremental pressure (Δp_s) as a function of r_i

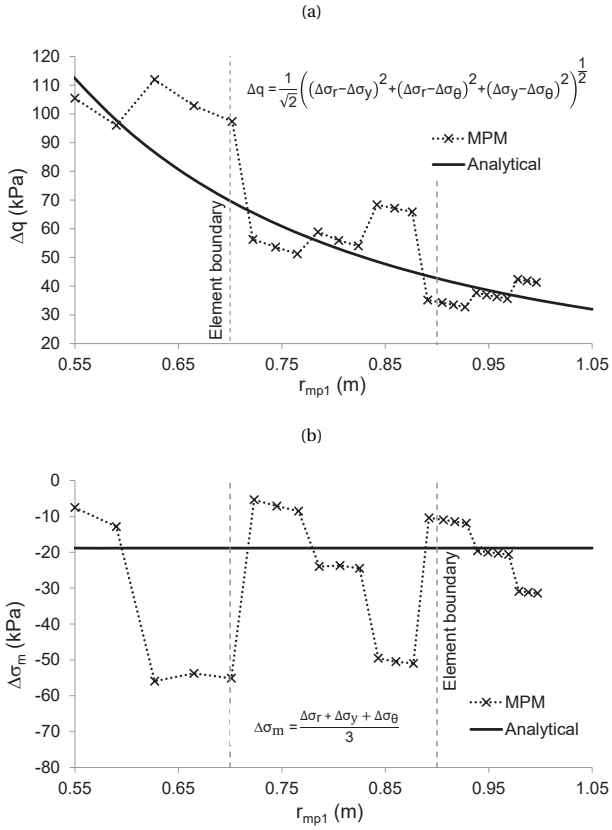

Figure 3.3: Evolution of mp1 stresses relative to r_{mp1}. a) deviatoric stress Δq, and b) mean stress $\Delta\sigma_m$

3.2.2. VERTICAL CUT BENCHMARK

A 2D plane strain elasto-plastic vertical cut problem (similar to that simulated in Section 2.7.3) has been simulated using the Von Mises constitutive model incorporating post-peak softening as described in Wang *et al.* 2016b. Figure 3.4 shows the domain, boundary conditions and discretisation. The height H of the cut and length L of the domain are 3.0 m and 6.0 m, respectively; the element size is $\Delta x = \Delta y = 0.10$ m and each element contains initially four equally distributed material points. The elastic parameters are E = 1000 kPa and $\upsilon = 0.35$, whereas the peak cohesion is $c_p = 12$ kPa, the residual cohesion is $c_r = 3$ kPa, and the softening modulus is $H_s = -30$ kPa. At the left boundary, the nodes are partly fixed to avoid displacement in the horizontal direction, whereas the nodes are fully fixed at the bottom boundary. The initial stresses in the domain are generated by fixing the locations of the material points and applying gravity loads until the internal and external forces are in equilibrium. After equilibrium is reached, the material points are released and deformation takes place.

Figure 3.5a and 3.5b shows contours of the deviatoric and mean stresses, respectively.

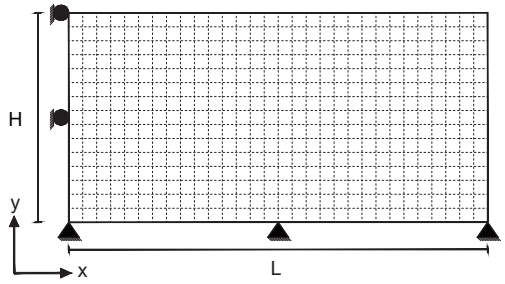

Figure 3.4: Sketch of the cutting stability problem

It is seen that during the movement of material points, both deviatoric and mean stress oscillations occur, although the overall failure mechanism is as expected. For Figure 3.5b, the shown range was fixed between 10 and -30 kPa because the oscillations are enormous in and around the shear band.

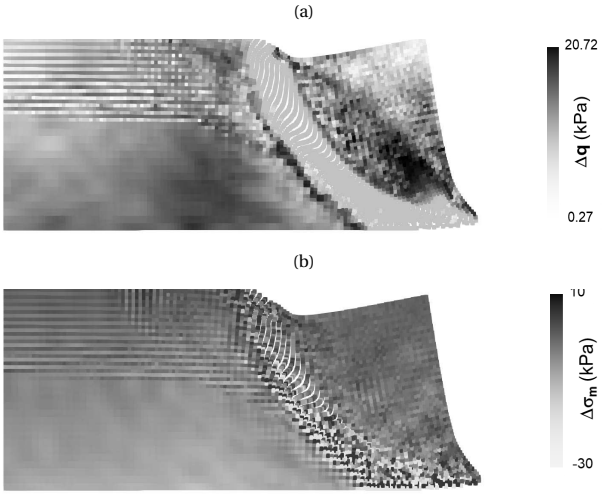

Figure 3.5: MPM stresses after 1.0 m of horizontal displacement at the toe. a) deviatoric stress, and b) mean stress

3.3. OSCILLATIONS IN MPM

The MPM technique can be seen as an FE stepwise procedure, in which the integration points (now called material points) move together with the mesh, but keep their new positions while the mesh returns to its original position. This allows the simulation of large deformations since extreme distortion of the mesh is avoided, although the process is found to cause stress oscillations. There are a number of contributing factors causing these oscillations, which are investigated below.

3.3.1. STRESS RECOVERY

As is typical in many implicit FEM formulations, displacements have been used as the primary variable and stresses are back-calculated using the strain-displacement matrix and the elastic matrix (eq. 2.38). During the back calculation of stresses an oscillation occurs, as may be observed by the stresses inside the elements, interpolated using the element SF gradients, deviating from the expected stresses (i.e. the stresses calculated using an analytical solution, referred to further as analytical stresses) except at the superconvergent positions (Naylor 1974, Barlow 1976, Zienkiewicz *et al.* 2005), which are locations inside the elements at which the stresses have a higher accuracy than at any other position. This problem is not observed in problems where the analytical stress is uniform across the element, e.g. as in a 1D bar. Figure 3.6 illustrates the radial stress inside a linear or quadratic axisymmetric element from Figure 3.1. It is seen that the computed stress distribution across the linear element (σ_L) is different from that across the quadratic element (σ_Q), and that both are different from the analytical stress (σ_A). However, the linear and quadratic stresses (σ_L and σ_Q, respectively) match the analytical solution exactly at the Gauss point locations. This means that, depending on the position of the material point, the recovered stresses can be either higher or lower than the analytical stresses, as illustrated in Figure 3.3.

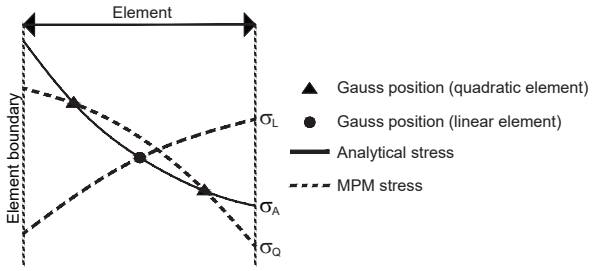

Figure 3.6: Radial stress inside an axisymmetric element

Figure 3.7 shows the analytical radial stress distribution and the stress recovered using MPM (or FEM) at any stress recovery position for the first load step in the axisymmetric benchmark. It is evident that the exact solution is near the centre of the elements, and recovering stresses at any other position will cause oscillations. It can also be seen that there will be a large oscillation whenever a material point crosses an element boundary, since the radial stress is discontinuous across inter-element boundaries.

3.3.2. NODAL INTEGRATION USING SF GRADIENTS

The nodal integrations of $\mathbf{F}^{\text{int}}$ and $\mathbf{K}$ are performed using SF gradients and the material point positions. However, considering that the SF gradients used in MPM are linear/plane (linear elements) and discontinuous between elements, and that the material point positions change each time step, the resulting nodal values are inaccurate, especially if material points cross element boundaries. Next, a description of the SF gradients in MPM and the consequences of using them are presented.

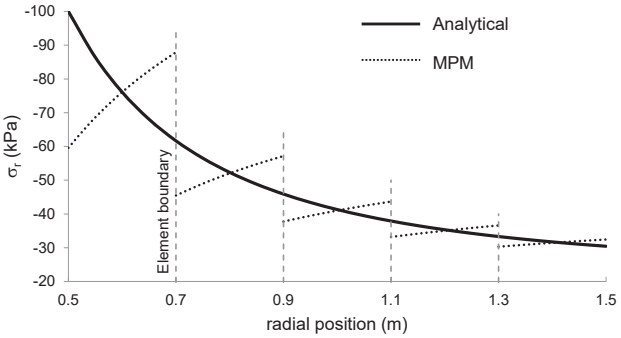

Figure 3.7: Analytical radial stress and stresses recovered using MPM in the axisymmetric benchmark

2D BI-LINEAR SHAPE FUNCTIONS

Figure 3.8 shows the SF (Figure 3.8b) and the horizontal and vertical SF gradients (Figure 3.8c, 3.8d) of node 1 of a 4-node square element (Figure 3.8a). It is noticed that the SF gradient is a maximum at the node, constant in the direction associated with the SF gradient, and decreases down to zero in the orthogonal direction. When a material point crosses an element boundary, the combination of the two element SFs must be considered.

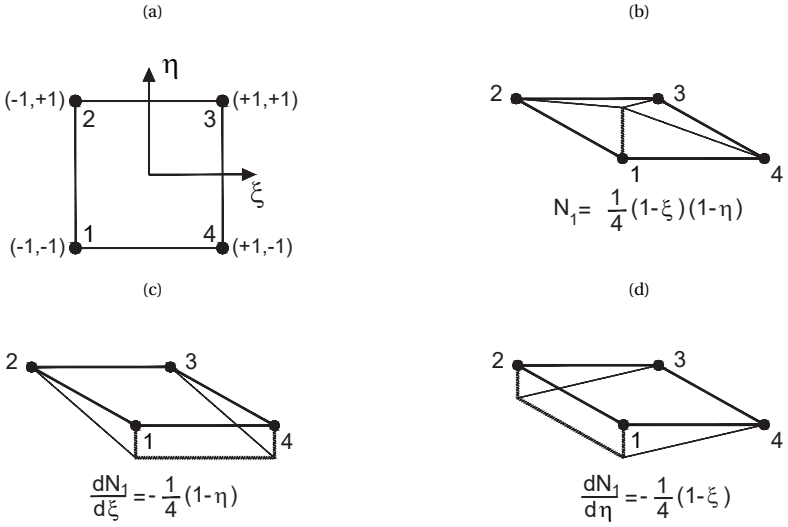

Figure 3.8: a) Element local numbering, b) regular SF associated with node 1, c) horizontal SF gradient associated with node 1, and d) vertical SF gradient associated with node 1. $\mathbf{N_i}$ is the shape function for node i, and ξ and η are local coordinates

In Figure 3.9, two elements are shown: E1 and E2 (Figure 3.9a). The SFs and SF gradients in both directions of node 5 are shown in Figure 3.9b, 3.9c and 3.9d, respectively. Figure 3.9b shows that the SFs are continuous between elements, while Figure 3.9d shows that the vertical SF gradient is continuous between elements in the horizontal direction

and constant in the vertical direction. On the other hand, Figure 3.9c shows that the horizontal SF gradients at the inter-element boundary are discontinuous, and that they decrease in the vertical direction.

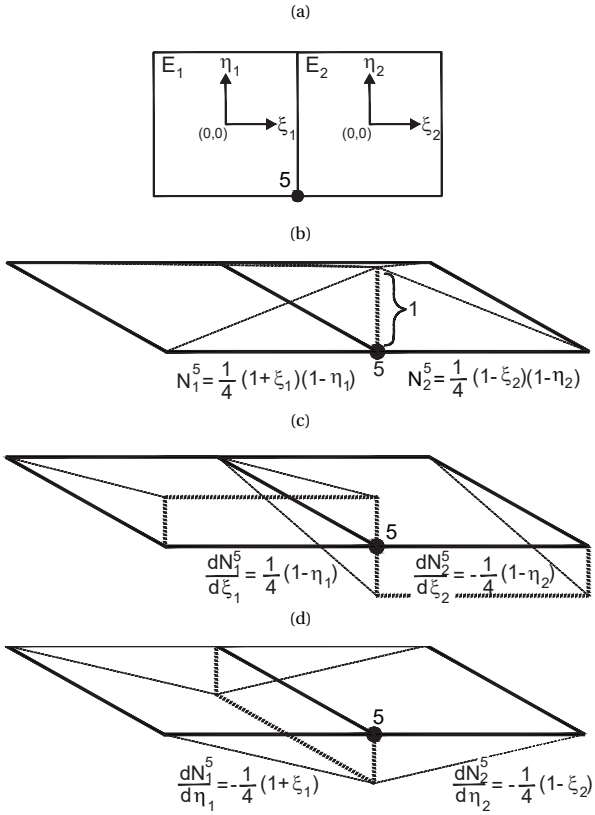

Figure 3.9: a) Connected elements E1 and E2, b) regular SFs for node 5, c) SF gradients in the horizontal direction, and d) SF gradients in the vertical direction. In this figure, the superscript and subscript refer to the node and element numbering, respectively

INTEGRATION OF THE INTERNAL FORCES $\mathbf{F}^{int}$ AND STIFFNESS $\mathbf{K}$

Since SF gradients must be used in the integration of any variable to compute nodal internal forces $\mathbf{F}^{int}$ and nodal stiffness [$\mathbf{K}$], it results in an inadequate distribution of such nodal quantities, whereas the distribution of nodal mass [$\mathbf{M}$] and nodal external forces $\mathbf{F}^{ext}$ is smoother due to the use of SFs. Moreover, $\mathbf{F}^{int}$ is computed using the strain-displacement matrix ($\mathbf{B}$) once (eq. 2.11), whereas the element stiffness is computed using both $\mathbf{B}$ and its transpose $\mathbf{B}^T$ (eq. 2.23), which causes additional inaccuracies when high-order SFs gradients are used to perform nodal integration procedures.

As an example of the inaccuracies caused by using SF gradients, the vertical and horizontal nodal internal force distributions (F_x and F_y) and the diagonal entries of the stiffness matrix (eq. 2.23) corresponding to the vertical and horizontal degrees of freedom

(K_x and K_y) using two different material point distributions, are computed for nodes 1-5 of the plane strain finite element mesh shown in Figure 3.10. In both cases the material points are equally distributed inside the elements; in the first case (Figure 3.10a) the material points are located inside each element, whereas in the second case (Figure 3.10b) the material points have moved and some are located at the inter element boundaries. After the movement, the material points are still located inside their original element, except for material points a-d which have crossed the boundary by an infinitesimal distance. Stress components of $\sigma_x = \sigma_y = -1.0$ MPa and $\sigma_{xy} = 0$, a Young's modulus of E = 1.0 kPa and a Poisson's ratio of $\upsilon = 0$ for each material point have been considered, while the distance between the nodes is 1 m and the material point weights are equal to 1.

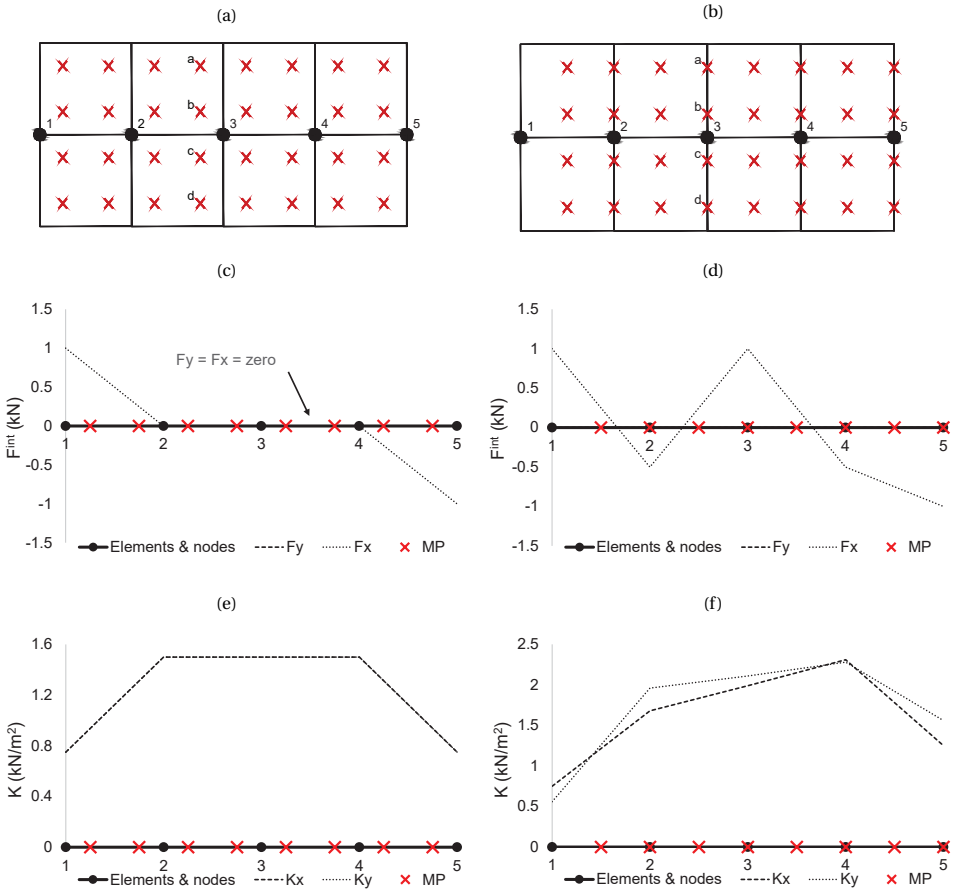

Figure 3.10: Investigation of internal forces and stiffness calculation using a) material points inside elements; and b) displaced material points where some material points (e.g. a - d) have crossed the inter element boundaries. Nodal force distribution c) before boundary crossing and d) after boundary crossing, and stiffness distribution e) before boundary crossing and f) after boundary crossing

In Figure 3.10c and 3.10d, the vertical internal force is equal to zero in both cases. The force is unchanged because the horizontal displacement of the material points does not affect the values of the vertical SF gradients, and equals to zero because the internal vertical forces on both sides of the nodes are the same but with an opposite sign. However, the distribution of the horizontal internal force is highly inaccurate due to the material point crossing the element boundary and the discontinuity of the horizontal SF gradients (Figure 3.10d). When integrating the nodal stiffness, the horizontal and vertical stiffnesses are initially similar (Figure 3.10e). However, as the material points cross an element boundary (Figure 3.10f), the inaccuracies are evident again, although they are smaller than those of the internal forces. This is because the product $\mathbf{B}\mathbf{B}^{\mathrm{T}}$ returns positive nodal values, so avoiding the change in sign of the SF gradients.

3.3.3. NODAL INTEGRATION OF THE MASS $\mathbf{M}$ AND EXTERNAL FORCES $\mathbf{F}^{\mathrm{ext}}$ USING SFS

The integration of $\mathbf{M}$ and $\mathbf{F}^{\mathrm{ext}}$ is performed using SFs rather than SF gradients, so that discontinuities between elements do not occur. In this section, only the external forces caused by gravity are considered. Since a lumped form of the mass matrix is used, and also because of the partition of unity of SFs, any initial distribution of material points inside the elements results in the same nodal mass (or external force), as long as the distribution is symmetrical. As an example, Figure 3.11 shows two different material point distributions inside an element, but the nodal mass and nodal external force are the same in both cases.

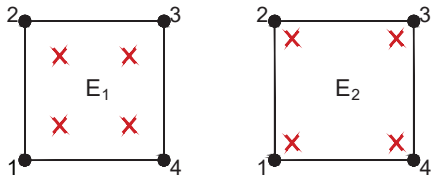

Figure 3.11: Different symmetric material point distributions in two elements

Figure 3.12 shows the distribution of $\mathbf{M}$ for the same problem as in Figure 3.10. It is clear that the movement of material points and the crossing of nodes does not cause any trouble for the nodal integration because of the continuity of the SFs. Also, since $\mathbf{F}^{\mathrm{ext}}$ is computed in a similar manner to $\mathbf{M}$, the distribution would be similar to the one in Figure 3.12.

3.3.4. STRESS REDISTRIBUTION DUE TO PLASTICITY

The stress oscillation caused by stress redistribution on the onset of plasticity is an extension of the oscillations explained in the previous sections. As the stresses exceeding the yield surface are integrated as a new external force computed with SF gradients, additional oscillations comparable to the $\mathbf{F}^{\mathrm{int}}$ oscillations are introduced. Moreover, oscillating stresses could cause some points to yield spuriously, leading to an unrealistic system behaviour.

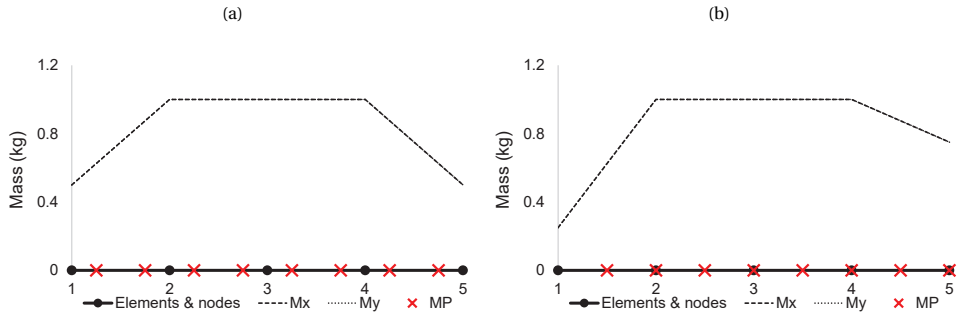

Figure 3.12: Nodal mass distribution considering a) initial material point distribution, and b) material point distribution after horizontal movement

3.4. IMPROVEMENTS TO REDUCE STRESS OSCILLATIONS

In FEM, high-order elements can be used to enhance the interpolation of strains within an element, improving the stresses recovered. In MPM, the use of such elements is not feasible (yet), since high-order SFs could produce a negative nodal mass, which is unfeasible. Additionally, the gradients of such SFs at the element interfaces remain discontinuous, causing large numerical inaccuracies during the movement of the material points between elements. Due to the unfeasibility of using such elements in MPM, several techniques have been developed, which can overcome the problems caused by using bi-linear SFs.

3.4.1. GIMP

The generalised interpolation material point (GIMP) method (Bardenhagen & Kober 2004) was proposed to reduce oscillations derived from material points crossing element boundaries. In GIMP, FE SFs are replaced by functions constructed based on the linear FE SF and a material point support domain (SD). This means that each material point has a domain over which its influence is distributed. The GIMP SF (S_{ip}) and its gradient (∇S_{ip}) in one dimension are computed as

$$S_{ip} = \frac{1}{V_p} \int_{\Omega_p \cap \Omega} \chi_p(\mathbf{x}) \mathbf{N}_i(\mathbf{x}) dx \tag{3.1}$$

$$\nabla S_{ip} = \frac{1}{V_p} \int_{\Omega_p \cap \Omega} \chi_p(\mathbf{x}) \nabla \mathbf{N}_i(\mathbf{x}) dx \tag{3.2}$$

where Ω is the problem domain, Ω_p is the material point support domain, i is the node, and χ_p is the characteristic function delimiting the area of influence of the material point and is originally presented as

$$\chi_p(x) \begin{cases} 1, & \text{if } x \cap \Omega_p \\ 0, & \text{otherwise} \end{cases} \tag{3.3}$$

Using the original definition of support domain given by Bardenhagen & Kober (2004), it would have a size of 2lp (lp = half of the material point support domain), which is

obtained by dividing the element size by the number of material points. In Figure 3.13, a 1D comparison between an FE SF and a GIMP SF is plotted, considering a distribution of two equally-distributed material points per element. It is seen that the GIMP SF and GIMP SF gradients are no longer exclusive to a single element and that the GIMP SF gradients are continuous between elements (as shown in the axisymmetric benchmark).

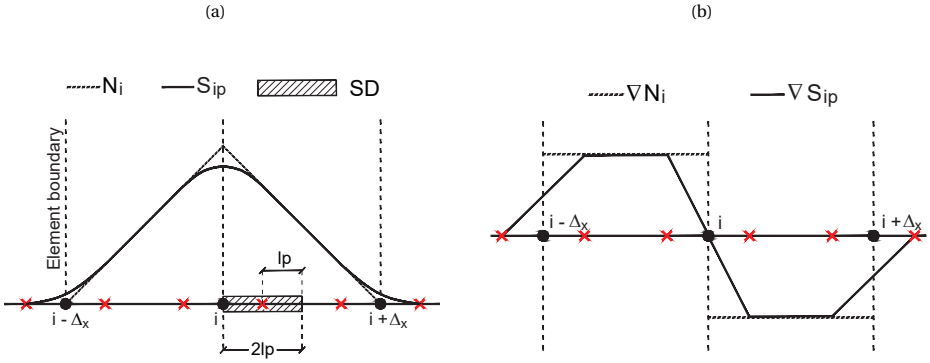

Figure 3.13: a) GIMP shape function (S_{ip}) and regular FE shape function ($\mathbf{N}_i$) of node i, and b) GIMP shape function gradient (∇S_{ip}) and regular FE shape function gradient ($\nabla \mathbf{N}_i$) for node i

The GIMP SFs in 2D and 3D are computed as products of the 1D GIMP SF in each direction; that is, $S_i(x) = S^1_{ip}(x_1) \cdot S^2_{ip}(x_2)$ in 2D and $S_i(x) = S^1_{ip}(x_1) \cdot S^2_{ip}(x_2) \cdot S^3_{ip}(x_3)$ in 3D, where S^k_{ip} is the 1D GIMP SF in the k-direction. An additional advantage of including a support domain is that the material boundary is explicitly defined, and can be used to apply boundary conditions.

3.4.2. MODIFIED INTEGRATION WEIGHTS

To reduce the problems caused by an irregular number of material points inside an element, it is here proposed to modify the material point integration weight to

$$W^* = W_p \frac{\text{omp}}{\text{cmp}} \tag{3.4}$$

where W^* is the modified material point weight (dimensionless), cmp is the current number of material points in the element, and omp is the original number of material points in the element. This modified weight is used considering only structured meshes, i.e. a mesh composed of equal-sized square elements, and equal mass material points, and its use with unstructured meshes or unequal mass material points is not part of this work. This modified weight technique, which compensates for the variation of the number of material points within an element, differs from the approach of other researchers who have modified the weights based on volumetric strain (e.g. Chen *et al.* 2017), which, while compensating for 1D deformations of the material points (compression or extension), does not reduce the problems caused by the rotation or advection of the material points. Finally, it should be noted that for four noded elements this modified weight value reduces to 4.0/cmp.

3.4.3. DOUBLE MAPPING (DM)

Integration using SF gradients is seen to work only at Gauss point locations, whereas material point integration is stable when based on SFs. Therefore, mapping to the Gauss point locations using shape functions (via the nodes) is proposed. As an example, the stiffness matrix is used. The elastic matrix is mapped to the nodes from the material points and then to the Gauss points, prior to the integration. Using FE SFs, the material point elastic matrix is mapped to the element nodes as

$$\mathbf{D}_i = \sum_{p=1}^{cmp} N_i(\mathbf{x}_p)\mathbf{D}_p W^* \tag{3.5}$$

where $\mathbf{D}_i$ is the elastic matrix at node i, and $\mathbf{D}_p$ is the elastic matrix of material point p. At this point, the total stiffness contribution of the material points is accumulated at the nodes, and this contribution is then redistributed to the original Gauss positions as

$$\mathbf{D}_g = \sum_{i=1}^{nn} N_i(\mathbf{x}_g)\mathbf{D}_i \tag{3.6}$$

where $\mathbf{D}_g$ is the elastic matrix at the Gauss point, $N_i(\mathbf{x}_g)$ is the nodal SF evaluated at the Gauss points, and nn is the number of nodes of the element. By substituting eq. 3.5 into eq. 3.6, $\mathbf{D}_g$ is obtained as

$$\mathbf{D}_g = \sum_{i=1}^{nn}\left(N_i(\mathbf{x}_g)\sum_{p=1}^{cmp} N_i(\mathbf{x}_p)\mathbf{D}_p W^*\right) \tag{3.7}$$

Finally, combining eq. 3.7 and eq. 2.23 (in FEM form) results in the nodal stiffness:

$$\mathbf{K} = \sum_{g=1}^{ngauss} \mathbf{B}^T(\mathbf{x}_g)\left[\sum_{i=1}^{nn}\left(N_i(\mathbf{x}_g)\sum_{p=1}^{cmp} N_i(\mathbf{x}_p)\mathbf{D}_p W^*\right)\right]\mathbf{B}(\mathbf{x}_g)\,|\mathbf{J}|\,W^{FE} \tag{3.8}$$

where ngauss is the number of Gauss points in the element and W^{FE} is the weight associated with Gauss point g (as in FEM).

3.4.4. DM-GIMP(DM-G)

As mentioned in Section 3.4.1, the GIMP method was created to avoid problems caused by the use of discontinuous FE SF gradients. However, a simple example in calculating the stiffness reveals a key problem. Figure 3.14 shows the same problem as in Figure 3.10, but in this case the stiffness is computed using regular SFs and GIMP SF gradients.

As shown in Figure 3.14a, for the initial configuration of material points, the horizontal nodal stiffness distributions remain the same for both techniques, because at this position the MPM and GIMP SF and SF gradients are the same. With the movement of the material points (Figure 3.14b), the horizontal nodal stiffness computed with GIMP decreases, as the GIMP SF gradients drop to zero at the inter-element boundaries (as shown in Figure 3.13). In addition, the contribution of material points in neighbouring elements is not capable of compensating for this drop. This would be the case for other methods, including DDMP and CDPI, that have this same characteristic.

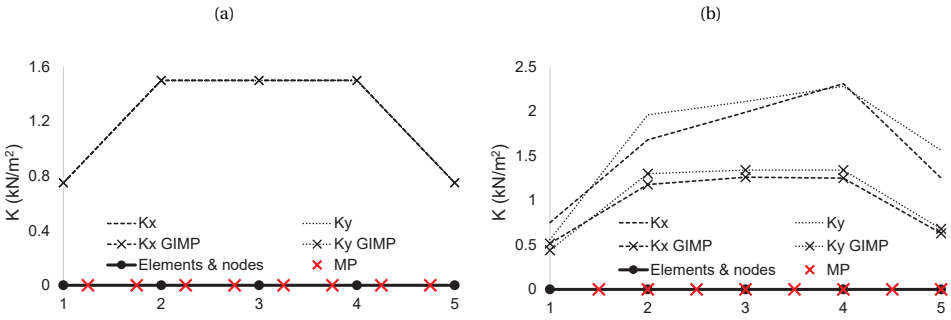

Figure 3.14: Nodal stiffness computed using regular SFs and GIMP SFs considering a) initial material point positions, and b) after displacement of material points

To overcome the problems of using GIMP to integrate nodal stiffness, it has been proposed that the double mapping approach be used alongside the local GIMP SFs (Charlton *et al.* 2017). The local GIMP SFs (S_{ip^*}) are similarly created as regular GIMP SFs, but the influence of the material point support domain affects only the nodal FE SF in a single element rather than contributing to all contiguous elements. In Figure 3.15, an illustration of the development of regular and local GIMP shape functions of a node is shown.

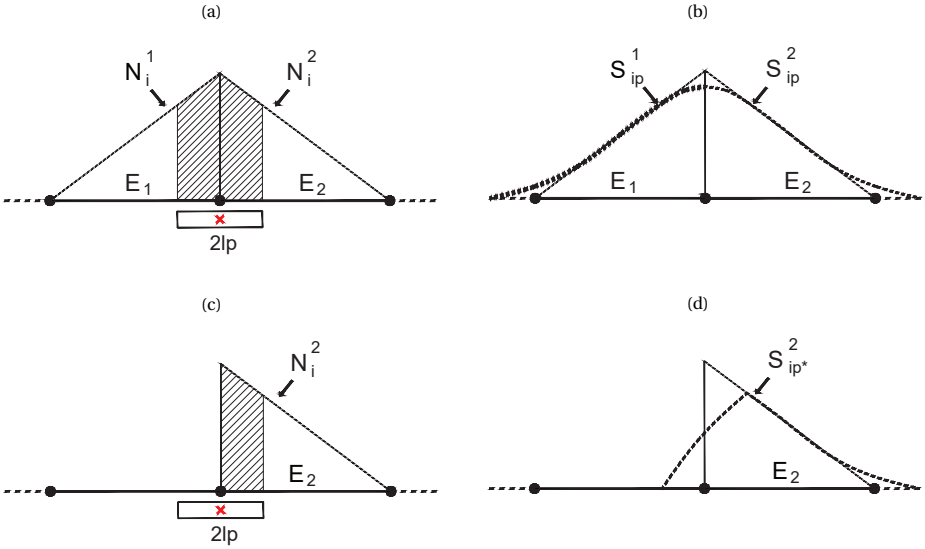

Figure 3.15: a) Nodal FE SF and interaction with the material point support domain, b) original GIMP SF (S_{ip}), c) nodal FE SF and interaction with the material point support domain in a single element, d) local GIMP SF (S_{ip^*})

In a similar manner to the double mapping technique using regular SFs, by using local GIMP SFs it is possible to distribute the elastic matrix to the nodes of an element and afterwards to the Gauss positions. The element stiffness matrix is then constructed as

$$\mathbf{K}_{el} = \sum_{g=1}^{ngauss} \mathbf{B}(\mathbf{x}_g)^T \left[\sum_{i=1}^{nn} \left(N_i(\mathbf{x}_g) \sum_{p=1}^{smp} S_{ip^*}(\mathbf{x}_p) \mathbf{D}_p W \right) \right] \mathbf{B}(\mathbf{x}_g) |\mathbf{J}| W^{FE} \tag{3.9}$$

where S_{ip^*} is the local GIMP SF of node i evaluated at the material point position, and smp is the number of material points with a support domain inside the element. Note that eq. 3.9 is similar to eq. 3.8, but instead of using N_i, S_{ip^*} is used. The algorithm to compute the stiffness matrix using DM and DM-G is given in Appendix B, together with a study of the computational performance.

3

3.4.5. COMPOSITE MATERIAL POINT METHOD (CMPM)

The composite material point method (CMPM) (González Acosta *et al.* 2017) is a modification of the composite finite element method (CFEM), proposed by Sadeghirad & Vaziri Astaneh (2011), in which the support domain used to recover the stresses is extended, i.e. a patch, improving the accuracy of the stresses computed. New shape functions enveloping all neighbouring elements of the element containing the material point are developed using Lagrange interpolation. In Figure 3.16, the C^2 shape functions are shown in 1D, in which each shape function N^2 envelopes the local element plus the neighbouring elements.

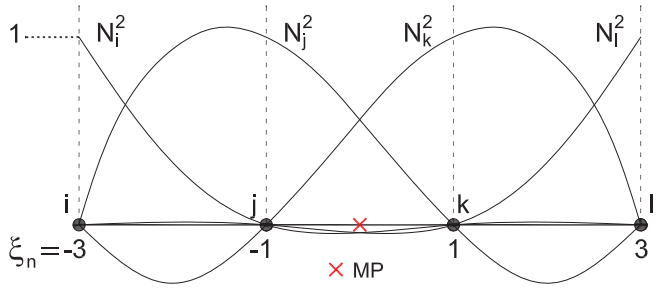

Figure 3.16: CMPM shape functions with C^2 continuity for a central local element

Using Lagrange interpolation, each of the N^2 shape functions is computed as

$$N_n^2(\xi) = \prod_{m=1;\, m\neq j}^{n} \frac{\xi - \xi_m}{\xi_j - \xi_m} \tag{3.10}$$

where ξ is the nodal local coordinate in the extended domain, n is the number of nodes, ξ_j is the local coordinate of the N_i^2 shape function, and ξ_m is the local coordinate of the remaining nodes. Solving eq. 3.10 for each node, the CMPM shape functions for an element with two neighbours are

$$\begin{bmatrix} N_i^2 \\ N_j^2 \\ N_k^2 \\ N_l^2 \end{bmatrix} = \frac{1}{16} \begin{bmatrix} -\frac{\xi^2 - 3\xi^2 - \xi + 3}{3} \\ \xi^2 - \xi^2 - 9\xi + 9 \\ -\xi^2 - \xi^2 + 9\xi + 9 \\ \frac{\xi^2 + 3\xi^2 - \xi - 3}{3} \end{bmatrix} \tag{3.11}$$

If the material point is located at the boundary, as in Figure 3.17, the CMPM shape functions are then

$$\begin{bmatrix} N_i^1 \\ N_j^1 \\ N_k^1 \end{bmatrix} = \frac{1}{4} \begin{bmatrix} \frac{\xi^2-4\xi+3}{2} \\ -\xi^2+2\xi+3 \\ \frac{\xi^2+4\xi+3}{2} \end{bmatrix} \tag{3.12}$$

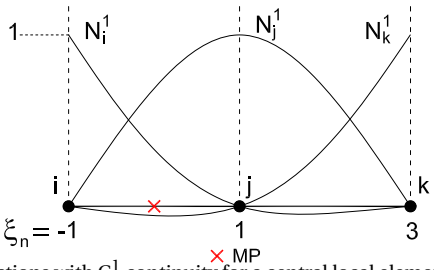

Figure 3.17: CMPM shape functions with C^1 continuity for a central local element

It is important to mention that although the CMPM SFs extend beyond the limits of an element, the range of the functions remains between $-1 \leq \xi \leq 1$. Also, this solution can only be used with a structured mesh. To extend the solution to a 2D domain, the new SFs are the product of the SFs in each direction.

3.4.6. IMPLEMENTATION OF DM-G AND CMPM

When DM-G is combined with CMPM (DM-GC), the (element) vectors of external and internal nodal forces are integrated using typical GIMP SFs Bardenhagen & Kober (2004) as

$$\mathbf{F}^{\text{ext}}|_{\text{elem}} = \sum_{p=1}^{\text{nmp}} \rho_p \mathbf{S}_{ip}^{\text{T}}(\mathbf{x}_p)\mathbf{b}\,|\mathbf{J}|\,W_p + \sum_{p=1}^{\text{bmp}} \mathbf{S}_{ip}^{\text{T}}(\mathbf{x}_p)\mathbf{s}_p^{\text{s}}\Gamma \tag{3.13}$$

$$\mathbf{F}^{\text{int}}|_{\text{elem}} = \sum_{p=1}^{\text{nmp}} \nabla\mathbf{S}_{ip}(\mathbf{x}_p)\boldsymbol{\sigma}_p\,|\mathbf{J}|\,W_p \tag{3.14}$$

where $\mathbf{S}_{ip}$ is the element matrix of GIMP SFs, and $\nabla\mathbf{S}_{ip}$ is the strain-displacement matrix for the GIMP SFs. Since the implicit solution scheme is used, the (element) stiffness matrix is computed using double mapping (DM) procedures as

$$\mathbf{K}|_{\text{elem}} = \sum_{g=1}^{\text{ngauss}} \mathbf{B}^{\text{T}}(\mathbf{x}_g) \left[\sum_{i=1}^{\text{nn}} \left(N_i(\mathbf{x}_g) \sum_{p=1}^{\text{cmp}} S_{ip*}(\mathbf{x}_p)\mathbf{D}_p W^* \right) \right] \mathbf{B}(\mathbf{x}_g)\,|\mathbf{J}|\,W^{\text{FE}} \tag{3.15}$$

And, the incremental stress of a material point is updated for the explicit and implicit schemes as

$$\Delta\boldsymbol{\sigma}_p = \mathbf{D}_p \nabla\mathbf{N}^2(\mathbf{x}_p)\,\Delta\bar{\mathbf{v}}^{\text{ext}} \tag{3.16}$$

and

$$\Delta\boldsymbol{\sigma}_p = \mathbf{D}_p \nabla \mathbf{N}^2 \left(\mathbf{x}_p\right) \Delta\bar{\mathbf{u}}^{ext} \tag{3.17}$$

where $\mathbf{N}^2$ is the (element) matrix of the CMPM SF gradients (equivalent to the strain-displacement matrix), and $\bar{\mathbf{u}}^{ext}$ and $\bar{\mathbf{v}}^{ext}$ are the vectors of nodal displacements and velocities, respectively, in the extended CMPM domain. Note that since GIMP and local GIMP SF are used to integrate both the forces and stiffness matrix, the stencil (i.e. support domain of each material point) is the same in both cases, including when using double mapping. CMPM uses an extended domain ($\bar{\mathbf{v}}^{ext}$ or $\bar{\mathbf{u}}^{ext}$) to recover stresses, which is not necessarily equal to the GIMP stencil. Finally, it is important to remark that the state variables (i.e. mass, velocity, acceleration) are mapped using GIMP SFs.

3.5. TESTING OF THE DOUBLE MAPPING TECHNIQUE TO COMPUTE NODAL STIFFNESS

Previously, it was demonstrated that SF gradients cause large inaccuracies when integrating variables to the nodes. By using GIMP, those inaccuracies reduced significantly, especially during the computation of internal nodal loads. Nevertheless, nodal stiffness inaccuracies remain, for which DM techniques have been developed. The testing strategy in this section is focused on the stiffness matrix. To compare the stiffness using each technique, the stiffness magnitude is used, and this is computed as

$$K_{mag} = \sqrt{K_x^2 + K_y^2} \tag{3.18}$$

where K_x and K_y are the diagonal entries of the stiffness matrix corresponding to the horizontal and the vertical degrees of freedom, respectively. The test consists of computing the stiffness of an infinite space made up of square elements that are full of equally spaced material points, four per element, as shown in Figure 3.18a. The infinite domain is then rotated 20^o degrees around its centre (C), as in Figure 3.18b. The elastic properties of the material are E = 1000 kN/m2 and $\upsilon = 0.30$. Figure 3.19 presents the stiffness computed using regular MPM and DM and the results are compared with the FEM stiffness, computed using four Gauss integration points ($K_{mag} = 3263.57 kN/m^2$). In addition, the stiffness using the modified integration weights (W*) and Gauss mapping (GM) separately (the two components of DM) are shown to highlight their comparative effects. Since the material points remain equally distributed after rotation, the stiffness of the domain should not change (i.e. be mesh independent). Finally, a further test is performed using two materials, by considering the properties of material points below line A - A' to be E = $1500 kN/m^2$ and $\upsilon = 0.25$.

Theoretically, the stiffness of the domain should be independent of the rotation of the field of material points, and should be equal to the FEM stiffness before rotation (for the case with one material). As can be observed in Figure 3.19, the stiffness obtained using regular MPM is not accurate and improvements are needed. After including the modified integration weight (W*), which accounts for a varying amount of material points per element, the stiffness distribution oscillates, although with a different spatial pattern than in regular MPM. Using GM the oscillation also persists, as the number of material points per cell is still incorrect, but it is less than in regular MPM because it helps to reduce errors due to material point position. It is noted that including W* and GM separately are

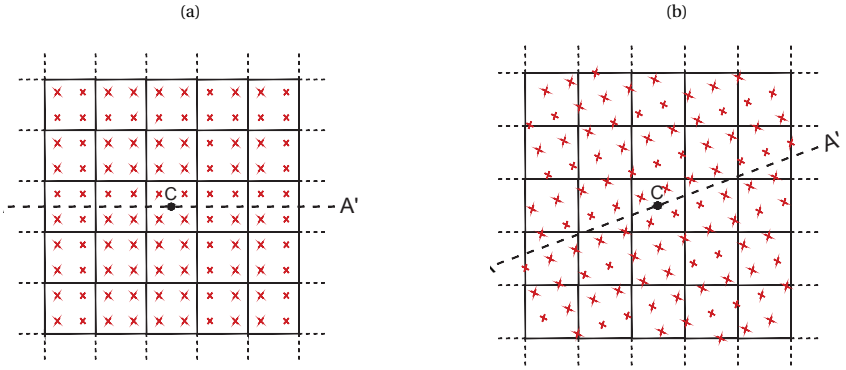

Figure 3.18: Infinite domain full of equally spaced material points (a) before and (b) after rotation

unable to fix the stiffness oscillation, and that the spatial distribution is almost opposite in pattern, i.e. where high values occur in GM, low values occur in W*, and vice versa. Using DM, i.e combining GM and W*, the stiffness oscillation is reduced significantly as it accounts for both the material point position and the number of material points per element. Moreover, the transition is smooth over the elements when two materials are used. In Figure 3.20, the tests from Figure 3.18 have been performed using GIMP and DM-G. As can be observed, the stiffness obtained using GIMP integration is significantly more inaccurate when compared to MPM integration, as it both oscillates and reduces in magnitude. Note that the results for GIMP are shown using a different contour range; this is because using GIMP SF gradients the stiffness reduces significantly, and it is necessary to change the contour range to visualize the stiffness distribution. On the other hand, using DM-G the stiffness oscillation is reduced further than using DM. This is because the W* approach, which only allows the impact of a discrete number of points in each element to be considered, is not being used. Utilising DM-G allows a gradual transition of mass from one element to another. Moreover, using DM-G, the transitions between materials appears sharper than in regular FEM due to an increase in the accuracy of the material stiffness distribution between the interface nodes.

Method	Maximum increase (%)	Maximum decrease (%)
Regular MPM	5.51	-7.38
W*	5.93	-8.88
GM	4.75	-5.63
DM	2.23	-2.38
GIMP[a]	0.0	-33.95
DM-G	0.21	-0.39

[a] Using GIMP the stiffness only decreases with respect to FEM

Table 3.1: Relative differences in stiffness magnitude between FEM and other methods for homogeneous material

In Table 3.1, the difference between the stiffness obtained using each technique

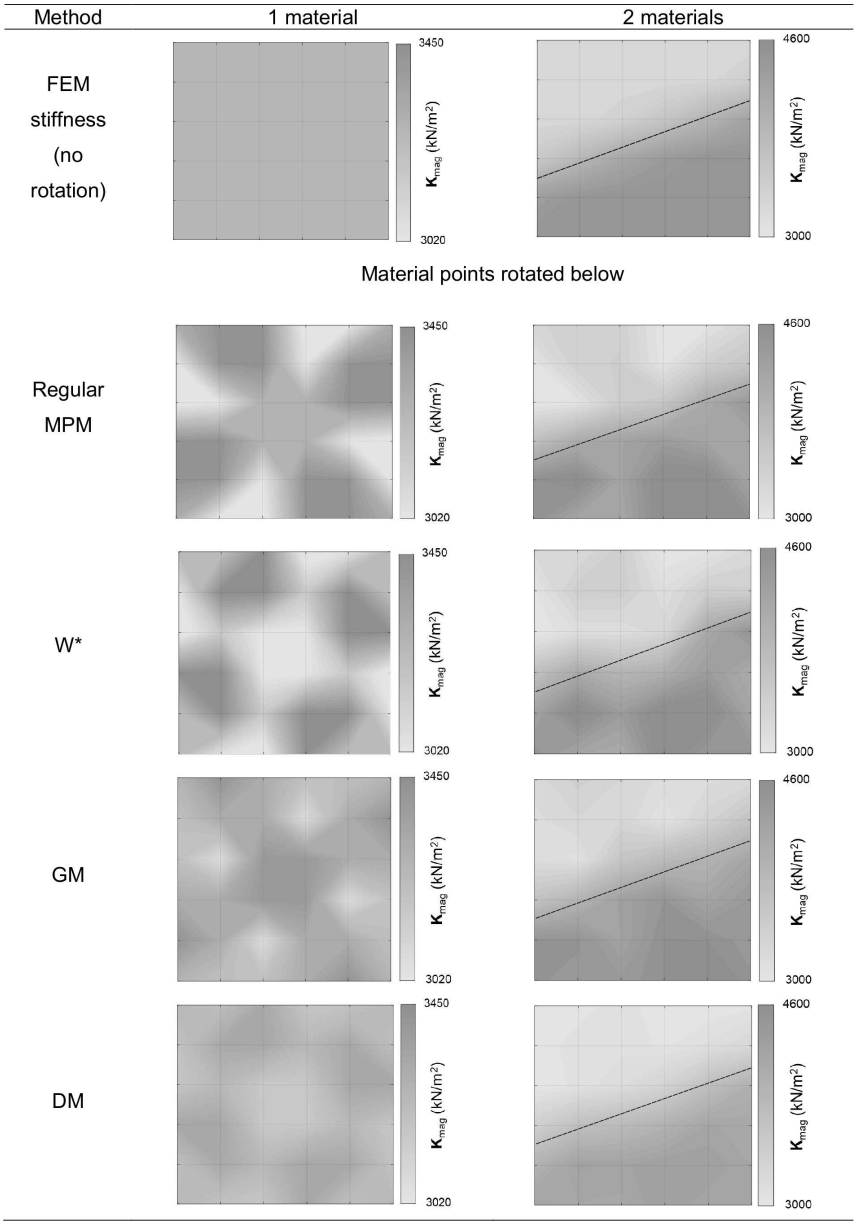

Figure 3.19: Stiffness distribution considering rotation of the domain, using one and two materials, computed with FEM, MPM, W*, GM and DM

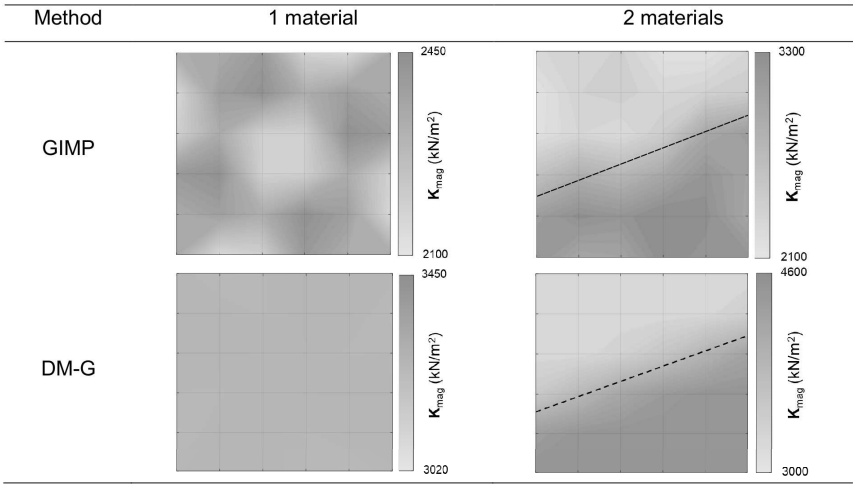

Figure 3.20: Stiffness distribution considering rotation of the domain, using one and two materials, computed with GIMP and DM-G

is shown relative to the nodal stiffness magnitude of the real FEM stiffness. In this comparison, only the homogenous material is considered. As can be observed, regular MPM and GIMP give large stiffness oscillations relative to the FEM stiffness, but in the case of GIMP the stiffness only decreases (as observed also in Figure 3.14b). Using only the modified integration weight the stiffness oscillation increases, whereas using the GM stiffness the oscillation decreases (compared to regular MPM), but not significantly. Using DM and DM-G, the dependence between the mesh and the position of the material points is reduced, and the nodal stiffness oscillations reduce significantly, especially using DM-G where the variation is smaller than 1%.

3.6. DM-GC BENCHMARKING

In this section, the DM-GC is tested using three benchmark problems. The first benchmark is a 1D elastic column subjected to an incremental gravity load. This benchmark is introduced to demonstrate the rate of convergence of DM-GC. The second and third benchmarks are those introduced in Section 3.2, which are now re-analysed using the improvements described in Section 3.4. Finally, all the benchmarks and geotechnical simulations introduced later are simulated using plane stress conditions.

3.6.1. 1D ELASTIC BAR CONVERGENCE

To demonstrate the accuracy of DM-GC, a 1D benchmark problem is analysed. This problem is similar to the benchmark analysed in Coombs *et al.* 2018, in which a 1D column made of material points is subjected to an incremental gravity force, whereas the number of square background elements (nel) is increased. In this benchmark, the initial gravity load is zero, and is increased using increments of $\Delta_g = 1.0 \times 10^{-4}$ until a maximum gravity load of $g_{SD} = 0.1g$ and $g_{LD} = 20g$, in which the first maximum gravity load (i.e. g_{SD}) is used to study small deformations, and the second (i.e. g_{LD}) to study large deformations.

The 1D bar has an initial height and width of H = 10 m and L = 1 m. The elastic parameters of the bar are Young's modulus, $E = 1.0 \times 10^3$ kPa, and Poisson's ratio, $\nu = 0.0$. The density of the material points is $\rho = 1500 kg/m^3$. The bar is fully fixed at the bottom, and fixed in the horizontal direction at both vertical sides. Each background element is filled (initially) with four material points equally spaced, and the simulations have been performed using the static scheme to avoid kinematic effects. The error through the calculations is measured as

$$\text{error} = \sum_{p=1}^{nmp} \frac{\left\| \sigma_{p,z} - \sigma_{a,z}(Z) \right\| V_p^0}{\left(\rho g H^0\right) V_{BAR}^0} \tag{3.19}$$

in which $\sigma_{p,z}$ is the material point vertical stress, $\sigma_{a,z}(Z)$ is the analytical vertical stress of the bar at the height z (i.e. $\sigma_{a,z} = \rho g(H - z)$, in which z is measured from the bottom), $\|\cdot\|$ is the L_2 norm of $(\cdot)$, V_p^0 is the initial material point volume, V_{BAR}^0 is the initial bar volume, and $\rho s H^0$ is the vertical stress at the bottom of the bar used to normalise the difference of stresses, in which H^0 is the initial bar height.

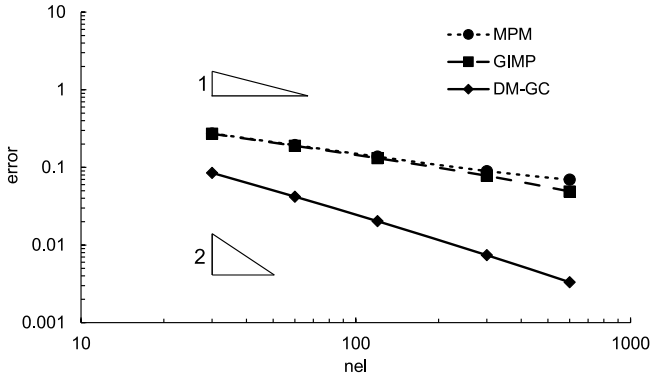

Figure 3.21: Convergence of MPM, GIMP, and DM-GC after a gravity load of 0.1g

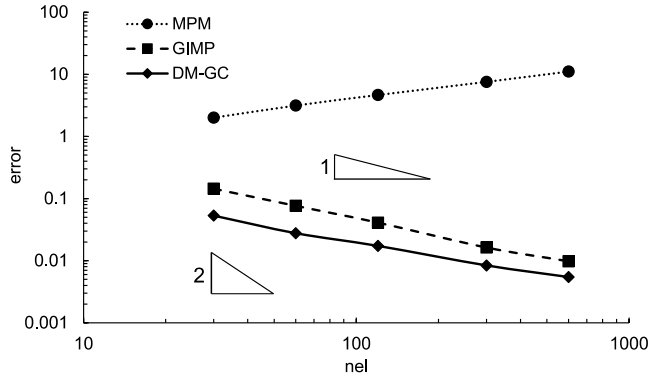

Figure 3.22: Convergence of MPM, GIMP, and DM-GC after a gravity load of 20g

Figure 3.21 shows the convergence of MPM, GIMP and DM-CG considering small deformations. It is observed that MPM and GIMP have the same convergence ($\alpha = 1$, in which α is the order of convergence). Nevertheless, it is observed that MPM error cannot reduce linearly at a certain point, which is attributed to the element crossing problem. On the other hand, using DM-GC, the order of convergence is $1 < \alpha < 2$. Figure 3.22 shows the results considering a large deformation. In this case, it is observed that MPM error grows due to the large number of material points crossing elements, which causes highly inaccurate internal stresses. On the other hand, the GIMP and DM-GC error reduces at a similar rate (with DM-GC having a smaller error).

3.6.2. AXISYMMETRIC BENCHMARK

Figure 3.7 showed the stress oscillation caused by using regular SFs to recover stresses in the cylinder wall. In Figure 3.23, GIMP and CMPM are compared against regular MPM for a single (i.e. the first) load step. As can be seen, the GIMP oscillation is the same as MPM close to the centre of the element, because there the SF gradients are the same for both techniques. However, stresses are continuous between the elements, due to the continuous gradients of GIMP. On the other hand, using CMPM the stresses remain discontinuous between elements, but the reduction of oscillation when compared to the analytical solution is significant.

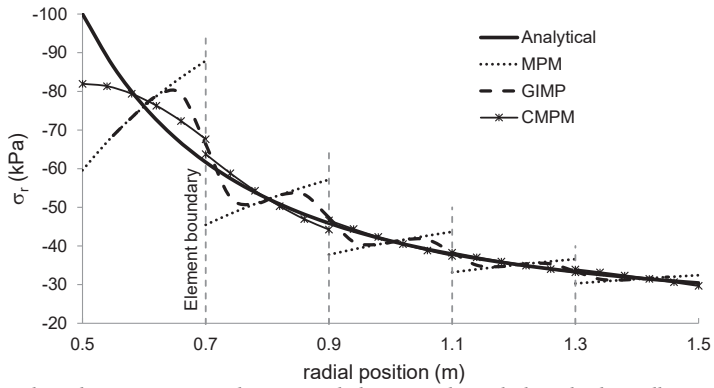

Figure 3.23: Analytical, MPM, GIMP and CMPM radial stresses through the cylinder wall

In Figure 3.24, the evolution of the incremental deviatoric and mean stresses of material point mp1 (over 25 load steps) are shown using normal MPM (as shown in Figure 3.3), DM and DM-CMPM (DM-C). As can be seen, there is a significant increase in the accuracy of the stresses recovered using the DM technique, due to the improved stress recovery and stiffness integration. Moreover, if CMPM is included in the analysis, the stress oscillation reduces still further to give stresses close to the analytical solution.

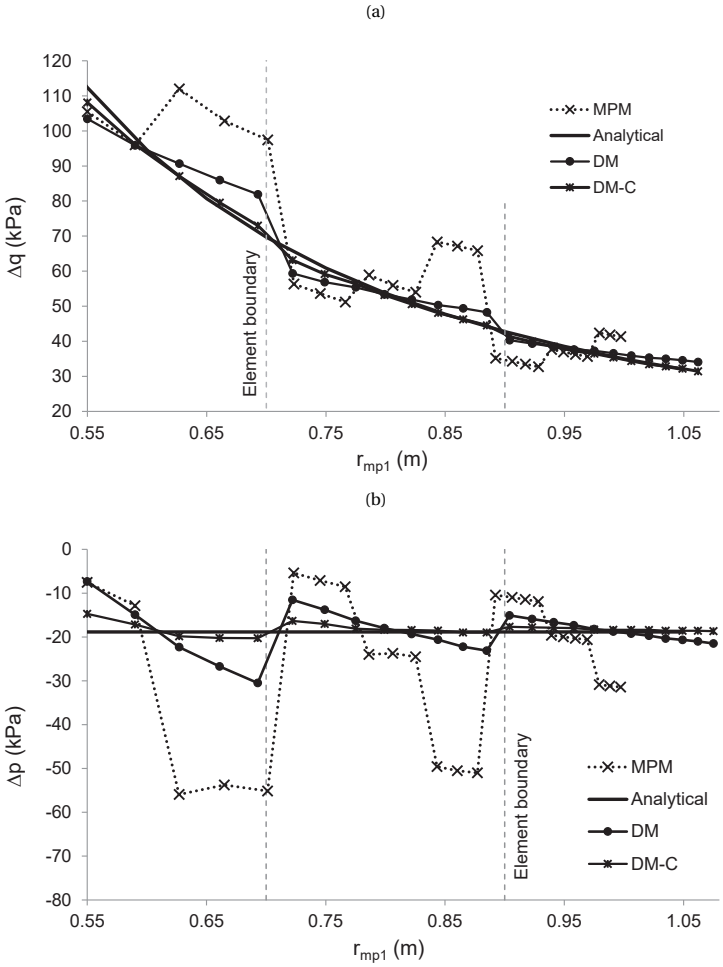

Figure 3.24: a) Deviatoric, and b) mean stress recovered from m_{p1} at different positions

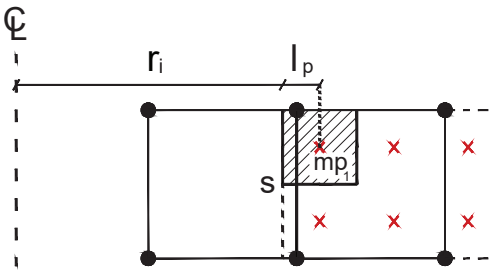

Figure 3.25: Internal boundary location at a given step using the GIMP support domain

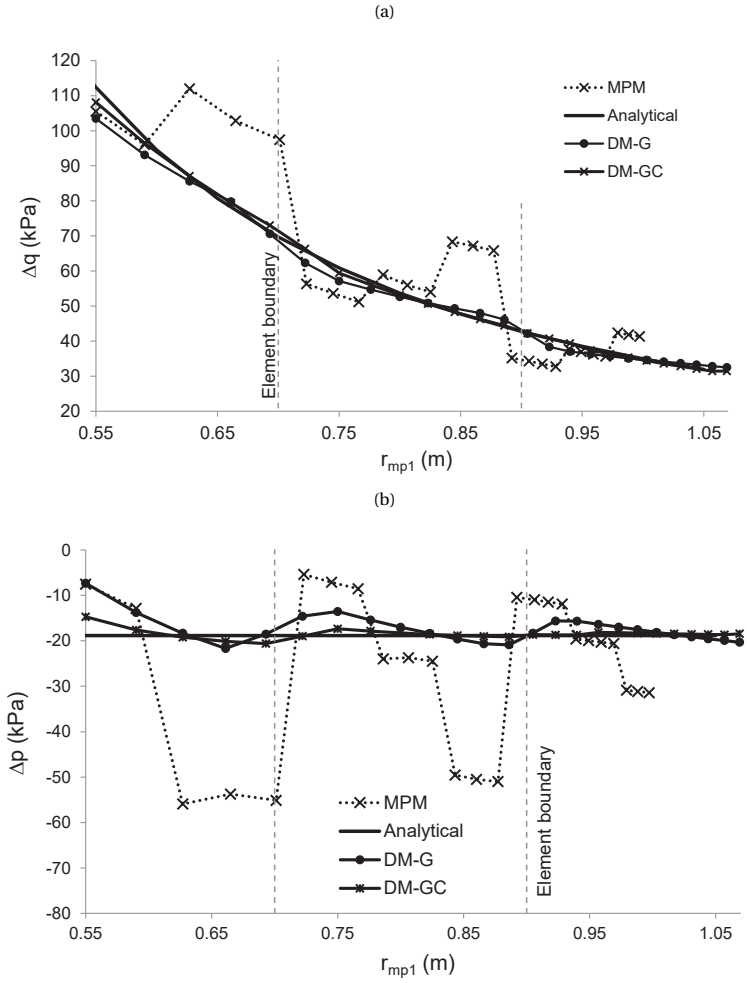

Figure 3.26: a) Deviatoric, and b) mean stress using DM-G and DM-GC

Next, the same example using DM-G and DM-GIMP-CMPM (DM-GC) is studied. Using DM-G, the stiffness is computed with the DM-G method and the stresses are recovered using GIMP SF. Using DM-GC, the DM-G method is again used to compute the stiffness, but the stresses are now recovered using CMPM rather than GIMP. In addition, since the inner wall boundary can be determined accurately using the material point support domain (as mention in Section 3.4.1), the distance between the cylinder axis and the inner boundary (s) is $r_i = r_{mp1} - l_p$ as in Figure 3.25. Then, the applied pressure Δp_s is distributed linearly to the nodes of the boundary element based on proximity.

In Figure 3.26 it can be seen that, using DM-G and DM-GC, the results approximate the analytical solution even better that DM and DM-C, respectively. This is because the stiffness computed using DM-G is closer to the FEM stiffness and also due to the accurate

distribution of the external pressure considering the accurate location of the internal boundary.

3.6.3. VERTICAL CUT BENCHMARK

Figure 3.27 shows the elastic stiffness magnitude in the vertical cut benchmark problem, using regular MPM and DM-GC. As can be observed in Figure 3.27(a) – (d), using regular MPM large stiffness oscillations occur, from the beginning (small deformations) up until the end (large deformations) of the analysis. In contrast, using DM-GC (Figure 3.27(e) – (h)) the stiffness oscillation reduces significantly, although some small oscillation can be observed in the shear band and along the edge of the domain.

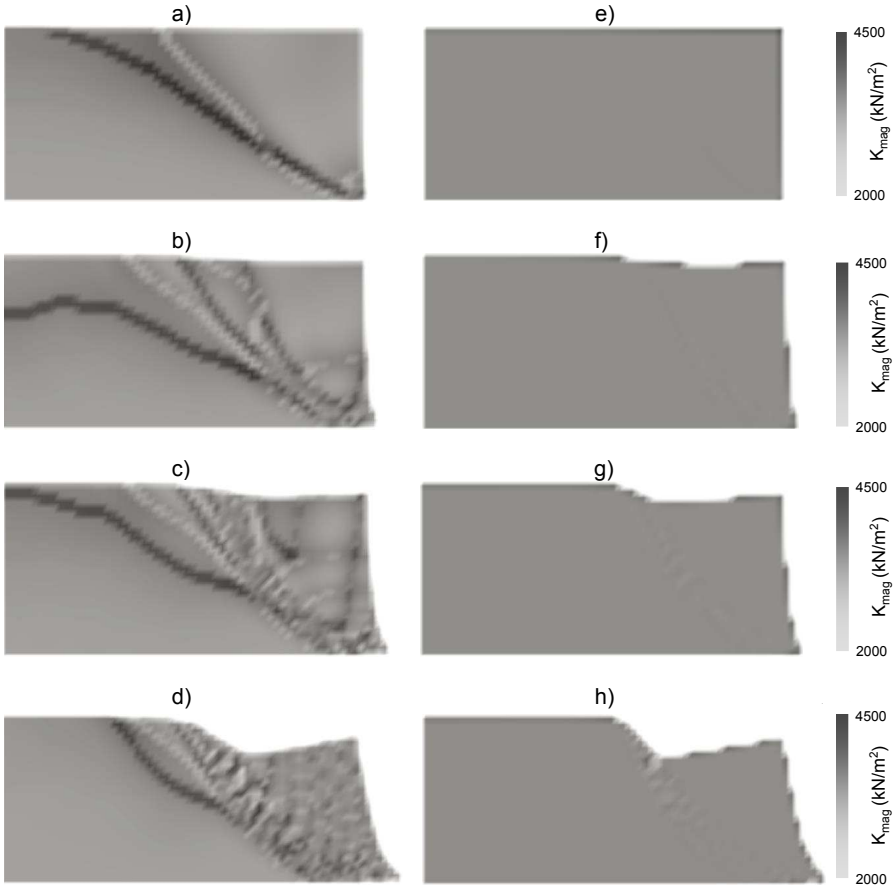

Figure 3.27: Stiffness magnitude in the body using regular MPM (a-d) and DM-GC (e-h) after a horizontal toe displacement of a & e) 0.10 m, b & f) 0.30 m, c & g) 0.50 m, and d & h) 1.0 m

In Figure 3.28 the nodal $\mathbf{F}^{int}$ magnitude is shown, once again comparing regular MPM and DM-GC. Analogous to eq.25, the magnitude of the nodal internal force is computed as

$$F^{int}_{mag} = \sqrt{F^{int}_x + F^{int}_y} \tag{3.20}$$

where F^{int}_x and F^{int}_y are the nodal internal forces for the horizontal and the vertical degrees of freedom, respectively. It is seen that if GIMP and CMPM are included in the solution, a large reduction in the oscillations of $\mathbf{F}^{int}$ is obtained. Using GIMP, the oscillation caused by the material points crossing cell boundaries are reduced. Furthermore, by including CMPM, the recovered stresses are improved, reducing the oscillation caused by the stress recovery position.

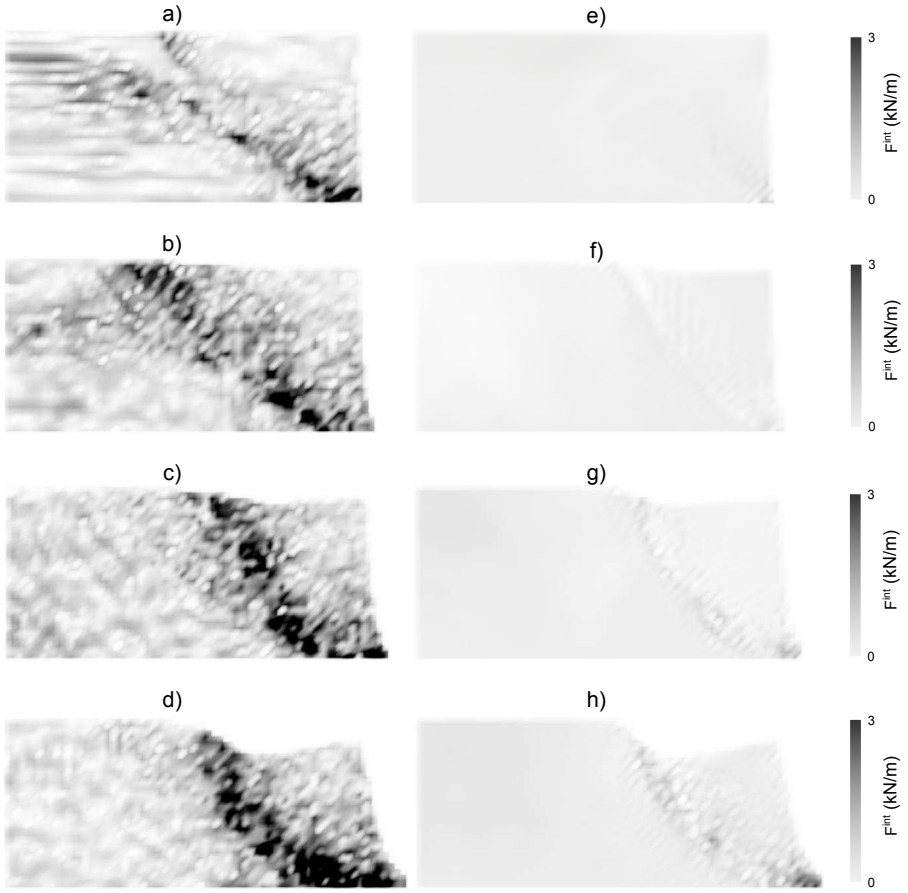

Figure 3.28: $\mathbf{F}^{int}$ magnitude in the body using regular MPM (a-d) and DM-GC (e-h) after a horizontal toe displacement of a & e) 0.10 m, b & f) 0.30 m, c & g) 0.50 m, and d & h) 1.0 m

Figure 3.29 shows the deviatoric stress contours from both analyses. It is evident that, after reducing the oscillation in the stiffness and the internal nodal forces by using DM-GC,

the deviatoric stress distribution in the domain is significantly smoother. Similarly, Figure 3.30 shows the comparison of mean stresses during the analyses, demonstrating that the mean stress oscillations are reduced with DM-GC. In this case, as in the axisymmetric benchmark, some oscillation of the mean stresses still occurs, but this is thought to be due to incompressibility during plastic yielding. For methods to reduce locking behaviour in MPM using low order shape functions the reader is referred to Coombs *et al.* (2018).

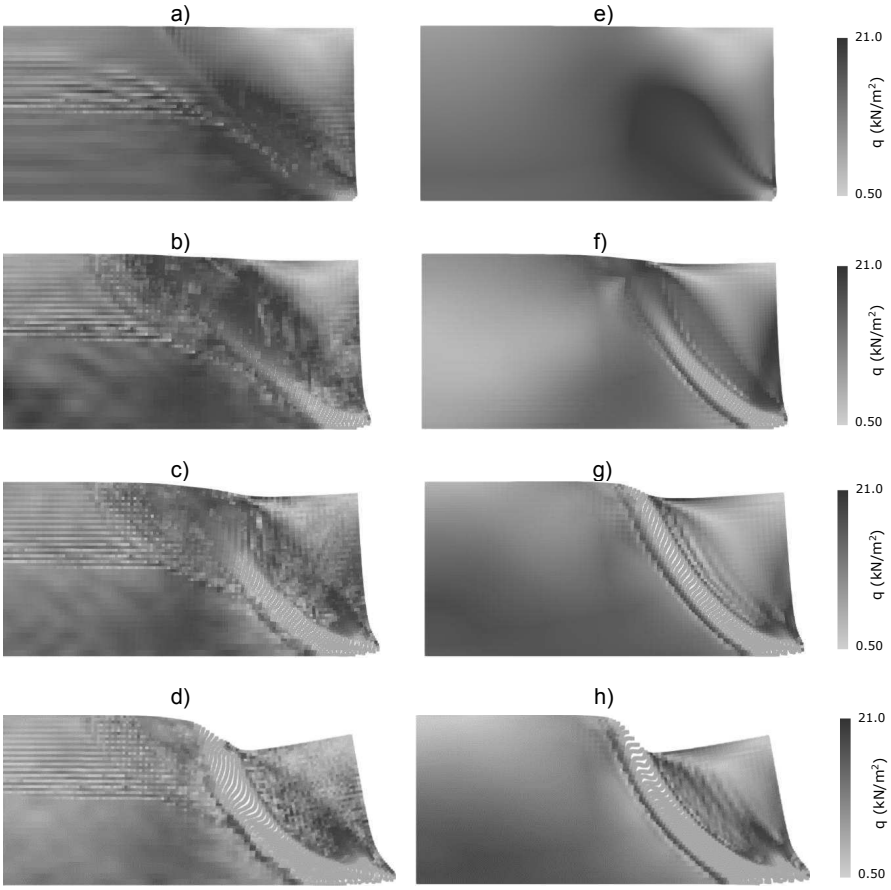

Figure 3.29: Deviatoric stress in the body using regular MPM (a-d) and DM-GC (e-h) after a horizontal toe displacement of a & e) 0.10 m, b & f) 0.30 m, c & g) 0.50 m, and d & h) 1.0 m

As can be seen from previous figures, the oscillation of material point stresses, nodal stiffness and internal nodal forces are reduced significantly using DM-GC. Plots for the nodal mass and external nodal forces are not included in the results since the oscillation for both MPM and DM-GC is small.

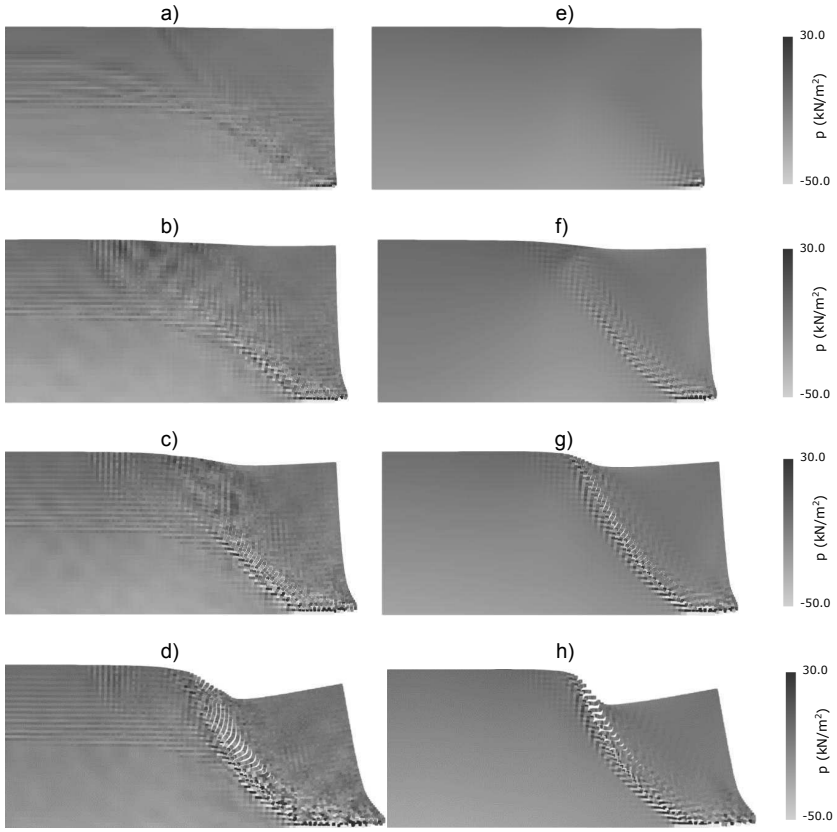

Figure 3.30: Mean stress in the body using regular MPM (a-d) and DM-GC (e-h) after a horizontal toe displacement of a & e) 0.10 m, b & f) 0.30 m, c & g) 0.50 m, and d & h) 1.0 m

Furthermore, p-q curves have been plotted for 3 material points at key positions in the soil body. Figure 3.31, shows the location of the points chosen; material point A is located at the toe of the cutting, material point B is found in the middle of the soil layer in the shear band, and material point C is in the centre of the sliding block.

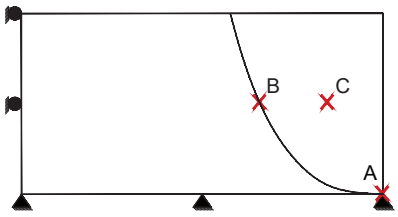

Figure 3.31: Material points selected to plot stresses in p-q space

Figure 3.32 shows the p-q stress paths at the 3 points, as computed using both techniques, as well as the initial position of the yield surface for a Von Mises material (FVM). It is seen that, for material point A, both techniques give reasonable results; this is because the bottom of the domain is fully fixed, so that the material point does not move much throughout the analysis. For material points B and C, if regular MPM is used (Figure 3.32 (b) and (c)), the oscillations are extreme. It is evident that were a constitutive model different from Von Mises to be used, in which plasticity does not depend only on the deviatoric stress, regular MPM would not perform well. On the other hand, using DM-GC, the stress path appears to be well-behaved (Figure 3.32 (e) and (f)), with only some small oscillations. Finally, based on the results obtained with the benchmarks and the geotechnical implementations, Table 3.2 summarises the advantages and disadvantages of each of the methods studied in this chapter.

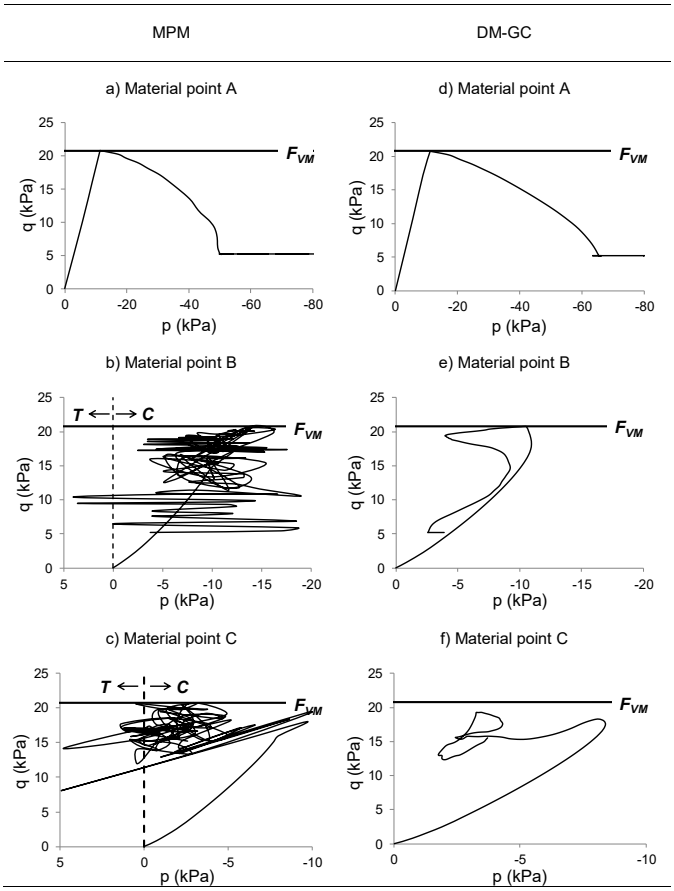

Figure 3.32: p-q curves using MPM (a,b and c), and DM-GC (d,e and f)

Table 3.2: Summary of advantages and disadvantages of the methods studied

Method	Oscillations of nodal Fint caused by		Oscillations of K caused by		Stress recovery
	MP position	MP CEB	MP position	MP CEB	-
MPM	Inaccurate distribution of internal forces	Large oscillations due to discontinuity of SF gradients	Increase if MP is close to the node, and decrease in some directions if MP is far from the node	Accumulation or reduction of MP's causes an increase or reduction of stiffness	Poor
GIMP	Decrease of oscillation by keeping conyinuity of SF gradients	Imbalance disappears because of continuity of SF gradients	Large stiffness oscillation	Stiffness vanishes if MP is at element boundary	Continuous between elements
DM-MPM	Inaccurate distribution of internal forces	Large imbalance due to discontinuity of SF gradients	Stiffness oscillation reduces	Stiffness oscillation reduces significantly by using the modified weighting value W*	Poor
DM-G	Decrease of oscillation by keeping continuity of SF gradients	Imbalance disappears because of continuity of SF gradients	Stiffness oscillation reduces significantly	Stiffness oscillation reduces significantly	Continuous between elements
DM-GC	Decrease of oscillation by keeping continuity of SF gradients	Imbalance disappears because of continuity of SF gradients	Stiffness oscillation reduces significantly	Stiffness oscillation reduces significantly	Highly improved by increasing the solution domain and SF order

MP: Material Point CEB: Crossing Element Boundary

3.7. CONCLUSIONS

MPM is a technique that is able to handle problems involving large deformations, since material properties and the body geometry are no longer attached to a mesh. Unfortunately, the use of regular bi-linear finite element shape functions causes significant oscillations when integrating internal forces and stiffness, decreasing the accuracy of the simulations. Moreover, the grid crossing of a material point between elements and poor stress recovery create additional oscillations. A series of improvements, both novel and building upon the work of others, have been studied and combined to obtain an almost oscillation free version of MPM. It has been shown that GIMP reduces the errors caused by grid crossing, but integration using SF gradients, shown via an example using the stiffness matrix, is inaccurate due to the use of SF gradients that drop to zero at the inter-element boundaries. Using GIMP together with a double mapping integration procedure significantly reduces the stiffness matrix oscillation. Also, it has been proven that CMPM increases the accuracy of the stresses computed at the material points compared to typical MPM and GIMP. These techniques combined (termed DM-GC) increases considerably the accuracy of the MPM simulations. Moreover, since it has been observed that DM performs well when using both typical finite element shape functions, and better still when using GIMP shape functions, the combination of DM with other C1-continuous methods, such as CPDI, B-spline MPM or DDMP, is a possibility which can be studied in the future. The DM and DM-G methods have the benefit of being able to be implemented implicitly or explicitly including typical elasto-plastic constitutive models.

REFERENCES

Alonso, E., Yerro, A. & Pinyol, N. (2015). Recent developments of the material point method for the simulation of landslides. In *IOP Conference Series: Earth and Environmental Science*, vol. 26, IOP Publishing, p. 012003.

Andersen, S. & Andersen, L. (2009). Analysis of stress updates in the material-point method. In *Proceedings of the 22nd Nordic Seminar on Computational Mechanics*, Citeseer, pp. 129–134.

Bandara, S. & Soga, K. (2015). Coupling of soil deformation and pore fluid flow using material point method. *Computers and Geotechnics* **63**, 199–214.

Bardenhagen, S. G. & Kober, E. M. (2004). The generalized interpolation material point method. *Computer Modeling in Engineering and Sciences* **5**, No. 6, 477–496.

Barlow, J. (1976). Optimal stress locations in finite element models. *International Journal for Numerical Methods in Engineering* **10**, No. 2, 243–251.

Beuth, L., Benz, T., Vermeer, P. A. & Więckowski, Z. (2008). Large deformation analysis using a quasi-static material point method. *Journal of Theoretical and Applied Mechanics* **38**, No. 1-2, 45–60.

Charlton, T., Coombs, W. & Augarde, C. (2017). igimp: An implicit generalised interpolation material point method for large deformations. *Computers & Structures* **190**, 108–125.

Chen, Z.-P., Zhang, X., Qiu, X.-M. & Liu, Y. (2017). A frictional contact algorithm for implicit material point method. *Computer Methods in Applied Mechanics and Engineering* **321**, 124–144.

Coetzee, C., Vermeer, P. & Basson, A. (2005). The modelling of anchors using the material point method. *International Journal for Numerical and Analytical Methods in Geomechanics* **29**, No. 9, 879–895.

Coombs, W. M., Charlton, T. J., Cortis, M. & Augarde, C. E. (2018). Overcoming volumetric locking in material point methods. *Computer Methods in Applied Mechanics and Engineering* **333**, 1–21.

González Acosta, J. L., Vardon, P. J. & Hicks, M. A. (2017). Composite material point method (cmpm) to improve stress recovery for quasi-static problems. *Procedia Engineering* **175**, 324–331.

González Acosta, J. L., Vardon, P. J., Hicks, M. A. & Pantev, I. (2018). The use of mpm to estimate the behaviour of rigid structures during landslides. In *NUMGE 2018: 9th European Conference on Numerical Methods in Geotechnical Engineering*, vol. 9, CRC Press.

González Acosta, J. L., Vardon, P. J., Remmerswaal, G. & Hicks, M. A. (2020). An investigation of stress inaccuracies and proposed solution in the material point method. *Computational Mechanics* **65**, No. 2, 555–581.

Jassim, I. (2013). *Formulation of a dynamic material point method (mpm) for geomechanical problems*. Ph.D. thesis, Ph. D. thesis. University of Stuttgart, Institute of Geotechnical Engineering.

Liang, Y., Zhang, X. & Liu, Y. (2019). An efficient staggered grid material point method. *Computer Methods in Applied Mechanics and Engineering* **352**, 85–109.

Lorenzo, R., da Cunha, R., Cordão Neto, M. & Nairn, J. (2017). Numerical simulation of installation of jacked piles in sand using material point method. *Canadian Geotechnical Journal* **55**, No. 1, 131–146.

Mar, A. & Hicks, M. (1996). A benchmark computational study of finite element error estimation. *International Journal for Numerical Methods in Engineering* **39**, No. 23, 3969–3983.

Naylor, D. (1974). Stresses in nearly incompressible materials by finite elements with application to the calculation of excess pore pressures. *International Journal for Numerical Methods in Engineering* **8**, No. 3, 443–460.

Phuong, N., Van Tol, A., Elkadi, A. & Rohe, A. (2016). Numerical investigation of pile installation effects in sand using material point method. *Computers and Geotechnics* **73**, 58–71.

Sadeghirad, A., Brannon, R. M. & Burghardt, J. (2011). A convected particle domain interpolation technique to extend applicability of the material point method for problems involving massive deformations. *International Journal for Numerical Methods in Engineering* **86**, No. 12, 1435–1456.

Sadeghirad, A. & Vaziri Astaneh, A. (2011). A finite element method with composite shape functions. *Engineering Computations* **28**, No. 4, 389–423.

Sołowski, W. & Sloan, S. (2015). Evaluation of material point method for use in geotechnics. *International Journal for Numerical and Analytical Methods in Geomechanics* **39**, No. 7, 685–701.

Steffen, M., Kirby, R. M. & Berzins, M. (2008a). Analysis and reduction of quadrature errors in the material point method (mpm). *International Journal for Numerical Methods in Engineering* **76**, No. 6, 922–948.

Steffen, M., Wallstedt, P., Guilkey, J., Kirby, R. & Berzins, M. (2008b). Examination and analysis of implementation choices within the material point method (mpm). *Computer Modeling in Engineering and Sciences* **32**, No. 2, 107–127.

Wang, B., Vardon, P. J. & Hicks, M. A. (2016a). Investigation of retrogressive and progressive slope failure mechanisms using the material point method. *Computers and Geotechnics* **78**, 88–98.

Wang, B., Vardon, P. J., Hicks, M. A. & Chen, Z. (2016b). Development of an implicit material point method for geotechnical applications. *Computers and Geotechnics* **71**, 159–167.

Zhang, D. Z., Ma, X. & Giguere, P. T. (2011). Material point method enhanced by modified gradient of shape function. *Journal of Computational Physics* **230**, No. 16, 6379–6398.

Zienkiewicz, O. C., Taylor, R. L. & Zhu, J. Z. (2005). *The finite element method: its basis and fundamentals*. Elsevier.

4

DEVELOPMENT OF AN IMPLICIT CONTACT TECHNIQUE FOR THE MATERIAL POINT METHOD

An implicit contact algorithm for the material point method (MPM) has been developed to simulate contact. This allows recently developed implicit MPM codes to simulate large-scale deformations and interaction with external bodies. The performance of the method has been investigated and compared to an existing explicit method using benchmark and geotechnical examples. In particular, the proposed formulation has been shown to conserve energy in a similar way to the explicit formulation and reach similar results. The method typically converges to the analytical solution when an adequate time step and mesh size is used, with the time step generally around ten times larger than the explicit method, although during the contact phase this does not always result in faster computation due to the iterative solution procedure.

Parts of this chapter appear in González Acosta *et al.* 2020

4.1. INTRODUCTION

As the fundamental attributes of MPM involve material moving substantial distances, for example in landslides with an extensive runout (e.g. Wang *et al.* 2016a), the impact of this material on other structures is a logical aspect to be investigated, which has great value in many branches of engineering. In one of the seminal MPM papers, Sulsky *et al.* (1994) showed that different bodies of material could be simulated together on the same background grid, with a single valued velocity field, and contact would be automatically calculated. However, the simulated contact was non-slip, (background) mesh dependent and, due to the lack of a specific contact formulation, inaccurate when considering bodies with different properties or initial state conditions.

The first dedicated methodology in MPM to simulate interaction between different bodies, i.e. contact, was introduced by Bardenhagen *et al.* (2000). In this method, the velocities of defined bodies are compared with a domain velocity (i.e. a multi-valued velocity field), and defines contact when these two velocities are not equal. When they are not equal, constraints on the normal and tangential kinematics are given, such that the bodies cannot penetrate each other and that the tangential behaviour can be defined based on constitutive behaviour, e.g. Coulomb friction. In this way, Bardenhagen *et al.* (2000) was able to simulate frictional slip behaviour within the MPM framework. Later, many case studies and improvements have been presented (Bardenhagen *et al.* 2001, Zhang *et al.* 2006, Li *et al.* 2009, Nairn 2013, Ma *et al.* 2014, Pantev 2016, González Acosta *et al.* 2018, Homel & Herbold 2017, Müller & Vargas 2019). Most of this work has been implemented using an explicit scheme, in fitting with the method of solving the equations of motion in these publications, and has advantages in the simplicity of implementation. However, versions of MPM which solve the equations of motion implicitly (e.g. Guilkey & Weiss 2003, Wang *et al.* 2016b) have been recently developed, which include the advantages typically associated with implicit solutions, i.e. a longer timestep. Therefore, the development of an implicit contact scheme is beneficial.

Some work regarding implicit contact in MPM has been reported where, in line with contact methods used in implicit FEM, Lagrange Multipliers (Chen *et al.* 2017) or the Penalty Method (Liu & Sun 2020) were used. Nevertheless, these techniques diverge from the methods used to compute contact in explicit MPM. In this chapter, an implicit contact algorithm is presented adapting the classical equations used in the explicit approach (Bardenhagen *et al.* 2000) to the implicit scheme and considering the Newton-Raphson iterative procedure. Moreover, to demonstrate the accuracy and performance of the solution proposed, three benchmarks and two geotechnical problems are introduced. Finally, comparative remarks are presented including also the computing performance, followed by some recommendations to increase the accuracy of the simulations.

4.2. CONTACT FORMULATION

The contact formulation relies on the equations of motion presented in the previous chapter, which are solved for a series of defined separate bodies, with the interactions (contact) between them being included in the equations of equilibrium as additional external forces. The bodies may be pre-defined (as in the examples here), or identified by the program to allow for the separation or joining of bodies. The original contact

procedures in MPM (Bardenhagen *et al.* 2000) used two steps to simulate contact: (i) the velocity field sharing step, and (ii) the contact force evaluation step. In this work, an extra (proximity detection) step to ensure mesh independency has been included, using a distance limit to activate the contact. In the velocity sharing step, the velocities are interpolated to the nodes to detect if any of the bodies may be interacting (which is possible if two or more bodies interpolate velocities to the same node). Using the individual nodal velocities of each body and the combined domain velocities (i.e. the nodal velocities accumulated from all material points in the domain), velocity sharing is detected at node i if

$$\mathbf{v}_{i,C} - \mathbf{v}_{i,bod} \neq \mathbf{0} \tag{4.1}$$

where

$$\mathbf{v}_{i,C} = \sum_{bod=1}^{nb} \frac{\bar{\mathbf{m}}_{i,bod}\mathbf{v}_{i,bod}}{\bar{\mathbf{m}}_{i,C}} \tag{4.2}$$

$$\bar{\mathbf{m}}_{i,C} = \sum_{bod=1}^{nb} \bar{\mathbf{m}}_{i,bod} \tag{4.3}$$

where $\mathbf{v}_{i,C}$ is the nodal combined velocity accounting for all bodies in the domain,$\mathbf{v}_{i,bod}$ is the nodal velocity of each independent body, $\bar{\mathbf{m}}_{i,C}$ is the combined nodal mass, bod denotes the body, nb the number of bodies and in the problem. If eq. 4.1 is true for any node i, the proximity detection rule is then evaluated. This proximity condition is

$$d\left(\mathbf{X}^{ic}_{p,bod1}, \mathbf{X}^{ic}_{p,bod2}\right) \leq d_{min} \tag{4.4}$$

where $\mathbf{X}^{ic}_{p,bod1}$ and $\mathbf{X}^{ic}_{p,bod2}$ are the coordinates of the closest material points p from each body (bod1 and bod2) to the possible contact node ic, d is the distance between $\mathbf{X}^{i}_{p,bod1}$ and $\mathbf{X}^{i}_{p,bod2}$, and $\mathbf{d}_{min}$ is the minimum distance required to active the contact. Note that $\mathbf{d}_{min}$ should have a maximum value of the cell size to ensure mesh independence, but has no minimum. Also, in eq. 4.4, only the contact between two bodies (bod1 and bod2) is considered, and the formulation to account for contact at a single node by more bodies is not included. If the velocity and proximity conditions are satisfied (i.e. eq. 4.1 and eq. 4.4), it is then necessary to evaluate if the bodies are approaching each other (contact evaluation step). This last condition is relevant because, if the bodies are separating (i.e. the first two conditions are true but the bodies are moving in opposite directions), interaction is considered not to be taking place; otherwise it would add energy into the system. This step is formulated as

$$\left(\mathbf{v}_{\mathrm{i,bod}} - \mathbf{v}_{\mathrm{i,C}}\right) \cdot \mathbf{n}_{\mathrm{i,bod}} > 0 \tag{4.5}$$

where $\mathbf{n}_{\mathrm{i,bod}}$ is the unit normal vector of the body at the contact node. The normal vector can be computed using different approaches (Nairn 2013), but in this work, the approach described in Huang *et al.* (2011) is used, which is

$$\mathbf{n}_{\mathrm{i,1}} = -\mathbf{n}_{\mathrm{i,1}} = \frac{\left(\bar{\mathbf{n}}_{\mathrm{i,1}} - \bar{\mathbf{n}}_{\mathrm{i,2}}\right)}{\left|\bar{\mathbf{n}}_{\mathrm{i,1}} - \bar{\mathbf{n}}_{\mathrm{i,2}}\right|} \tag{4.6}$$

and

$$\bar{\mathbf{n}}_{\mathrm{i,bod}} = \frac{\sum_{\mathrm{g=1}}^{\mathrm{ngp}} \nabla \mathbf{N} \mathrm{m_g}}{\left|\sum_{\mathrm{g=1}}^{\mathrm{ngp}} \nabla \mathbf{N} \mathrm{m_g}\right|} \tag{4.7}$$

where the normal $\bar{\mathbf{n}}$ is the individual normal of the body bod around node i, in which the direction is governed by the mass $\mathrm{m_g}$ concentrated at the (central) Gauss position, and ngp is the number of (central) Gauss position with concentrated mass $\mathrm{m_g}$ around node i. Note that the normal $\bar{\mathbf{n}}$ can be inconsistent (i.e. may not be perpendicular) to the surface of the body due to the irregular distribution of $\mathrm{m_g}$ around node i. This inconsistency can be lessened by using $\mathbf{n}$, the normal direction at node i in which the influence of the neighbour body is considered. Furthermore, to compute $\bar{\mathbf{n}}$, bi-linear or GIMP SF gradients can be used as the results are identical. Figure 4.1 illustrates the different variables during contact between body A and body B, and highlights the difference between $\bar{\mathbf{n}}$ and $\mathbf{n}$.

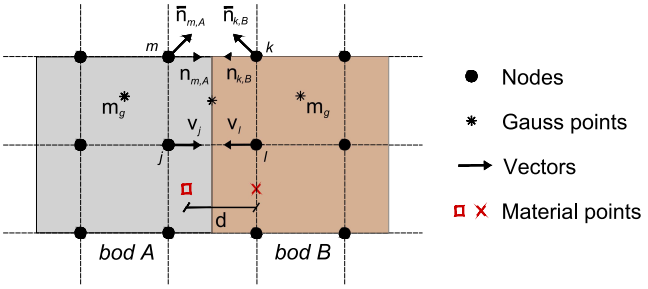

Figure 4.1: Contact variables

If eqs. 4.1, 4.4, and 4.5 are true, contact is deemed to occur, and contact conditions must be applied by assigning contact forces. To do so, first the corrected nodal velocities of each body are calculated to avoid interpenetration. Hence,

$${}^{*}\mathbf{v}_{\mathrm{ic,bod}} = \mathbf{v}_{\mathrm{ic,bod}} - \left[\left(\mathbf{v}_{\mathrm{ic,bod}} - \mathbf{v}_{\mathrm{ic,C}}\right) \cdot \mathbf{n}_{\mathrm{ic,bod}}\right] \mathbf{n}_{\mathrm{ic,bod}} \tag{4.8}$$

where ${}^{*}\mathbf{v}_{\mathrm{ic,bod}}$, is the corrected nodal velocity, and ic represents the contact node. Then, the normal contact force is computed as

$$\mathbf{F}^{\text{nc}}_{\text{ic,bod}} = \frac{\bar{\mathbf{m}}_{\text{ic,bod}} \left[\left({}^{*}\mathbf{v}_{\text{ic,bod}} - \mathbf{v}_{\text{ic,bod}} \right) \cdot \mathbf{n}_{\text{ic,bod}} \right] \mathbf{n}_{\text{ic,bod}}}{\Delta t} \tag{4.9}$$

where $\mathbf{F}^{\text{nc}}_{\text{ic,bod}}$ is the nodal normal contact force. The tangential force required to ensure non-slip (stick) conditions is calculated as

$$\mathbf{F}^{\text{stick}}_{\text{ic,bod}} = \frac{\bar{\mathbf{m}}_{\text{ic,bod}} \mathbf{n}_{\text{ic,bod}} \times \left[\left(\mathbf{v}_{\text{ic,bod}} - \mathbf{v}_{\text{ic,C}} \right) \times \mathbf{n}_{\text{ic,bod}} \right]}{\Delta t} \tag{4.10}$$

where $\mathbf{F}^{\text{stick}}_{\text{ic,bod}}$ is the frictional force required to ensure non-slip conditions. The frictional force, obeying Coulomb's theory, is then

$$\mathbf{F}^{\text{fric}}_{\text{ic,bod}} = \frac{\mathbf{F}^{\text{stick}}_{\text{ic,bod}}}{\left| \mathbf{F}^{\text{stick}}_{\text{ic,bod}} \right|} \min \left(\mu \left| \mathbf{F}^{\text{nc}}_{\text{ic,bod}} \right|, \left| \mathbf{F}^{\text{stick}}_{\text{ic,bod}} \right| \right) \tag{4.11}$$

where $\mathbf{F}^{\text{fric}}_{\text{ic,bod}}$ is the final frictional force between bodies, μ is the friction coefficient which depends on the material characteristics, the quotient ensures that the direction of the force opposes the relative motion, and the min function determines the magnitude of the force. Finally, if contact occurs, nodal accelerations are no longer computed using eq. 2.14, since the contact loads should be included as

$$\ddot{\mathbf{a}}^{\text{t}}_{\text{bod}} = \frac{\mathbf{F}^{\text{ext,t}}_{\text{bod}} - \mathbf{F}^{\text{int,t}}_{\text{bod}} + \mathbf{F}^{\text{nd,t}}_{\text{bod}} - \mathbf{F}^{\text{fric,t}}_{\text{bod}}}{\mathbf{m}^{\text{t}}_{\text{bod}}} \tag{4.12}$$

4.3. EXPLICIT AND IMPLICIT CONTACT ALGORITHM

4.3.1. EXPLICIT CONTACT ALGORITHM

The implementation of contact using the explicit scheme is straightforward. Table 4.1 shows the algorithm of the explicit scheme including the contact steps. Several minor steps are omitted, such as the activation of the boundary conditions and the computation of the material point local coordinates, in order to maintain the algorithm simplicity. The square brackets located at the left side of the figure indicate a loop for each body; i.e. the combination of steps should be repeated for each body before continuing with the following steps. The plastic iteration loop is indicated, but the procedures are not elaborated; the reader is directed to Smith *et al.* (2013) and Sloan *et al.* (2001) where the plastic procedures are described in detail. Note that, similar to the block benchmark presented in Section 2.7, the contact at the boundaries occurs due to the fixed boundary, which prevents the displacement of the block, causing the development of strain energy which pushes the block upwards.

Table 4.1: Steps followed in the explicit MPM scheme considering contact

Evaluate nodal force and mass (eqs. 2.10 or 3.13, 2.11 or 3.14, and 2.12): $\mathbf{F}^{ext,t}_{i,bod}$, $\mathbf{F}^{int,t}_{i,bod}$, and $\bar{\mathbf{m}}^{t}_{i,bod}$
Evaluate combined velocity (eq. 4.2): $\mathbf{v}^{t}_{i,C}$
Estimate new contact velocities (eq. 4.8): ${}^{*}\mathbf{v}^{t}_{ic,bod}$
Estimate contact and frictional forces (eqs. 4.9 and 4.11): $\mathbf{F}^{nc}_{ic,bod}$ and $\mathbf{F}^{fric}_{ic,bod}$
Estimate nodal accelerations (eqs. 2.14 or 4.12): $\bar{\mathbf{a}}^{t}_{i,bod}$
Update material point velocity at time $t+\Delta t$ (eq. 2.15): $\mathbf{v}_p^{t+\Delta t}$
Update nodal velocities (eq. 2.18): $\bar{\mathbf{v}}^{t+\Delta t}$
Estimate material point trial stresses (eq. 2.17 or 3.16): $\boldsymbol{\sigma}_p^{trial}$
Loop 1: if $Y(\boldsymbol{\sigma}_p^{trial}) > 0$: return stresses to the yield surface Y
Plastic iteration loop
IF $Y(\boldsymbol{\sigma}_p^{trial(t+\Delta t)}) = 0$: EXIT Loop 1
END Loop 1
Update material point stresses after plasticity $\boldsymbol{\sigma}_p^{t+\Delta t} = \boldsymbol{\sigma}_p^{trial(t+\Delta t)}$
Update material point positions (eq. 2.16): $\mathbf{x}_p^{t+\Delta t}$

4.3.2. IMPLICIT CONTACT ALGORITHM

To simulate contact using the implicit scheme, the same approach as in the explicit scheme is used. Newmark's time integration technique and the Newton-Raphson method are used, so the equations used to estimate contact must be updated in each iteration step. Moreover, if contact occurs, it is assumed that it persists throughout the Newton-Raphson iterative process, i.e. between times t and $t+\Delta t$. Considering these assumptions, the equations used to update nodal velocities during the iterative procedure are then

$$ {}^{k}\mathbf{v}^{t+\Delta t}_{ic,C} = \sum_{bod=1}^{nb} \frac{\bar{\mathbf{m}}_{ic,bod}\mathbf{v}^{t+\Delta t}_{ic,bod}}{\bar{\mathbf{m}}_{ic,C}} \tag{4.13} $$

and

$$ {}^{k*}\mathbf{v}^{t+\Delta t}_{ic,bod} = \mathbf{v}^{t+\Delta t}_{ic,bod} - \left[\left(\mathbf{v}^{t+\Delta t}_{ic,bod} - \mathbf{v}^{t+\Delta t}_{ic,C}\right)\cdot\mathbf{n}_{ic,bod}\right]\mathbf{n}_{ic,bod} \tag{4.14} $$

the contact loads are computed as

$$ {}^{k}\mathbf{F}^{nc,t+\Delta t}_{ic,bod} = \frac{\bar{\mathbf{m}}_{ic,bod}\left[\left({}^{*}\mathbf{v}^{t+\Delta t}_{ic,bod} - \mathbf{v}^{t+\Delta t}_{ic,bod}\right)\cdot\mathbf{n}_{ic,bod}\right]\mathbf{n}_{ic,bod}}{\Delta t} \tag{4.15} $$

with the tangential force to ensure sticking conditions calculated as

$$ {}^{k}\mathbf{F}^{stick,t+\Delta t}_{ic,bod} = -\frac{\bar{\mathbf{m}}_{ic,bod}\mathbf{n}_{ic,bod}\times\left[\left(\mathbf{v}^{t+\Delta t}_{ic,bod} - \mathbf{v}^{t+\Delta t}_{ic,C}\right)\times\mathbf{n}_{ic,bod}\right]}{\Delta t} \tag{4.16} $$

and the frictional force

$$ {}^{k}\mathbf{F}^{\text{fric},t+\Delta t}_{\text{ic,bod}} = \frac{\mathbf{F}^{\text{stick}t+\Delta t}_{\text{ic,bod}}}{\left|\mathbf{F}^{\text{stick},t+\Delta t}_{\text{ic,bod}}\right|} \min\left(\mu\left|\mathbf{F}^{\text{nc},t+\Delta t}_{\text{ic,bod}}\right|, \left|\mathbf{F}^{\text{stick},t+\Delta t}_{\text{ic,bod}}\right|\right) \tag{4.17} $$

Note that these equations are similar to those used in the explicit scheme, with the exception that the nodal combined velocities $\mathbf{v}^{t+\Delta t}_{\text{ic,bod}}$ are updated every iteration, which leads to a new set of corrected velocities and nodal forces. Finally, if contact occurs, the incremental displacements should be computed using

$$ \bar{\mathbf{K}}_{\text{bod}}\, {}^{k}\bar{\mathbf{u}}_{\text{i,bod}} = {}^{k-1}\left(\mathbf{F}^{\text{ext}}_{\text{i,bod}} - \mathbf{F}^{\text{kin}}_{\text{i,bod}} - \mathbf{F}^{\text{int}}_{\text{i,bod}} + \mathbf{F}^{\text{nc}}_{\text{ic,bod}} - \mathbf{F}^{\text{fric}}_{\text{ic,bod}}\right)^{t+\Delta t} \tag{4.18} $$

Table 4.2: Steps followed in the implicit MPM scheme considering contact

- Evaluate nodal mass, velocities and accelerations (eqs. 2.12, 2.13 and 2.34):
  $\bar{\mathbf{m}}^{t}_{\text{i,bod}}$, $\bar{\mathbf{v}}^{t}_{\text{i,bod}}$ and $\bar{\mathbf{a}}^{t}_{\text{i,bod}}$
- Evaluate nodal external loads and stiffness (eqs. 2.10 or 3.13 and 2.31 or 3.15):
  $\mathbf{F}^{\text{ext},t}_{\text{i,bod}}$ and $\bar{\mathbf{K}}^{t}_{\text{bod}}$
- Evaluate combined velocity (eq. 4.2): $\mathbf{v}^{t}_{\text{i,C}}$
- Initialize $\bar{\mathbf{u}}^{t+\Delta t}_{\text{ic,bod}} = 0$, $\mathbf{v}^{t+\Delta t}_{\text{ic,bod}} = \bar{\mathbf{v}}^{t}_{\text{i}}$, $\mathbf{F}^{\text{nc},t+\Delta t}_{\text{ic,bod}} = 0$ and $\mathbf{F}^{\text{fric},t+\Delta t}_{\text{ic,bod}} = 0$
- Loop 1: over the number of iteration steps
  - Evaluate nodal internal loads (eq. 2.11 or 3.14): $\mathbf{F}^{\text{int},t}_{\text{i,bod}}$
  - Evaluate nodal kinetic loads (eq. 2.11 or 3.14): $\mathbf{F}^{\text{kin},t}_{\text{i,bod}}$
  - Estimate contact and frictional forces (eqs. 4.9 and 4.11): $\mathbf{F}^{\text{nc}}_{\text{ic,bod}}$ and $\mathbf{F}^{\text{fric}}_{\text{ic,bod}}$
  - Estimate incremental displacements (2.30 or 4.18):$\bar{\mathbf{u}}^{t+\Delta t}_{\text{i,bod}}$
  - Update nodal velocities (eq. 2.28):$\bar{\mathbf{v}}^{t+\Delta t}_{\text{i,bod}}$
  - Evaluate combined velocity (eq. 4.13): $\mathbf{v}^{t}_{\text{i,C}}$
  - Estimate new contact velocities (eq. 4.14): ${}^{*}\mathbf{v}^{t+\Delta t}_{\text{ic,bod}}$
  - Estimate material point trial stresses (eq. 2.38 or 3.17): $\boldsymbol{\sigma}^{\text{trial}}_{\text{p}}$
  - Loop 2: if $Y(\boldsymbol{\sigma}^{\text{trial}}_{\text{p}}) > 0$: return stresses to the yield surface Y
    - Plastic iteration loop
    - IF $Y(\boldsymbol{\sigma}^{\text{trial}(t+\Delta t)}_{\text{p}}) = 0$: EXIT Loop 1
  - END Loop 2
  - IF convergence is true (eq. 2.33) or the maximum number of iterations is reached: exit Loop 1
- Update material point stresses after plasticity $\boldsymbol{\sigma}^{t+\Delta t}_{\text{p}} = \boldsymbol{\sigma}^{\text{trial}(t+\Delta t)}_{\text{p}}$
- Update material point variables (eqs. 2.35, 2.36 and 2.37): $\mathbf{a}^{t+\Delta t}_{\text{p}}$, $\mathbf{v}^{t+\Delta t}_{\text{p}}$ and $\mathbf{x}^{t+\Delta t}_{\text{p}}$

Table 4.2 shows the steps followed to simulate contact using the implicit scheme. It should be noted that the vector of external forces $\mathbf{F}^{ext}$ and the stiffness matrix $\bar{\mathbf{K}}$ are evaluated at time $t + \Delta t$ outside the iteration loop, as both remain constant throughout the iterative procedure. The modified Newton-Raphson is used, in which the stiffness matrix is kept constant during the iterative procedure. The small time steps used to capture the kinematics ensure that this results in a reasonable solution.

4.4. APPLICATION AND EVALUATION OF CONTACT METHODS

4.4.1. BENCHMARK PROBLEMS

To evaluate the performance of the implicit contact method, three plane strain benchmarks are analysed and compared against the explicit solution, as well as against the analytical, and FEM solutions where available. The first two benchmarks (i.e. a collision and a 1D vibrating bar) are used to study energy conservation. The first benchmark considers a contact occurring instantaneously between two blocks, and the second considers contact which persists throughout the whole simulation. The third benchmark is the simulation of a block sliding on a rigid surface, and is used to analyse the interaction between bodies when considering frictional forces. Each benchmark was simulated using DM-GC and four equally spaced material points per background element, which were initially positioned at the local coordinates $\xi = \pm 0.5$ and $\eta = \pm 0.5$ (see Appendix A)

COLLISION BENCHMARK

In Figure 4.2, the initial configuration of the collision benchmark is shown. The benchmark consists of two square blocks (A and B) of size 0.6 m, moving freely towards each other through a background mesh with a mesh spacing of $\Delta_x = \Delta_y = 0.20$ m. Each block has an initial horizontal velocity of 0.5 m/s. The properties of both blocks are Young's modulus, E = 500 kPa, Poisson's ratio, $\upsilon = 0.45$, and unit weight, $\gamma = 20$ kN/m^3. The tolerance values used in the Newton-Raphson iterative procedure, and to establish contact, are tol = 1.0×10^{-8} (eq. 2.33) and $d_{min} = 0.2$ m, respectively. Gravity forces have not been considered.

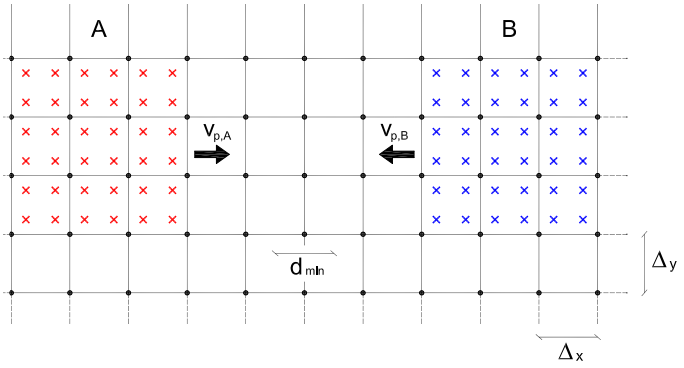

Figure 4.2: Collision benchmark

Figure 4.3, shows the results of the collision in terms of total energy (TE), for both the explicit and the implicit schemes. In Figure 4.3a, for the explicit scheme, it is observed that, at the moment of the collision (t_c), the energy decreases significantly (by 17%) and, depending on the time step used, the total energy either continues decreasing or stays almost constant after the collision. Figure 4.3b shows that, using the implicit scheme, the total energy behaves in a similar way to the explicit solution, except that some oscillation of the energy is observed after the collision. This oscillations are attributed to not capturing accurately internal waves due to the large time step used, which is 10 times greater than that used with the explicit scheme, for almost the same performance.

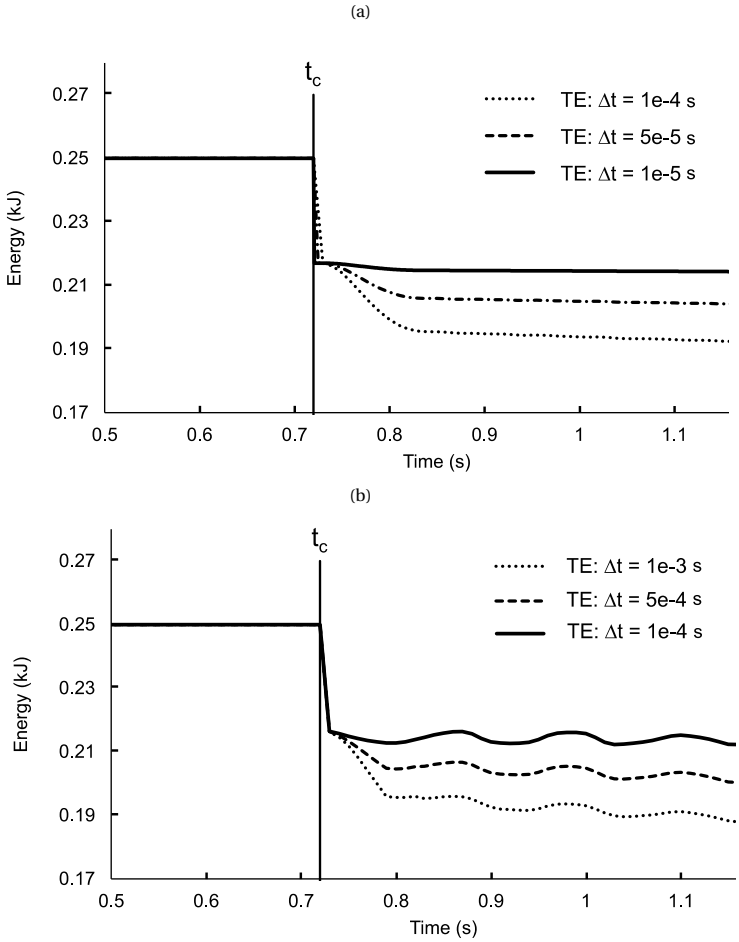

Figure 4.3: Energy conservation after collision using a) the explicit scheme, and b) the implicit scheme

Additionally, Figure 4.4 and Table 4.3 demonstrates the energy conservation and computational time required to complete each simulation with respect to the mesh (element) size for the implicit scheme. The study of energy conservation is performed

using a time step of $\Delta t = 1.0 \times 10^{-4}$ s, and mesh sizes of 0.20, 0.10 and 0.05 m. Also, an additional curve (solid line with markers) computed using a mesh size of 0.05 m and a time step of $\Delta t = 1.0 \times 10^{-5}$ s is added to Figure 6 to study the effects of reducing the time step and the mesh size simultaneously. The contact tolerance values used are the maximum values for the mesh, i.e. dmin = 0.20, 0.10 and 0.05, respectively. It is observed that the drop of energy at the point of contact decrease with the reduction of the mesh size, improving the conservation of energy. Furthermore, by reducing the mesh size and time step together, the drop of energy and the oscillations after contact reduces drastically, reinforcing the theory that the oscillations in 4.3b were caused due to the large time step used. Nonetheless, despite of the improvement of the results, some reduction in energy is still observed. The analysis of the computational time is performed considering the time steps, $\Delta t = 1.0 \times 10^{-5}$ s, and, $\Delta t = 1.0 \times 10^{-4}$ s, for the explicit and the implicit scheme, respectively. It is observed that the computational time needed to complete a simulation grows substantially with the reduction of the mesh size. Nevertheless, the time relation is almost constant, being that the implicit solution is on average 30% faster than the explicit solution. Finally, the Courant number (CN) indicates that the conditions of each simulation (i.e. material properties, mesh size and time steps) are adequate (i.e. CN < 1).

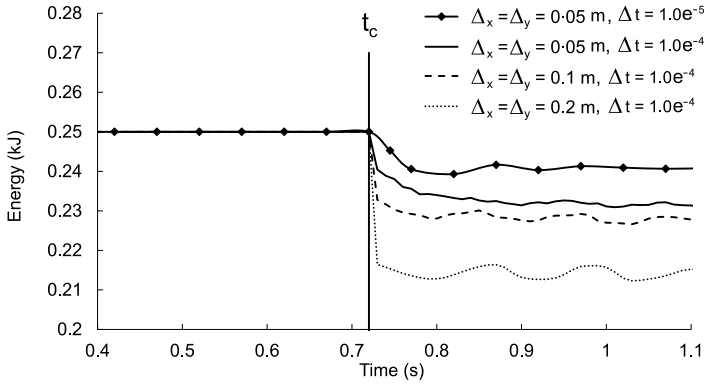

Figure 4.4: Energy conservation with implicit scheme using different mesh sizes

Table 4.3: Collision benchmark computational time

Mesh size (m)	Computational time		Δt implicit / Δt implicit	Courant number
	Implicit	Explicit		
0.2	2	3	0.67	0.01
0.1	5	7	0.71	0.03
0.05	21	31	0.68	0.06
0.02	224	330	0.68	0.15

The reason for the decrease of energy observed in Figure 4.3 and 4.4 is the inconsistency between the contact loads and the internal loads developed at the contact

($\mathbf{F}^{nc} \neq \mathbf{F}^{int}$). One method to prevent this inconsistency between the contact and internal forces is to compute the contact loads as a function of the internal loads developed by each body at the contact (Xiao-Fei *et al.* 2008). At the contact interface, the normal acceleration of each body can be assumed to be equal (i.e. $\mathbf{a}^{t}_{i,A} \cdot \mathbf{n}_i i, A = -\mathbf{a}^{t}_{i,B} \cdot \mathbf{n}_i i, B$). Hence, from Newton's second law, it is established that

$$m_{i,A}\left(\mathbf{a}_{i,A} \cdot \mathbf{n}_{i,AB}\right) = \mathbf{F}^{int}_{i,A} \cdot \mathbf{n}_{i,A} - \mathbf{F}^{nc}_{i} \tag{4.19}$$

$$m_{i,B}\left(\mathbf{a}_{i,B} \cdot \mathbf{n}_{i,AB}\right) = \mathbf{F}^{int}_{i,B} \cdot \mathbf{n}_{i,B} + \mathbf{F}^{nc}_{i} \tag{4.20}$$

which leads to

$$\mathbf{F}^{nc}_{i,A} = \frac{\left(m_{i,B}\,\mathbf{F}^{int}_{i,A} - m_{i,A}\,\mathbf{F}^{int}_{i,B}\right) \cdot \mathbf{n}_{i,AB}}{\left(m_{i,A} + m_{i,B}\right)} = -\mathbf{F}^{nc}_{i,B} \tag{4.21}$$

where $\mathbf{F}^{nc}_{i,A}$ and $\mathbf{F}^{nc}_{i,B}$ are the contact forces between the bodies as a function of the internal forces developed. In Figure 4.5, the energy conservation of the collision benchmark is plotted using eq. 4.21 to compute the contact loads, a step size of $\Delta t = 1.0 \times 10^{-5}$ s, a mesh of size of $\Delta x = \Delta y = 0.20$ m, and the explicit scheme. It is seen that the energy conservation improves considerably because the contact loads and the internal loads are equivalent. However, this approach should be implemented with caution since the contact forces are dependent on the material point stresses which are known to suffer from numerical oscillations, leading to a oscillations of the contact loads. Since stress oscillation problems are typical in MPM, in order to implement eq. 4.21 in any problem more complicated than this example, further improvements are needed. Additionally, the implementation of this contact technique using the implicit scheme is not straightforward due to the interdependence of the internal and contact loads and the iterative nature of the implicit scheme. Since these improvements needed to implement this technique in both solutions schemes are beyond the scope of this thesis, all remaining examples have been computed using the initial approach.

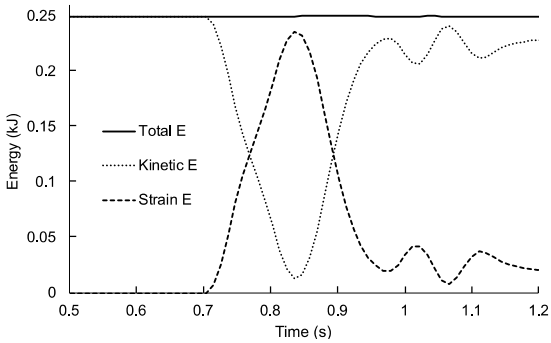

Figure 4.5: Energy conservation during block collision with explicit scheme

1D BAR BENCHMARK

This benchmark is similar to other 1D vibration benchmarks, except that this 1D bar is made up of two bars (bodies A and B), where interaction occurs due to the contact

forces at the interface between the two bodies. Initially, the bodies have zero internal stresses, but, due to the gravity force, they compress as soon as they are allowed to move. The equations of motion are calculated separately for the two bodies and the interaction between them is calculated via the contact forces. Figure 4.6 shows a sketch of the benchmark, including the dimensions of the bars and the boundary conditions. Each bar has a height of $H_1 = H_2 = 5$ m and a width of L = 1 m. The size of the mesh is, $\Delta x = \Delta y = 0.25$ m. The properties of both bars are Young's modulus, E = 1000 kPa, Poisson's ratio, $\upsilon = 0.35$, and unit weight, $\gamma = 15 kN/m^3$. The tolerance values used in the Newton-Raphson iterative procedure and the contact distance are tol = 1.0×10^{-8} and $d_{min} = 0.25$ m, respectively.

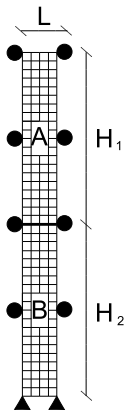

Figure 4.6: 1D bar benchmark background mesh, where each element was initially filled with 4 material points

Figures 4.7 and 4.8 shows the sum of the total energy of each 1D bar and the displacement of the top material point throughout 3 seconds of simulation using several time steps for both solution schemes, respectively. Furthermore, FEM results are included, which are considered as a reference solution. As can be observed in Figure 4.7a, by reducing the time step, the energy conservation is improved. The largest drop of energy is during compression, when most of the penetration occurs. Using the smallest time step of $\Delta t = 1.0^{-5}$ s, the loss of energy is the lowest (4.7 % after 3 seconds). On the other hand, using the largest time step, $\Delta t = 1.0^{-4}$, the loss of energy is considerable (22.5 % after 3 seconds). Consistent with the calculated loss of energy, Figure 4.7b shows that the top material point is unable to reach its original position when a large time step used. In contrast, when the smallest time step is used, results are nearly equal to FEM results (i.e. accurate). This is because the computed contact loads can adjust satisfactorily to the change of internal forces and velocities of each body during contact when smaller time step are used, restricting the penetration of the bodies. When the implicit scheme is used (Figure 4.8), the results for energy conservation and material point position are similar to those using the explicit scheme, based on each implicit simulation using a time step 10 times larger than in the explicit simulation.

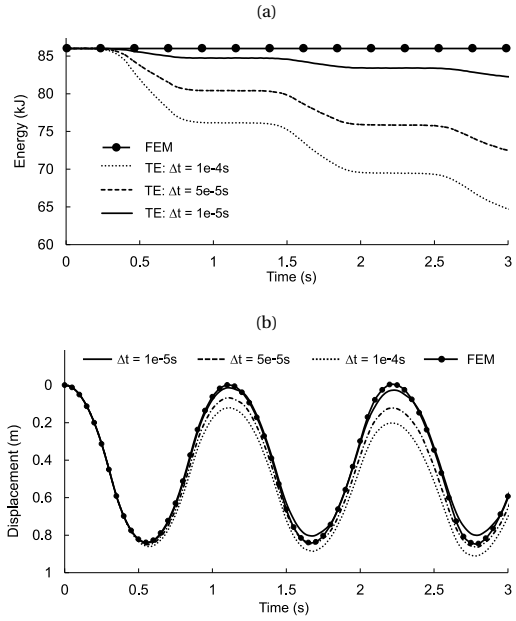

Figure 4.7: a) Sum of the Total energy of each 1D bar using the explicit scheme, and b) displacement of the top material point

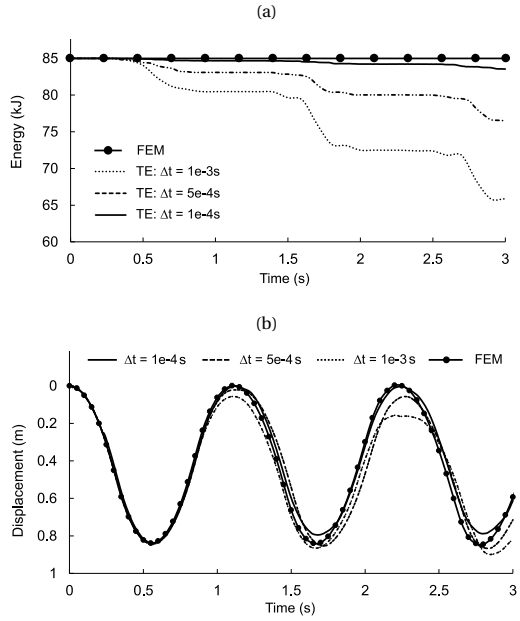

Figure 4.8: a) Sum of total energy of each 1D bar using the implicit scheme, and b) displacement of the top material point

SLIDING BENCHMARK

In this benchmark, a block under gravity loading is located on a flat surface and slides. Figure 4.9 shows a sketch of the problem. Body A is a rigid surface and a body B slides over body A due to the gravity load (g) which is rotated by $\theta = 15^o$ to the vertical. The lengths of the two bodies are $L_1 = 1.5$ m and $L_2 = 6$ m, respectively, and the height of each body is, $H_1 = H_2 = 0.75$ m. The mesh size is $\Delta x = \Delta y = 0.25$ m, and body A is fixed at the bottom boundary and at the vertical boundaries. The elastic properties of the bodies are Young's modulus, $E_A = 5000$ kPa and $E_B = 1000$ kPa, in which E_A and E_B refer to body A and B, respectively. The Poisson's ratio and unit weight for both bodies is, $\nu = 0.35$ and $\gamma = 20\text{kN/m}^3$, respectively. Two simulations using two different friction factors, $\mu = 0$ and $\mu = 0.15$, have been performed, and the results are compared with the analytical solution of (Jiang & Yeung 2004). Time steps of $\Delta t = 5.0 \times 10^{-5}$ s and $\Delta t = 5.0 \times 10^{-4}$ s were used for the explicit and the implicit simulations, respectively. The tolerance values used in the Newton-Raphson iterative procedure and the contact distance are tol = 1.0^{-8} and $d_{min} = 0.25$, respectively.

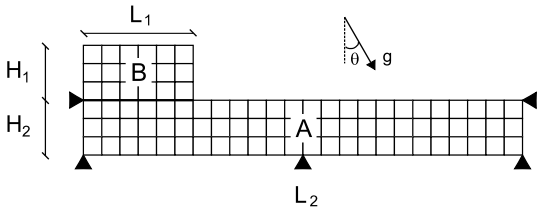

Figure 4.9: schematic of the sliding benchmark

Figure 4.10 shows the results of the benchmark over two seconds of sliding. It is seen that the simulated results using the explicit and the implicit schemes are similar to the analytical solution, indicating that the friction between the bodies is accurate. Figure 4.11 shows the contact loads distribution at the interface of body A and B considering $\mu = 0.15$. The load distribution of Figure 4.11a corresponds to the initial state of the simulation, in which the block has not moved. In this case, the normal load $\mathbf{F}^{nc}$ is constant at the centre of the block and drops close to the corners. Also, the frictional load $\mathbf{F}^{fric}$ is maximum at 1m and minimum at 0.25 m, indicating that the frictional force is developing from right to left due to the weight of body B and the inclined gravity force. Then, Figure 4.11b shows the instant in which body B begins to slide. In this case, the frictional loads are constant below body B, indicating that the frictional force is fully developed. Additionally, the results obtained using the explicit and the implicit schemes are similar. The reader is directed to the work of Oden & Pires (1984) in which a similar simulation is performed. Note that, due to the differences in the simulation conditions, results are not the same. Nevertheless, similarities can be observed, as the distribution of the normal and frictional load before the movement of the block.

Figures 4.12, 4.13 show the average of the normal and tangent loads below body B during the sliding considering also $\mu = 0.15$. It is observed that both loads are close and oscillate around the analytical solution (which is computed considering static conditions). These oscillations are caused mainly by the bouncing and vibrations of body B during

the sliding. This is more evident in the explicit results which contain larger magnitude of oscillations

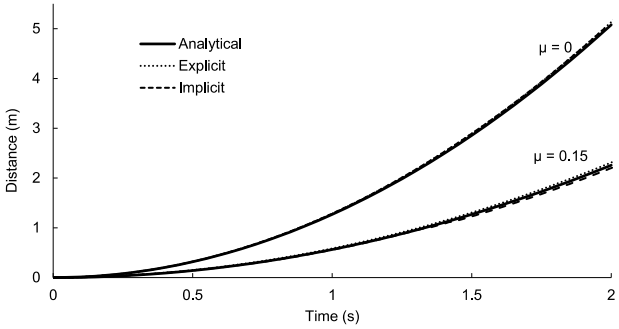

Figure 4.10: Sliding simulation using the explicit and the implicit scheme

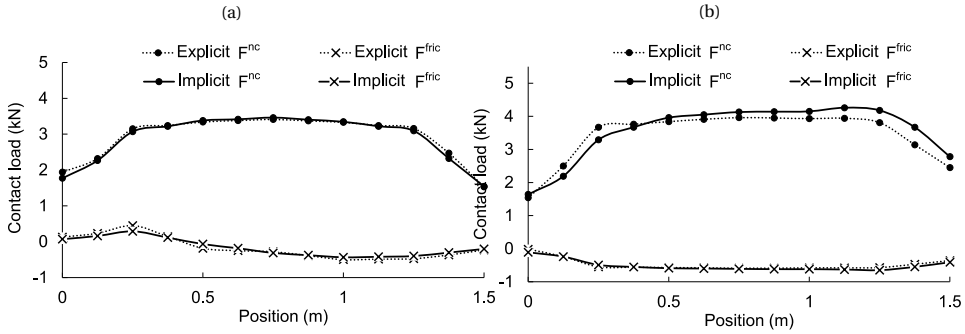

Figure 4.11: Normal $\mathbf{F}^{nc}$ and tangent $\mathbf{F}^{fric}$ contact loads below body B a) before displacement and b) after displacement

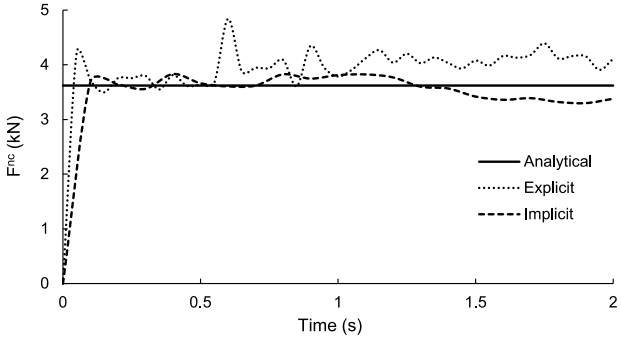

Figure 4.12: Interface normal force (F^{nc})

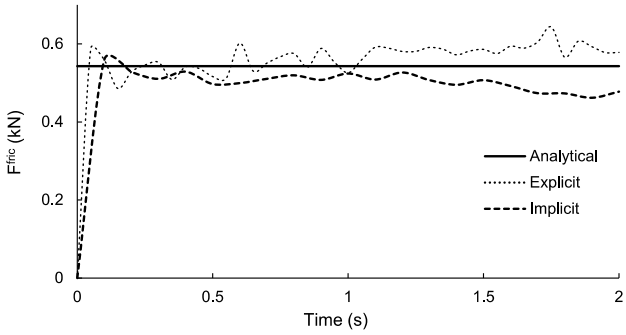

Figure 4.13: Interface tangent force (F^{fric})

4.4.2. GEOTECHNICAL APPLICATIONS

Two plane strain geotechnical problems are simulated using both the explicit and the implicit contact solutions. The first problem consists of a shallow foundation that penetrates into the soil due to an increase in gravitational loading applied to the foundation. The second problem consists of a vertical cutting that, after failing, slides and collides against a wall. In these problems, the Young's modulus used for the rigid elements (i.e. the foundation and the wall) are lower than the actual values for such elements. The intention of this is to permit the bending of the rigid bodies rather to keep them undeformable, to demonstrate the capabilities of the method.

FOUNDATION

This problem involves a foundation slab that penetrates into an incompressible, linear elastic, perfectly plastic von Mises soil, with a rough interface, i.e. no tangential slip is allowed. The initial stresses in the soil are computed as $\sigma_y = \gamma_{soil} h_y$ and $\sigma_x = \sigma_Z = K_0 \sigma_y$ where $\gamma_{soil} = 17.5 kN/m^3$ is the soil unit weight, h_y is the depth of the material point below the soil surface, and $K_0 = 0.7$ is the coefficient of earth pressure at rest. The elastic parameters of the soil are Young's modulus, $E_{soil} = 5.0 \times 10^3 kPa$, and Poisson's ratio, $\nu_{soil} = 0.49$, and its undrained shear strength is $S_u = 10$ kPa. The slab Young's modulus and Poisson's ratio are $E_{slab} = 1.0 \times 10^4 kPa$ and $\nu_{slab} = 0.45$, respectively.

Figure 4.14 shows the geometry and boundary conditions of the problem. The slab dimensions are thickness, $H_1 = 0.6$ m, and width, $2L_1 = 4.0$ m, (only half of the foundation has been modelled), while the modelled soil domain has a depth of $H_2 = 4.0$ m and a width of $L_2 = 7.0$ m, respectively. The vertical boundaries of the domain are fixed in the horizontal direction, whereas the bottom boundary is fixed in both directions. The mesh comprises four noded square elements of size $\Delta_x = \Delta_y = 0.20$ m, and there are initially four MPs in each element. Based on the results of the benchmark analyses, the time steps selected for the explicit and implicit simulations were, $\Delta t_{expl} = 1.0 \times 10^{-5}$ and $\Delta t_{impl} = 1.0 \times 10^{-4}$ s, respectively.

The pressure exerted by the slab on the soil has been applied by increasing the self-weight of the slab by gravitational loading; i.e. by assuming the density of the slab to be $\rho_{slab} = 3000 kg/m^3$ and increasing the gravity from zero at a rate of 1 g/s while keeping the gravity of the soil constant at 1g. Finally, the tolerance value used in the Newton-Raphson iterative procedure and the contact distance are tol = 1.0×10^{-8} and $d_{min} = 0.20$ m, respectively.

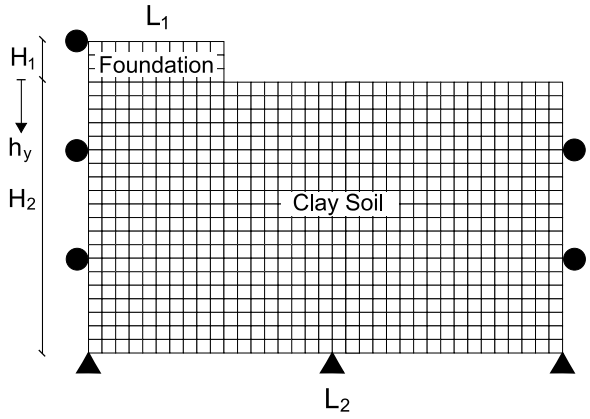

Figure 4.14: Foundation problem

Figure 4.15 shows the results for the foundation problem after a settlement of 0.20 m using the implicit scheme (with similar results being obtained with the explicit scheme). In Figure 4.15a, the plastic deviatoric strain contours indicate a failure mechanism resembling the failure described in Terzaghi (1943), while Figure 4.15b, shows the shear stresses developed. By comparing both parts of the figures, it is seen that the larger plastic deviatoric strains develop in zones where the shear stresses shift from positive values to negative. It is also evident that, due to the soil yielding and the use of a large Poisson's ratio, some checker-board oscillation occurs, as is typical for von Mises incompressible materials using bi-linear elements. The reader is referred to Coombs *et al.* 2018 and González Acosta *et al.* 2019, where the volumetric locking problem has been studied.

Figure 4.16, shows the pressure(P_L)-displacement responses computed using the explicit and implicit schemes plotted against two analytical solutions of Terzaghi (1943). Both of these solutions for the bearing capacity consider rough contact between the soil and foundation. However, one solution does not include any overburden load ($Q_1 = S_u N_c$), whereas the second solution does ($Q_2 = S_u N_c + \gamma_{soil} D_f$, where D_f is the depth of the base of the foundation). The pressure load between the slab and the soil is computed from the contact forces (F^{nc}) and the size of the foundation. As can be seen, despite the stress oscillations observed in Figure 4.15a, the maximum simulated bearing capacity of the soil is close to both analytical solutions, especially the second solution in which the influence of the deformation has been included (via the overburden component).

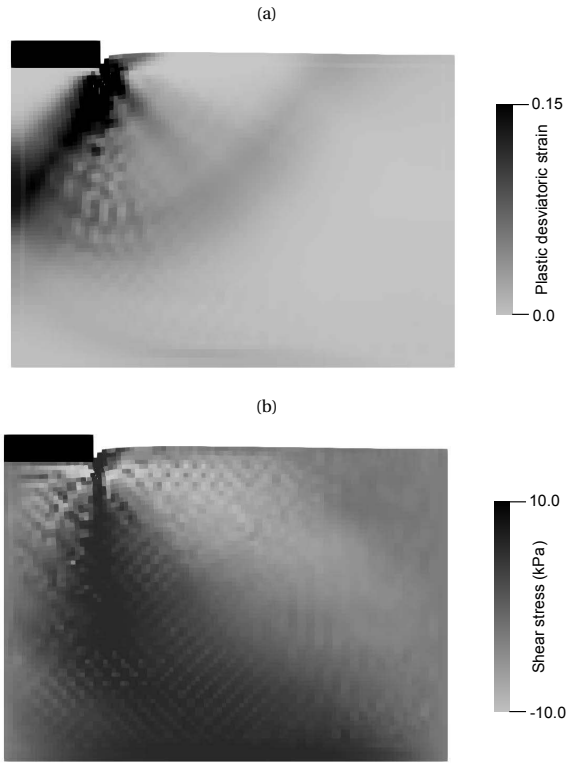

Figure 4.15: a) Plastic deviatoric strain after failure and, b) shear stresses after failure

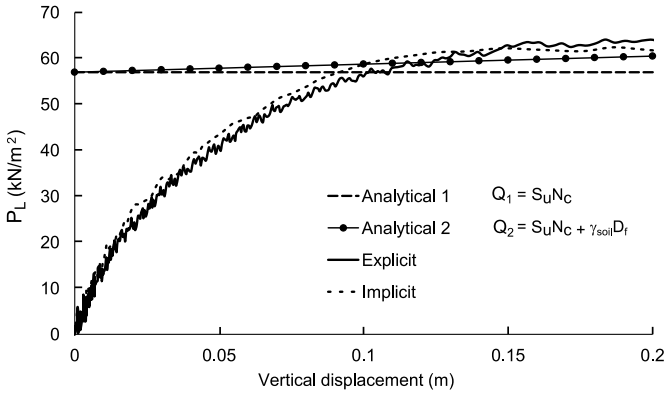

Figure 4.16: Pressure-displacement curves up to a settlement of 0.2 m using both explicit and implicit schemes

VERTICAL CUTTING

This problem consists of a vertical cutting that fails due to self-weight and then hits a protection wall. Figure 4.17 shows a schematic of the initial state of the problem, including the boundary conditions. As for the previous example, the initial stress states in the vertical cutting and the protection wall are computed using the depth of each material point from the surface of each structure (i.e. h_{y1} and h_{y2}, respectively); and the unit weights and earth pressure coefficients of the soil and the wall, $\gamma_{soil} = 18.0\,kN/m^3$, $k_{0-soil} = 0.7$ and $\gamma_{wall} = 25.0kN/m^3$, $k_{0-wall} = 0.5$, respectively. To generate the initial stresses in the vertical cut, a static step is applied in which the movement of the material points is prevented. This step causes large localised shear stresses to develop at the toe of the vertical cut, which cause the triggering of the landslide when the material points are released. The boundary conditions, are that both bodies are fully fixed at the base, and the soil is also fixed in the horizontal direction at the left-hand vertical boundary. The height and width of the modelled soil domain and the protection wall are $H_1 = 2.5$ m and $L_1 = 6.0$ m, and $H_2 = 1.0$ m and $L_2 = 0.8$ m, respectively. The distance between the soil and the wall is $L_3 = 1.0$ m, and the element size is $\Delta_x = \Delta_y = 0.10$ m.

The elastic parameters of the soil and the wall are Young's moduli $E_{soil} = 1.0 \times 10^3$ kPa and $E_{wall} = 3.0 \times 10^3$ kPa, and Poisson's ratios $\mu_{soil} = 0.38$ and $\mu_{wall} = 0.30$, respectively. The soil is modelled as a linear elastic, linear strain-softening Von Mises material, with a peak cohesion $c_p = 14$ kPa, a residual cohesion, $c_r = 5$ kPa, and a softening modulus, $H_s = -18$ kPa (see Wang *et al.* 2016b for details of the constitutive model). The wall is simulated as a linear elastic material. The time steps selected for the explicit and the implicit simulations are, $\Delta t_{expl} = 5.0 \times 10^{-5}$ and $\Delta t_{impl} = 5.0 \times 10^{-4}$ s, respectively. The tolerance value used in the Newton-Raphson iterative procedure and the contact distance are tol = 1.0×10^{-8} and $d_{min} = 0.1$ m, respectively.

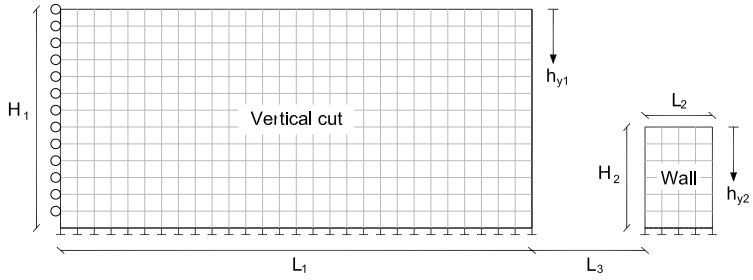

Figure 4.17: Vertical cut and protection wall (mesh indicative and not scaled)

Figure 4.18 shows the distribution of plastic deviatoric strains in the vertical cut, and the distribution of deviatoric stresses in the wall, after a) 0.8, b) 1.25 and c) 2.4 seconds in the implicit simulation. Figure 4.18a shows a moment after the vertical cut has failed, with the soil mass moving downwards and to the right, and increasing its kinetic energy before the collision. Figure 4.18b shows the instant at which the contact load and the internal deviatoric stresses in the wall are a maximum. Figure 4.18c shows the end of the simulation, when the wall has partially recovered its position. It can be seen that, due to the adopted proximity detection rule, the two bodies are closely connected during

contact.

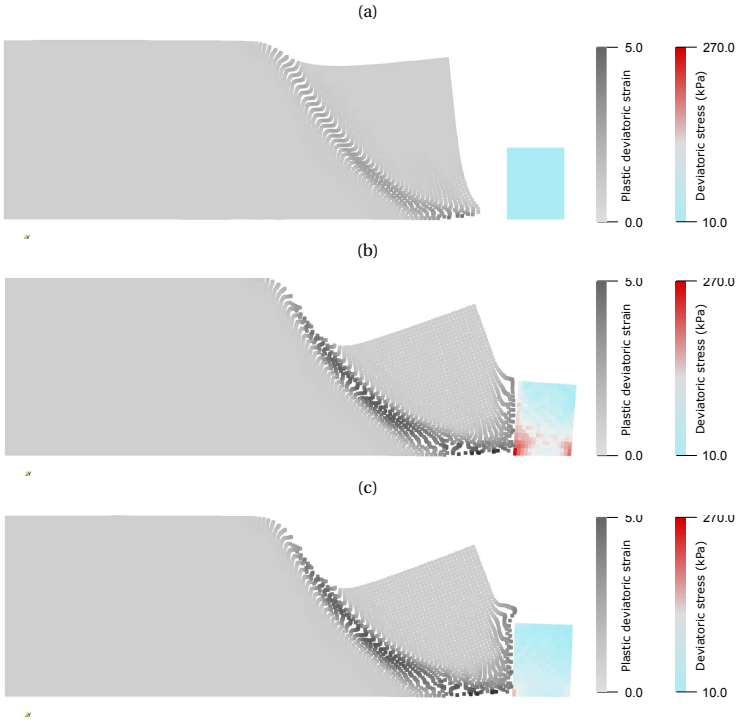

Figure 4.18: Collision simulation after a) 0.8, b) 1.25, and c) 2.4 seconds. Plastic deviatoric strains are shown in the soil, and deviatoric stresses are shown in the wall

Figure 4.19 shows the average pressure at the wall surface and the deviatoric stress at the wall base. The pressure in Figure 4.19a has been computed by adding the contact force from each contact node and dividing it by the wall height H_2. The deviatoric stress (q) in Figure 4.19b has been computed, using the principal stresses, as

$$q = \frac{\sqrt{(\sigma_1 - \sigma_2)^2 + (\sigma_1 - \sigma_3)^2 + (\sigma_2 - \sigma_3)^2}}{\sqrt{2}} \tag{4.22}$$

The material points selected to compute the deviatoric stress are those inside four elements at the bottom left corner of the wall (Figure 4.19b). These points were chosen because, in this section of the wall, the deviatoric stress is a maximum. It is observed that the results in Figure 4.19 are consistent with each other, in that the maximum deviatoric stress occurs at the same time as the maximum contact pressure. Also, due to the elastic behaviour of the wall, an oscillatory behaviour is observed.

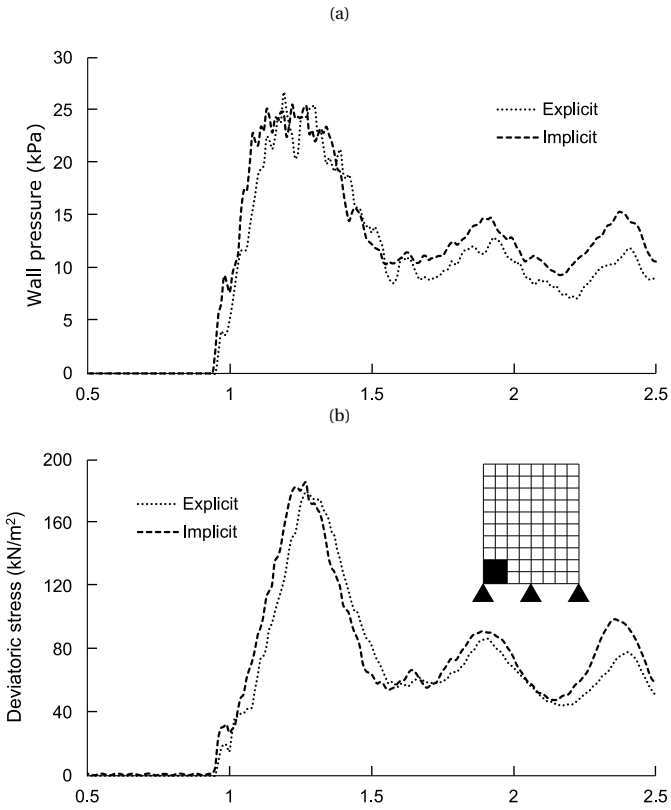

Figure 4.19: a) Contact pressure at the wall surface, and b) deviatoric stress at the base of the wall

4.4.3. COMPUTATIONAL TIME

The time steps used and the computational times recorded for the simulations from Sections 4.4.1 and 4.4.2 are presented, to further assess the capability of the implicit solution. Note that the time steps chosen for the geotechnical simulations were based on the results obtained from the benchmarks (i.e. the largest time steps which returned accurate results). They were compiled using Intel Parallel Studio XE, and run on a computer with an Intel Xeon E5-1620 processor and 16 GB RAM. However, it should be noted that no special effort was made to optimize the code (e.g. no parallel computing), which means that the installed RAM was not exploited to its maximum capacity.

Table 4.4 summarises the implicit/explicit time step relationship, computation time (CT), and memory usage (MU) between the simulations. It is observed that, in most of the simulations (i.e. except the block collision simulation), the time step used for the implicit simulations is 10 times larger than the time step used for the explicit simulations. Due to the use of a larger time step, the computation time is smaller (in most of the simulations) when using the implicit solution. The reason for the larger computation time in the foundation simulation is the incompressibility of the soil, which leads to more iterations in order to reach equilibrium. However, in more realistic simulations, where

contact only occurs during part of the simulation, the implicit algorithm should lead to substantial computation time savings. Finally, it is observed that the memory usage is almost the same with both formulations. This is because the implicit scheme uses the skyline storage technique, which is highly effective in manipulating the data during the simulations. Nevertheless, when the simulated problems contain a large number of points (e.g. the foundation and soil-wall collision problems), the differences in memory usage are more evident.

Table 4.4: Time step relationship, computation time and memory usage for each simulation

Problem analysed	Implicit Δt / Explicit Δt	Explicit CT (min)	Implicit CT (min)	Explicit MU (MB)	Implicit MU (MB)
Block collision	5	1.93	0.42	1.9	2.1
1D vibration bar	10	11.64	3.6	3	3.5
Sliding block	10	8.4	2.27	2.3	2..5
Foundation settlement	10	305	335	66.8	76.6
Soil-wall collision	10	94.33	68.26	80.9	86.6

4.5. CONCLUSIONS

In this Chapter, an implicit contact solution was developed for MPM, based on existing explicit procedures and using the Newton-Raphson iterative procedure and Newmark's time integration scheme. The relative performance of the formulation with respect to an explicit scheme was investigated through analysing three benchmark problems. It was shown that the results obtained using the explicit and implicit methods were almost identical. It was observed that both methods dissipate energy in a similar manner due to an inconsistency between the contact loads and the increment of material point stresses, which is proportional to both the time step and mesh size discretisation. Moreover, it was observed that by reducing the time step and mesh size to realistically small sizes, a reasonable energy conservation can be achieved. The ability of the method for simulating geotechnical problems was demonstrated through the analysis of foundation slab settlement in a cohesive soil, in which the failure mechanism and the bearing capacity obtained were similar to Terzaghi's analytical solution, and through the analysis of the collision of a mass of soil against a protection wall. Finally, it was shown that the simulation using the implicit approach is faster when the contact loads in the problem are moderate; otherwise, the computational time can be similar to the explicit approach.

REFERENCES

Bardenhagen, S., Brackbill, J. & Sulsky, D. (2000). The material-point method for granular materials. *Computer Methods in Applied Mechanics and Engineering* **187**, No. 3-4, 529–541.

Bardenhagen, S., Guilkey, J. E., Roessig, K., Brackbill, J., Witzel, W. & Foster, J. (2001). An improved contact algorithm for the material point method and application to stress propagation in granular material. *CMES: Computer Modeling in Engineering & Sciences* **2**, No. 4, 509–522.

Chen, Z.-P., Zhang, X., Qiu, X.-M. & Liu, Y. (2017). A frictional contact algorithm for implicit material point method. *Computer Methods in Applied Mechanics and Engineering* **321**, 124–144.

Coombs, W. M., Charlton, T. J., Cortis, M. & Augarde, C. E. (2018). Overcoming volumetric locking in material point methods. *Computer Methods in Applied Mechanics and Engineering* **333**, 1–21.

González Acosta, J., Zheng, X., Vardon, P., Hicks, M. & Pisano, F. (2019). On stress oscillation in mpm simulations involving one or two phases. In *MPM 2019: 2nd International Conference on the Material Point Method for Modelling Soil–Water–Structure Interaction*.

González Acosta, J. L., Vardon, J. & Hicks, M. (2020). Development of an implicit contact technique using the material point method. *Submitted for publication* .

González Acosta, J. L., Vardon, P. J., Hicks, M. A. & Pantev, I. (2018). The use of MPM to estimate the behaviour of rigid structures during landslides. In *NUMGE 2018: 9th European Conference on Numerical Methods in Geotechnical Engineering*, vol. 9, CRC Press.

Guilkey, J. E. & Weiss, J. A. (2003). Implicit time integration for the material point method: Quantitative and algorithmic comparisons with the finite element method. *International Journal for Numerical Methods in Engineering* **57**, No. 9, 1323–1338.

Homel, M. A. & Herbold, E. B. (2017). Field-gradient partitioning for fracture and frictional contact in the material point method. *International Journal for Numerical Methods in Engineering* **109**, No. 7, 1013–1044.

Huang, P., Zhang, X., Ma, S. & Huang, X. (2011). Contact algorithms for the material point method in impact and penetration simulation. *International Journal for Numerical Methods in Engineering* **85**, No. 4, 498–517.

Jiang, Q. & Yeung, M. (2004). A model of point-to-face contact for three-dimensional discontinuous deformation analysis. *Rock Mechanics and Rock Engineering* **37**, No. 2, 95–116.

Li, F., Pan, J. & Sinka, C. (2009). Contact laws between solid particles. *Journal of the Mechanics and Physics of Solids* **57**, No. 8, 1194–1208.

Liu, C. & Sun, W. (2020). Ils-mpm: an implicit level-set-based material point method for frictional particulate contact mechanics of deformable particles. *Computer Methods in Applied Mechanics and Engineering* **369**, 113168.

Ma, J., Wang, D. & Randolph, M. (2014). A new contact algorithm in the material point method for geotechnical simulations. *International Journal for Numerical and Analytical Methods in Geomechanics* **38**, No. 11, 1197–1210.

Müller, A. & Vargas, E. A. (2019). Stability analysis of a slope under impact of a rock block using the generalized interpolation material point method (GIMP). *Landslides* **16**, No. 4, 751–764.

Nairn, J. (2013). Modeling imperfect interfaces in the material point method using multimaterial methods. *Computer Modeling in Engineering and Sciences* **1**, No. 1, 1–15.

Oden, J. & Pires, E. (1984). Algorithms and numerical results for finite element approximations of contact problems with non-classical friction laws. *Computers & Structures* **19**, No. 1-2, 137–147.

Pantev, I. (2016). *Contact modelling in the material point method*. Master's thesis, Delft University of Technology.

Sloan, S. W., Abbo, A. J. & Sheng, D. (2001). Refined explicit integration of elastoplastic models with automatic error control. *Engineering Computations: International Journal for Computer-Aided Engineering* **18**, No. 1-2, 121–194.

Smith, I. M., Griffiths, D. V. & Margetts, L. (2013). *Programming the finite element method*. John Wiley & Sons.

Sulsky, D., Chen, Z. & Schreyer, H. L. (1994). A particle method for history-dependent materials. *Computer Methods in Applied Mechanics and Engineering* **118**, No. 1-2, 179–196.

Terzaghi, K. (1943). *Theoretical soil mechanics*. John Wiley & Sons.

Wang, B., Hicks, M. & Vardon, P. (2016a). Slope failure analysis using the random material point method. *Géotechnique Letters* **6**, No. 2, 113–118.

Wang, B., Vardon, P. J., Hicks, M. A. & Chen, Z. (2016b). Development of an implicit material point method for geotechnical applications. *Computers and Geotechnics* **71**, 159–167.

Xiao-Fei, P., Ai-Guo, X., Guang-Cai, Z., Ping, Z., Jian-Shi, Z., Shang, M. & Xiong, Z. (2008). Three-dimensional multi-mesh material point method for solving collision problems. *Communications in Theoretical Physics* **49**, No. 5, 1129.

Zhang, X., Sze, K. & Ma, S. (2006). An explicit material point finite element method for hyper-velocity impact. *International Journal for Numerical Methods in Engineering* **66**, No. 4, 689–706.

5

STUDY OF LANDSLIDES AND THE INTERACTION WITH STRUCTURES USING IMPLICIT MPM

In this Chapter, the implicit contact technique developed in Chapter 4 is studied by simulating soil-structure interaction problems and a landslide. First, the behaviour of a retaining structure is studied during the impact of a mass of soil, for different foundation conditions. In this simulation, structural behaviour in the context of rotation, sliding, pull-out and overturning is observed, and both passive and active soil failures occur. Then, a landslide triggered by construction procedures is analysed, in which a combination of deep and shallow complex failure mechanisms are observed.

Parts of this chapter appear in González Acosta *et al.* 2020.

5.1. INTRODUCTION

Landslides are natural hazards in which a large mass of debris, mud or rock moves down-slope at a range of velocities. The triggering causes are diverse; usually a landslide is activated because of (i) the rapid loss of material strength, as occurs when the pore pressure in the soil increases during extreme rainfall (Wang & Sassa 2003, Collins & Znidarcic 2004, Moriwaki *et al.* 2004, Iverson *et al.* 2015, Wang *et al.* 2018), or (ii) the rapid application of external loads, as occurs during earthquakes (Rodrıguez *et al.* 1999, Nakamura *et al.* 2014, Li *et al.* 2012). Nonetheless, the occurrence of slow landslides, in which movement can take place over several days or years, is also possible. These landslides are usually undergoing creep (Van Asch 1984, Van Asch & Van Genuchten 1990, Furuya *et al.* 1999), or the complex geometric and geologic characteristics of the site prevents fast sliding of the soil (Rico *et al.* 1976). In Figure 5.1, typical slope failures are illustrated. Figure 5.1a shows a retrogressive failure, in which an initial shear band (SB 1) develops, causing the material to slide (FV 1). Then, if the down-slope material cannot support the imbalance in loads of the backslope, a new SB develops, causing the slide of another block of material (FV 2). This process can repeat several times, causing multiple slope failures. In Figure 5.1b, a translational failure is observed, in which a segment of material detaches and moves a short or large distance. In contrast with the retrogressive failure, the mass of soil affected is larger and further sequential failures may not occur. Some of the most typical slope failure types are described in Locat *et al.* (2011) and Vardon *et al.* (2017). Moreover, Wang *et al.* (2016a) showed that failures are often a combination of multiple mechanisms.

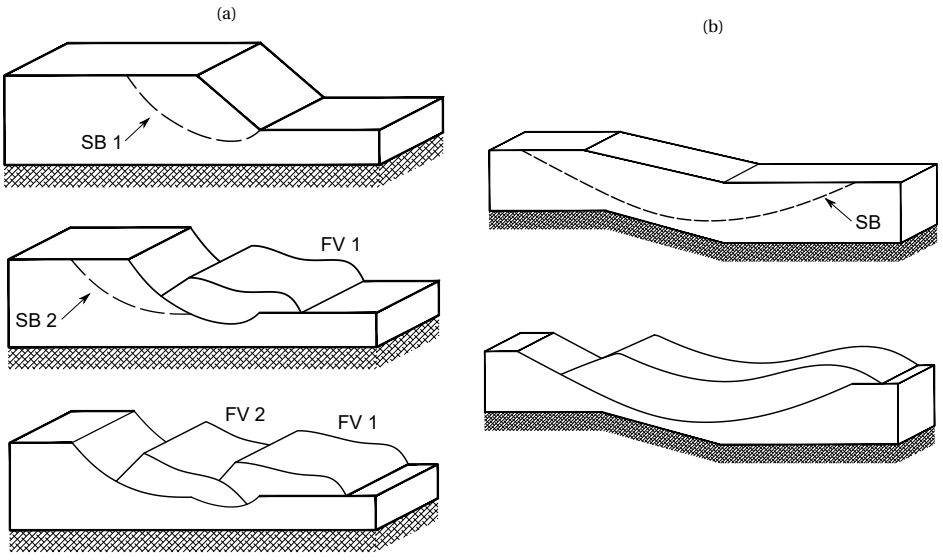

Figure 5.1: a) scheme of a retrogressive failure, and b) scheme of a translation failure (after Locat *et al.* 2011)

Regardless of the type of failure or triggering cause, damage to infrastructure and/or loss of human lives are possible. It is estimated that landslides are responsible for around 17% of fatalities due to natural hazards, most of them being in America (North, Central and South) and China, and economic losses scale to several billions USD annually (Kjekstad & Highland 2009). In order to mitigate possible damage caused by landslides, it is important to develop tools capable of simulating real geotechnical scenarios in which slope failure or landslides can occur, including interaction with neighbouring structures.

The finite element method (FEM) is a numerical technique frequently used to study geotechnical problems, such as slope stability and the interaction with protection/retaining structures (Cai & Bathurst 1995, Chen & Martin 2002, Mishra *et al.* 2017). Nevertheless, in FEM, the connectivity between the mesh and the domain is essential and does not allow for the simulation of large deformations, thereby reducing the range of problems that can be studied. To date, numerous papers have reported the use of MPM to simulate interaction between landslides and structures (Mast *et al.* 2014, Li *et al.* 2016, Dong *et al.* 2017, Conte *et al.* 2019). Nevertheless, these attempts have generally failed to depict a realistic landslide simulation and the interaction with surrounding structures, due to the use of (i) unrealistic initial conditions (which leads to implausible failure triggers), (ii) simplified solution procedures (which ignore a realistic contact simulation), and (iii) poor stress recovery techniques (which reduces the accuracy of the simulations).

In this section, the procedures developed in Sections 3.2 and Chapter 4 (i.e. DM-GC and the implicit contact method) are used to study the use of the implicit contact MPM for geotechnical problems.

5.2. APPLICATION OF THE IMPLICIT CONTACT METHOD

The proposed implicit contact method is applied to two plane strain geotechnical problems. The first problem consists of a vertical cutting, which fails under self-weight and collides against a rigid wall. The second problem consists of a large slope, which fails, due to the removal of material and inadequate construction of retaining structures, dragging all neighbouring structures in the failure. In both problems, the progressive failure of the soil and the response of the structures after contact are investigated.

5.2.1. VERTICAL CUT

A 2D elasto-plastic vertical cut has been simulated using a von Mises constitutive model incorporating post-peak softening (Wang *et al.*, 2016b), which, after failure, collides against a rigid wall. Figure 5.2 shows the generic problem domain (including dimensions in meters) and boundary conditions. This problem has been analysed twice, by considering two different geometries. In the first simulation, the wall is founded on the ground surface (i.e. $s = 0$), and the foundation soil layer is shallow ($h_2 = 0.25$ m). In the second simulation, the foundation soil layer is deeper ($h_2 = 1.0$ m), and the rigid wall is founded at a depth of $s = 0.5$ m. The background mesh element size is $\Delta x = \Delta y = 0.05$ m and each element contains initially four equally distributed material points (i.e. at the centre of each element quadrant).

The unit weights of the soil and the wall are $\gamma_s = 18\,kN/m^3$ and $\gamma_w = 20\,kN/m^3$, respectively. The elastic parameters for the soil are Young's modulus, $E = 1.0 \times 10^3$ kPa and Poisson's ratio, $\upsilon = 0.35$, and the peak shear strength parameters for the soil cut and foundation soil are $s_{pv} = 10$ kPa and $s_{pf} = 30$ kPa, respectively. The residual shear strength and the softening modulus are the same for both soils, and are equal to $s_r = 3$ kPa and $H_s = -30$ kPa, respectively. The elastic parameters for the rigid wall are $E = 1.0 \times 10^4$ kPa and $\upsilon = 0.38$.

At the left and right boundaries of the domain, the nodes are on rollers to avoid displacement in the horizontal direction, whereas the nodes are fully fixed at the bottom boundary. The initial stresses in the domain were generated by linearly increasing the gravity load. During these steps, the kinematics were not considered and the material points stayed in their original positions (i.e. no movement was allowed). After the gravity load had reached its maximum value, the kinematics were included, and the material points were released. Then, due to the development of large shear stresses at the cutting toe and the low strength of the material, the failure was triggered. The failure process was modelled using a time step of $\Delta t = 1.0 \times 10^{-4}$ s for the simulation.

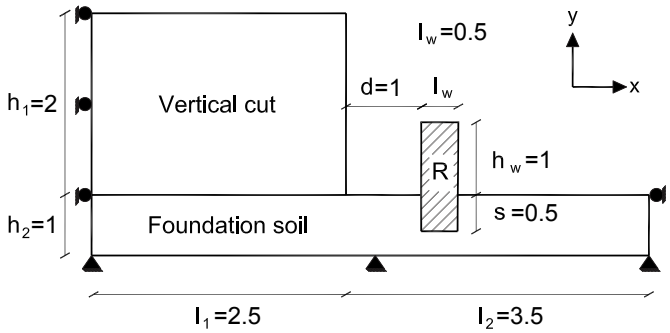

Figure 5.2: Vertical cut sketch (not to scale; dimensions in meters)

Figure 5.3 shows the interaction between the vertical cut and the rigid wall, by way of the plastic deviatoric strain and deviatoric stress distributions, for the simulation with no wall foundation. Note that the deviatoric stress range is fixed to maximum of 25 kPa, allowing a better visualization of the stresses in the vertical cut. In Figure 5.3a and 5.3b, the initial condition of the simulation is shown (at the instant the material points are released). It is seen that the material points have not yet moved, although there is a stress concentration at the base of the cut. In Figure 5.3c and 5.3d, the simulation at the instant of the contact (t = 0.7 s) is shown. At this stage of the analysis, the shear band already traverses the height of the vertical cut and a large block of soil is moving towards the retaining structure. In Figure 5.3e and 5.3f, the simulation has reached time t = 1 s. In this case, the contact has already occurred and, due to the kinematic forces applied by the soil, the wall is being pushed and slides to the right. It is seen that a large portion of soil close to the contact zone undergoes plasticity due to the large contact forces developed. Finally, Figure 5.3g and 5.3h show the final step of the simulation corresponding to time t = 3 s. By this stage of the analysis the rigid wall has fallen over after being pushed a considerable

distance. Furthermore, at the base of the wall, the soil and the wall are not in contact and the soil has formed a circular scarp. This occurred during the fall of the wall, due to the rotational movement of the wall pushing the soil away.

Figure 5.4 shows the results of the simulation with the wall foundation and a deeper soil foundation. In Figure 5.4a and 5.4b, the initial plastic deviatoric strains and deviatoric stresses are shown, while Figure 5.4c and 5.4d shows the stresses and strains at the initiation of contact (t = 0.8 s). At this point, the results are similar to the previous simulation (as expected), but the contact occurs 0.1 s later. This time difference is attributed to the inclusion of the foundation, which has a small influence on the growing velocity of the failure mechanism. In Figure 5.4e and 5.4f, the results during the contact at a time of t = 1 s are quite different from the previous simulation. It is seen that the rigid wall, rather than sliding, rotates because of the support given by the foundation soil. A small zone in the foundation soil at the back of the wall develops into a passive failure wedge, and the wall separates from the soil in areas where tension would occur, highlighting the advantage of using the contact algorithm. Finally, at the end of the simulation (Figures 5.4g and 5.4h) the wall is not far from its original position and is able to prevent further movement of the failed soil mass.

Finally, note that an interface is observed (i.e. a notable difference of deviatoric stresses) between the vertical cut and the foundation soil. This interface is cased by the different peak strengths of the two materials. During an increment of the gravity load, the material of the vertical cut reaches its maximum shear strength, preventing further increment of the deviatoric stress. On the other hand, the deviatoric stresses in the foundation soil keep increasing.

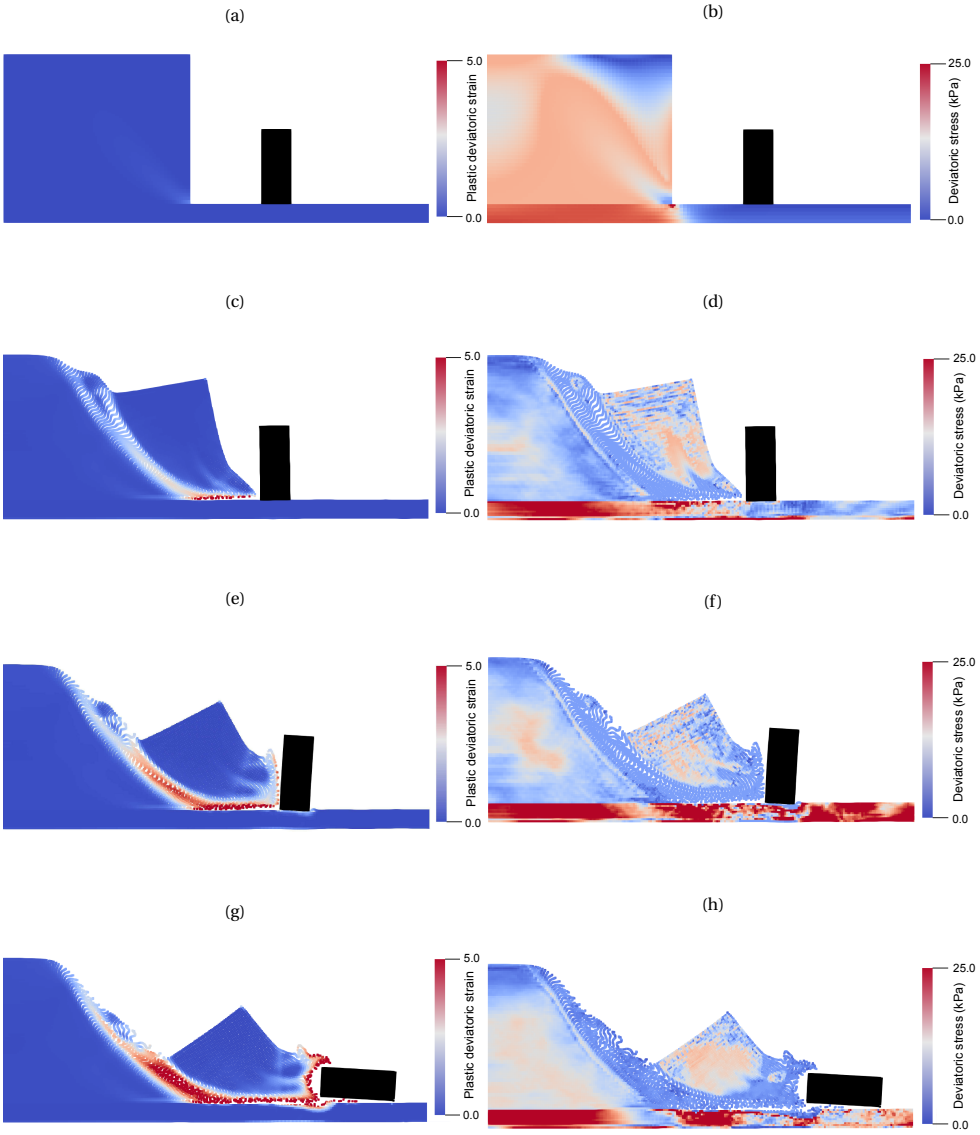

Figure 5.3: Slope initial state (a, b), slope at the instant of collision, t = 0.7 s (c, d), slope during collision, t = 1 s (e, f), and final configuration (g, h), showing contours of plastic deviatoric strain and deviatoric stress

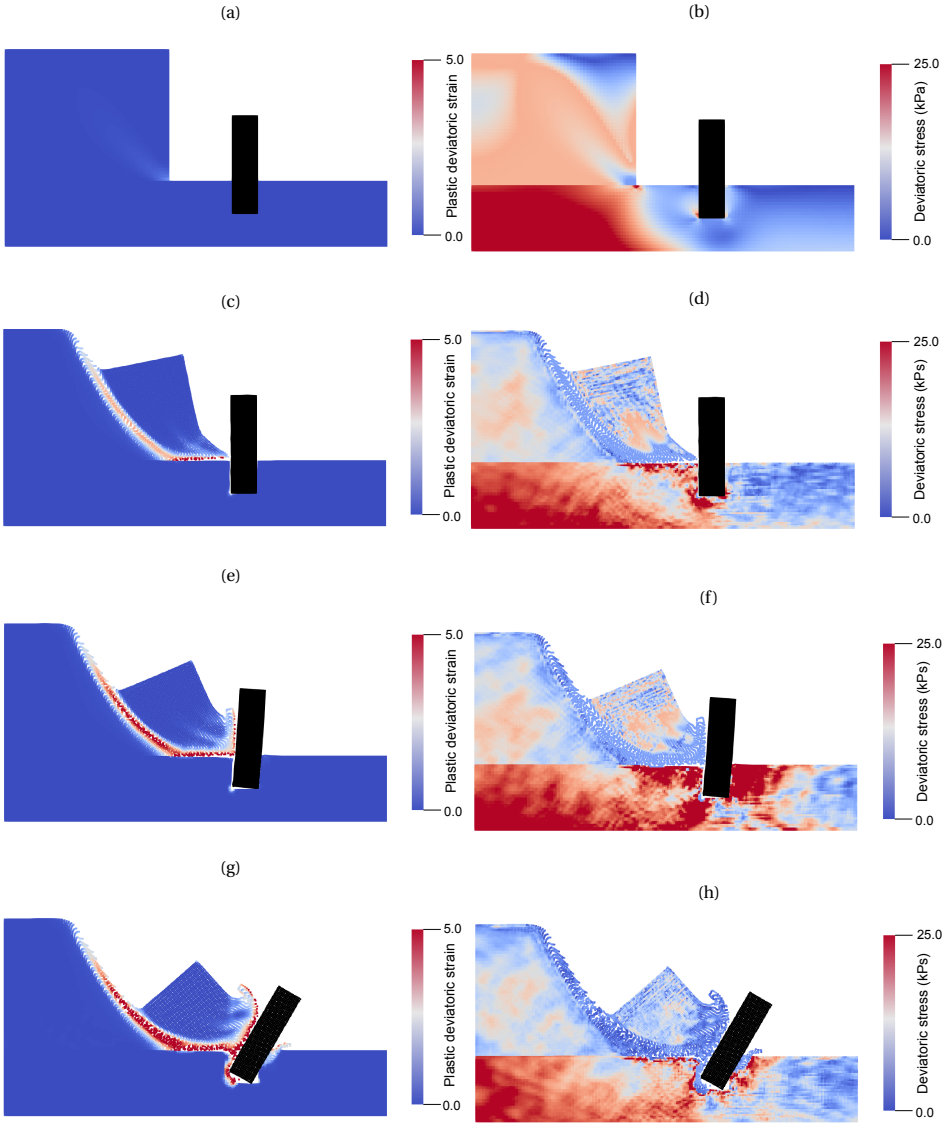

Figure 5.4: Slope initial state (a, b), collision instant t = 0.8 s (c, d), interaction at time t = 1 s (e, f), and final configuration (g, h), showing contours of plastic deviatoric strain and deviatoric stress

In Figures 5.5 and 5.6, the magnitude of the contact loads developed at the wall surface during the collision and the displacement of the wall, respectively, are shown for the second simulation. Figure 5.5a shows the contact loads before the collision. In this case, the loads are caused only by the self weight of the wall and the soil, since collision has not yet occurred. Figure 5.5b shows the contact loads at the instant of the collision (t = 0.8 s); since the area of the contact is small and the velocity of the soil is large, the contact loads are high. Figure 5.5c shows the evolving situation during the collision at time t = 1 s. In this case, since the soil begins to accumulate at the wall, the contact loads are distributed and the magnitudes reduce. It is also seen that, at the base of the wall on the left side, there are large forces due to the rotation of the wall. Finally, Figure 5.5d shows the final position of the wall (t = 1.5 s). In this case, the contact loads have reduced since the velocity of the material is equal to zero (i.e. the kinetic forces are equal to zero). It should be noted that the magnitudes of the vectors representing the contact loads have different ranges in each sub-figure to enhance visualisation.

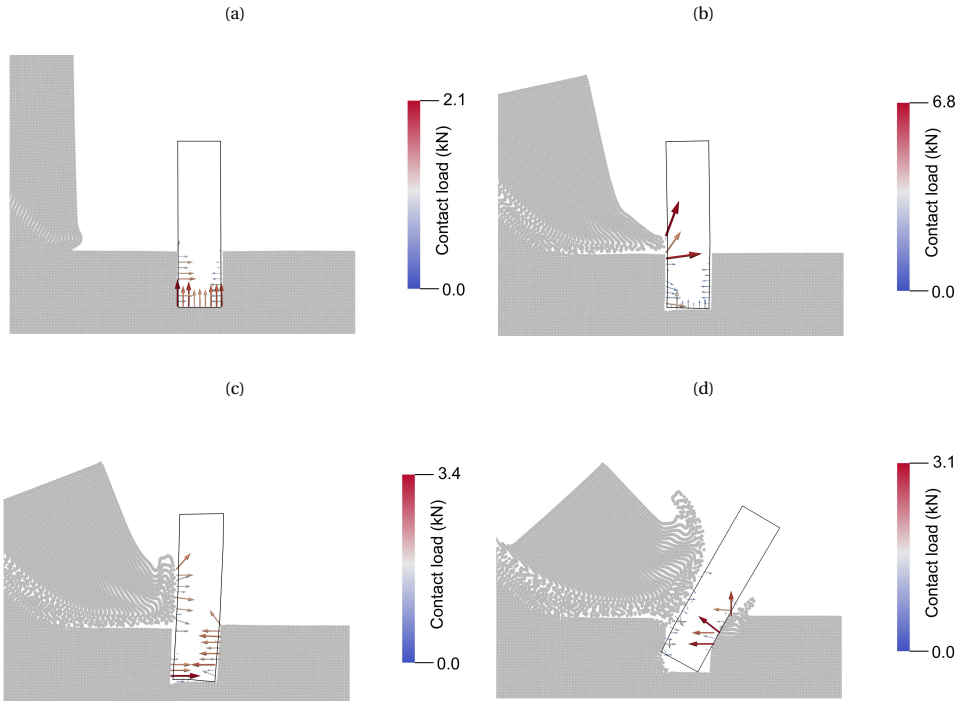

Figure 5.5: a) initial contact loads, b) contact loads at instant of collision (t = 0.8 s), c) distributed contact loads (t = 1 s), d) contact loads at the end of the simulation. Note the different scaling in each sub-figure

In Figure 5.6, the average horizontal displacement of four material points at the top of the wall (labeled mps) is plotted for both simulations. The selected material points are located at the centre of the wall. As observed, the displacement of the surface wall is at least twice as big as the displacement of the embeded wall. At the end of the simulations, the maximum displacements are $d^{S}_{max} = 1.59$ m and $d^{E}_{max} = 0.67$ m, for the surface and embedded walls, respectively. The simulations were run using an Intel Xeon E5-1620 processor and completed in 9 hours and 4 minutes for the problem considering the wall at the surface (using 11,040 material points), and in 12 hours and 55 minutes for the problem considering the embedded wall (using 18,400 material points).

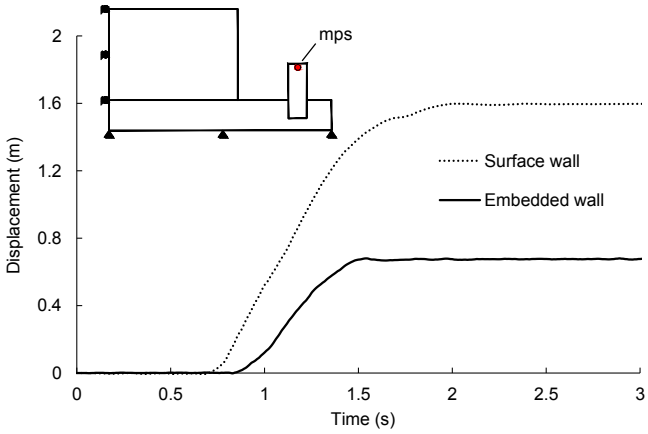

Figure 5.6: Rigid wall horizontal displacement

5.2.2. LANDSLIDE

The analysis of an initially stable slope, which undergoes several construction phases before failure, has been performed. The soil follows the same type of constitutive behaviour as in the previous example. Also, a depth dependent strength is included, in which the peak shear strength increases linearly with the depth, from $s_p = 15$ kPa at the soil surface to $s_p = 80$ kPa at the base of the soil layer. The residual cohesion and the softening modulus are $s_r = 5$ kPa and $H_s = -30$ kPa, respectively. The elastic parameters for the soil are Young's modulus, $E = 1.5 \times 10^3$ kPa, and Poisson's ratio, $\upsilon = 0.40$. The elastic parameters for the structural elements are $E = 5.0 \times 10^4$ kPa, and $\upsilon = 0.35$.

In Figure 5.7, the main features of the slope are shown, including the construction stages and dimensions (in meters). Figure 5.7a shows the initial slope, comprising a single homogeneous soil layer of constant depth H_1. The element size is $\Delta x = \Delta y = 0.5$ m, and each element initially contains four equally distributed material points. The entire layer is supported by a rigid material, simulated by the fixed bottom boundary. Figure 5.7b indicates the excavation process, which involves three steps: (i) excavation 1 (exc - 1) at a distance L_4 from the top of the slope, (ii) excavation 2 (exc - 2) at a distance L_5 from the first excavation, and (iii) excavation 3 (exc - 3) at a distance L_6 from the second excavation. Finally, Figure 5.7c shows the wall foundation depths and geometry of the structure. The thickness of the columns and floors of the structure are 0.75 m and 1.0 m, respectively.

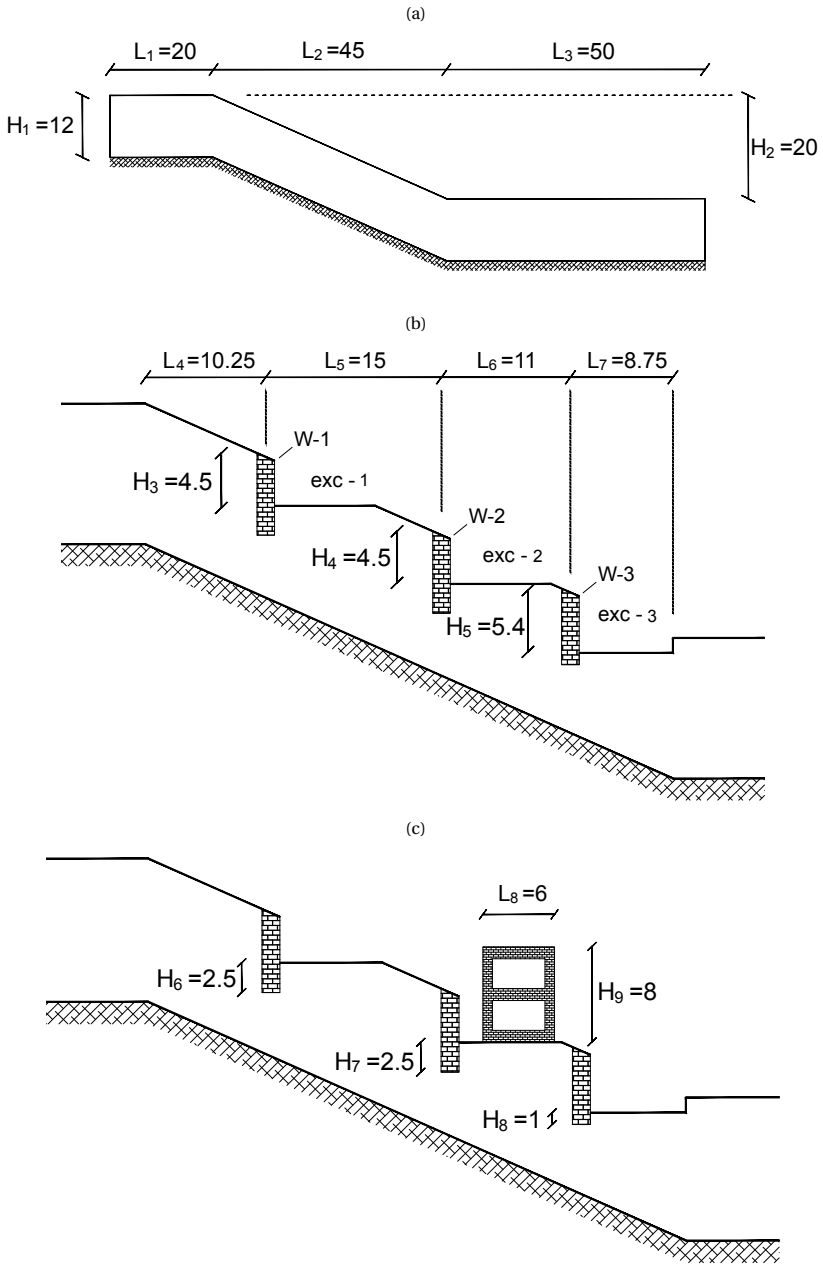

Figure 5.7: a) Slope dimensions, b) construction stages, and c) building and wall foundations. Note unequal scales to enable better visualisation; dimensions in meters

The excavation procedure and the installation of the structural elements was simulated as follows. Each excavation was executed by removing columns of material points,

in 50 steps, in which each column had a width of one element. Figure 5.8 shows an example of the excavation procedure. Note that this example is only illustrative, and that the dimensions are not the same as in the simulation. These excavations were executed sequentially, i.e. after excavation exc - 1 was completed, exc - 2 began. Each retaining wall is inserted in a single step by changing the properties of ground material points to structural material points. The insertion of each wall is performed at the same time as the removal of the last portion of soil in each excavation. The thickness of each retaining wall is equal to 1.5 m. To reduce the impact of inserting a wall in a single step, an initial wall gravity of $g_{ini} = 0.3g$ is used. This wall gravity is increased in increments of $\Delta g = 1.0 \times 10^{-4}$ g in each time step until reaching 1g. The structure is placed in a single step by adding material points in the domain. Similar to the retaining walls, the initial structure gravity is $g_{ini} = 0.3g$ and this is increased in increments of $\Delta g = 1.0 \times 10^{-4}g$ each time step until reaching 1g. The time step used for the simulation is $\Delta t = 1.0 \times 10^{-4}$ s.

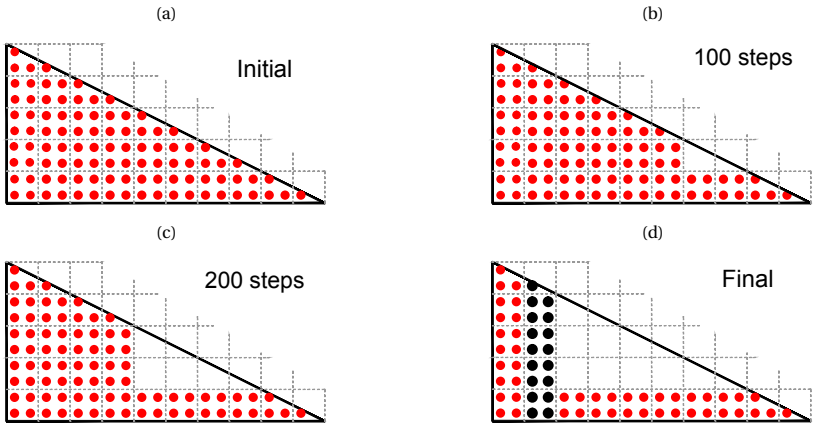

Figure 5.8: a) Initial slope, b) after two excavation steps, c) after four excavation steps, and d) excavation finalized, including installation of retaining wall (depicted by black material points)

The initial stresses in the slope are assigned in a single step using a static approach (i.e. by removing the kinematics), i.e. $\sigma_y = \gamma_{soil} h_y$ and $\sigma_x = \sigma_y K_0$, in which γ_{soil} is the soil unit weight equal to 17.5kN/m^3, h_y is the vertical distance between the soil surface and the material point, and K_0 is the coefficient of earth pressure at rest equal to 0.7. Meanwhile, the material points are kept in their original positions (i.e. no movement allowed) in this step. After the first step, the material points are free to move, including during the construction steps.

Figures 5.9 and 5.10 show the plastic deviatoric strains and the deviatoric stresses, respectively, during the landslide. The results observed are obtained from the instant after concluding the construction process (i.e. excavations, installation of retaining walls and structure) until the end of the landslide. Figure 5.9a shows the instant immediately after including the structure, in which plastic strains are not visible yet. Nonetheless, Figure 5.10a shows a large concentration of shear stresses below the walls. Figure 5.9b shows the simulation after 0.7 s. It is observed that the wall W-3 at the base of the slope begins to rotate, separating from the soil behind it. This is a consequence of both the weight of

the structure, which increases the horizontal pressure applied to the wall, and the lack of support on the downslope side. Moreover, the soil pushing the wall W-3 moves, thereby causing the movement of wall W-2, which, at the same time, develops plastic strains at its base. Additionally, Figure 5.10b shows that, at the soil-boundary interface, large shear stresses develop due to the movement of the soil, and small plastic regions start initiating at this interface. Since it was the inclusion of the building that caused the wall W-3 to fall over, and thereby the subsequent soil displacements and development of large shear stresses at the soil-boundary interface, it can be stated that the building triggered the landslide.

Figure 5.9c shows the simulation after 1.1 s. It is seen that the wall W-3 has rotated a considerable distance, and that the soil behind the wall begins to slide downwards. The movement of the soil triggers further shear bands, at the base of each wall and at the soil-boundary interface. It is also seen that the structure is tilting and that walls W-1 and W-2 are separating from the soil. Figure 5.10c shows that the plastic strains at the soil-boundary interface extend almost the whole length of the inclined boundary, and that the plastic strains at the base of the walls have grown significantly, reaching almost the soil surface.

Figure 5.9d shows the simulation after 1.75 s. It is seen that the wall W-3 has fallen over, allowing the soil behind to slide more freely. The shear bands have extended to the soil surface, except for between the middle and bottom walls where the shear band connects the bases of both walls, and numerous shallow failures (which exhibit typical rotational mechanisms) have formed. Figure 5.10d shows that the deviatoric stresses at the soil-boundary interface length have dropped to residual values. Besides, it is seen that deviatoric stresses are still large at the leading edge end of the bottom shear band, which indicates that the plastic strains are still developing.

In Figure 5.9e and 5.10e, it is seen that the shear band at the base of the soil layer now exceeds the length of the slope, to form a translational failure mechanism which encloses the multiple shallow failures. The walls W-1 and W-2, and the structure, are being dragged by the soil, while the wall W-3 is being pushed away in front of the landslide. In addition, due to the large kinematic forces, another shear band begins to grow at the base of the horizontal section of the slope. Finally, Figures 5.9f and 5.10f show the final step, in which the soil has reached nearly static conditions. It is seen that most of the soil is in the plastic condition, and that it exhibits numerous failure surfaces. The shear band at the base of the horizontal section of the slope has grown enough to reach the soil surface at the end of the domain. Note that the right vertical boundary causes the vertical growth of the plastic shear band at this location, which would not occur had a larger horizontal domain been used. Finally, it is seen that all the structures have ended up buried in the ground.

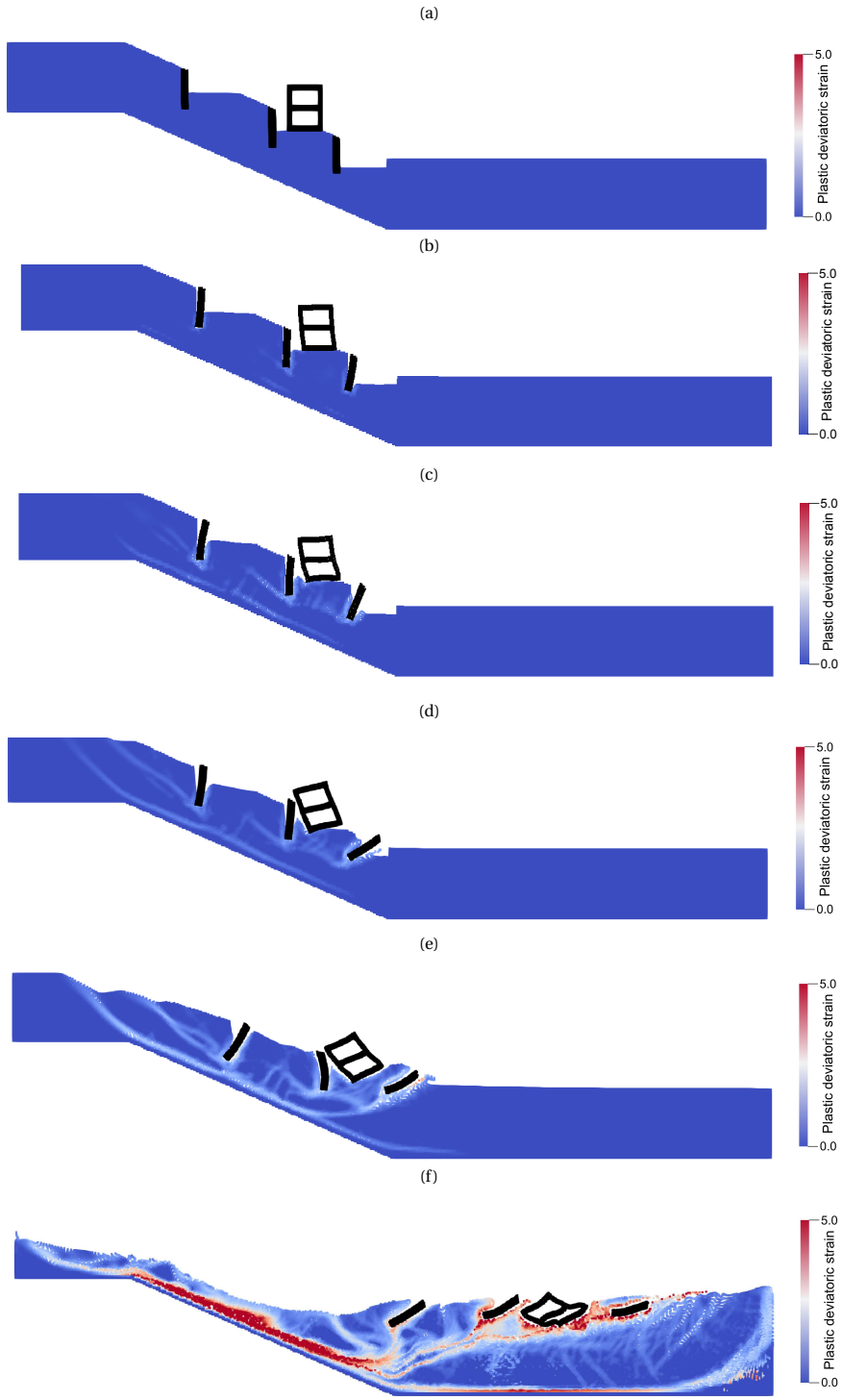

Figure 5.9: Landslide plastic deviatoric strains after a) 0.14 s, b) 0.7 s, c) 1.1 s, d) 1.75 s, e) 3.05 s, and f) 10 s

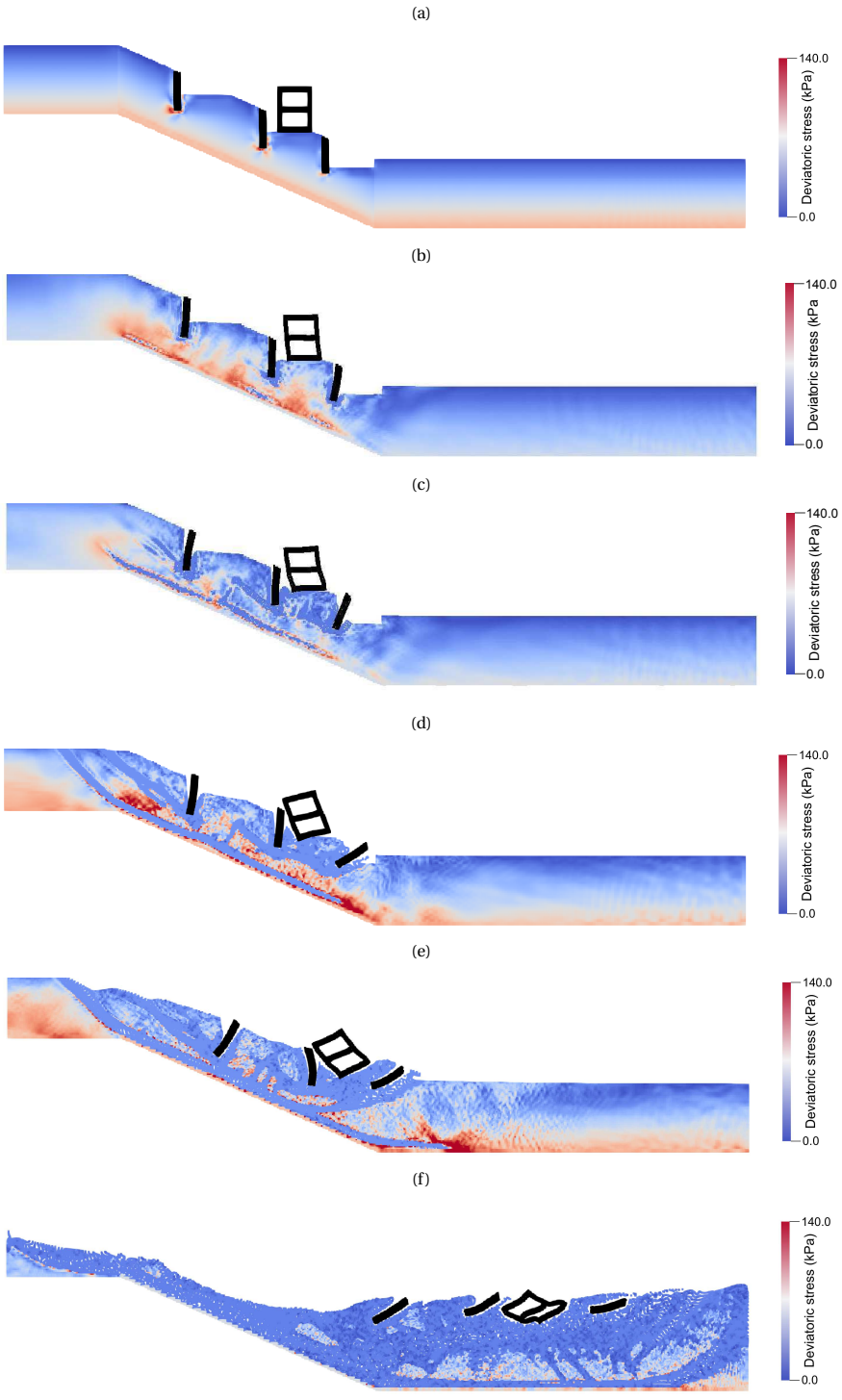

Figure 5.10: Landslide simulation and deviatoric stresses after a) 0.14 s, b) 0.7 s, c) 1.1 s, d) 1.75 s, e) 3.05 s, and f) 10 s

Figure 5.11 shows the displacements and velocities of the structures, which were obtained from an average of the results from four material points located at the centre of each structure (denoted with a solid circle in Figure 5.11a). In Figure 5.11a, the displacement of each structure is shown, with the labels A, B, C, D, E and F indicating the times corresponding to the results shown in parts (a) to (f) of Figures 5.9 and 5.10). It is observed that, after 10 seconds, the structures have moved nearly 50 meters. The vertical wall nearest the bottom of the slope (S3) has moved the furthest because it has fewest obstacles in front of it. Similar results are observed in Figure 5.11b, in which the vertical wall S3 reaches the maximum velocity (close to 10 m/s), whereas the rest of the structures reach similar velocities (around 6 m/s). The type of information illustrated in Figure 5.11 is necessary to evaluate the consequences of a landslide. This simulation was completed in 215 hours with a total of 25,766 material points, and used the same processor as in the vertical cutting problem.

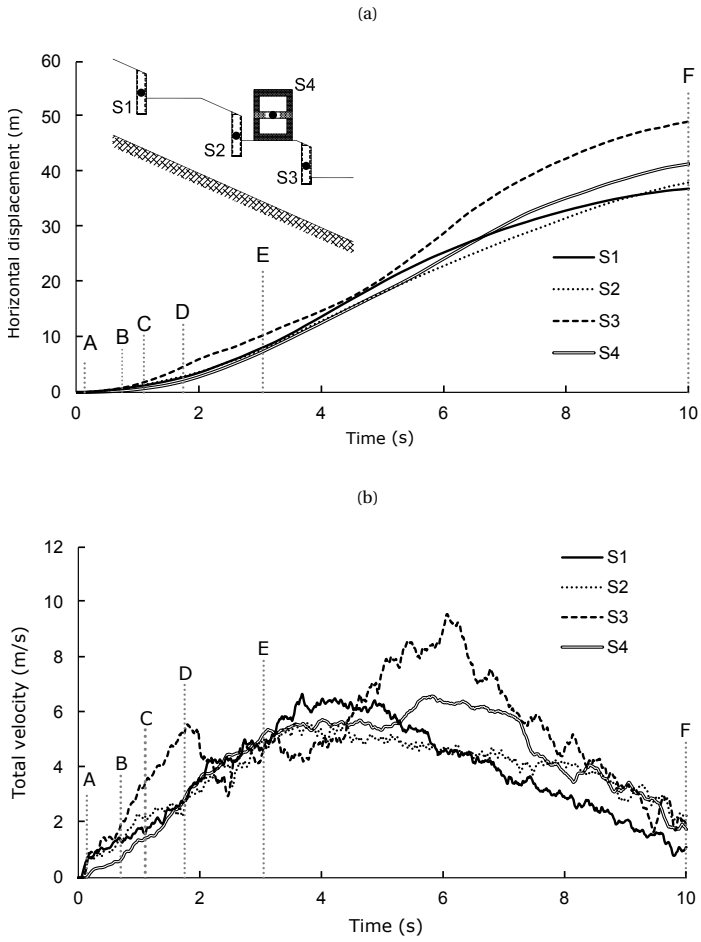

Figure 5.11: a) Displacements, and b) velocities of the structures

5.3. CONCLUSION

The DM-GC technique developed in Chapter 3 has been combined with the implicit contact formulation developed in Chapter 4 to simulate complex geotechnical problems. The method was able to capture realistic soil-structure interaction and a large variety and combination of failure modes. It was demonstrated that the interaction between the soil and multiple structures is possible. The method was able to capture some interesting features such as the sliding and rotation of structures pushed by the soil, the development of passive and active soil failure mechanisms, and the combination of rotational and translational slope failures, thereby validating the technique for the assessment of protection structures against the consequences of landslides.

REFERENCES

Cai, Z. & Bathurst, R. J. (1995). Seismic response analysis of geosynthetic reinforced soil segmental retaining walls by finite element method. *Comput Geotech* **17**, No. 4, 523–546.

Chen, C.-Y. & Martin, G. (2002). Soil–structure interaction for landslide stabilizing piles. *Comput Geotech* **29**, No. 5, 363–386.

Collins, B. D. & Znidarcic, D. (2004). Stability analyses of rainfall induced landslides. *J Geotech Geoenviron Eng* **130**, No. 4, 362–372.

Conte, E., Pugliese, L. & Troncone, A. (2019). Post-failure stage simulation of a landslide using the material point method. *Eng Geol* **253**, 149–159.

Dong, Y., Wang, D. & Randolph, M. F. (2017). Investigation of impact forces on pipeline by submarine landslide using material point method. *Ocean Eng* **146**, 21–28.

Furuya, G., Sassa, K., Hiura, H. & Fukuoka, H. (1999). Mechanism of creep movement caused by landslide activity and underground erosion in crystalline schist, Shikoku Island, southwestern japan. *Eng Geol* **53**, No. 3-4, 311–325.

González Acosta, J. L., Vardon, J. & Hicks, M. (2020). Study of landslides and the interaction with structures using implicit MPM. *Submitted for publication* .

Iverson, R. M., George, D. L., Allstadt, K., Reid, M. E., Collins, B. D., Vallance, J. W., Schilling, S. P., Godt, J. W., Cannon, C., Magirl, C. S. *et al.* (2015). Landslide mobility and hazards: implications of the 2014 Oso disaster. *Earth Planet Sci Lett* **412**, 197–208.

Kjekstad, O. & Highland, L. (2009). Economic and social impacts of landslides. In *Landslides–disaster risk reduction*, Springer, pp. 573–587.

Li, X., He, S., Luo, Y. & Wu, Y. (2012). Simulation of the sliding process of Donghekou landslide triggered by the Wenchuan earthquake using a distinct element method. *Environ Earth Sci* **65**, No. 4, 1049–1054.

Li, X., Wu, Y., He, S. & Su, L. (2016). Application of the material point method to simulate the post-failure runout processes of the Wangjiayan landslide. *Eng Geol* **212**, 1–9.

Locat, A., Leroueil, S., Bernander, S., Demers, D., Jostad, H. P. & Ouehb, L. (2011). Progressive failures in eastern Canadian and Scandinavian sensitive clays. *Can Geotech J* **48**, No. 11, 1696–1712.

Mast, C. M., Arduino, P., Miller, G. R. & Mackenzie-Helnwein, P. (2014). Avalanche and landslide simulation using the material point method: flow dynamics and force interaction with structures. *Comput Geosci* **18**, No. 5, 817–830.

Mishra, M., Vassallo, R., Santarsiero, G. & Masi, A. (2017). Landslide–pile–tunnel interaction by 2d and 3d finite element modelling. In *6th international conference on computational methods in structural dynamics and earthquake engineering (COMPDYN)*, pp. 15–17.

Moriwaki, H., Inokuchi, T., Hattanji, T., Sassa, K., Ochiai, H. & Wang, G. (2004). Failure processes in a full-scale landslide experiment using a rainfall simulator. *Landslides* **1**, No. 4, 277–288.

Nakamura, S., Wakai, A., Umemura, J., Sugimoto, H. & Takeshi, T. (2014). Earthquake-induced landslides: distribution, motion and mechanisms. *Soils Found* **54**, No. 4, 544–559.

Rico, A., Springall, G. & Mendoza, A. (1976). Investigations of instability and remedial works on the Tijuana–Ensenada highway, México. *Géotechnique* **26**, No. 4, 577–590.

Rodrıguez, C., Bommer, J. & Chandler, R. (1999). Earthquake-induced landslides: 1980–1997. *Soil Dyn Earthq Eng* **18**, No. 5, 325–346.

Van Asch, T. J. & Van Genuchten, P. (1990). A comparison between theoretical and measured creep profiles of landslides. *Geomorphology* **3**, No. 1, 45–55.

Van Asch, T. W. (1984). Creep processes in landslides. *Earth Surf Processes Land* **9**, No. 6, 573–583.

Vardon, P. J., Wang, B. & Hicks, M. A. (2017). Slope failure simulations with MPM. *J Hydrodyn* **29**, No. 3, 445–451.

Wang, B., Vardon, P. & Hicks, M. (2016a). Investigation of retrogressive and progressive slope failure mechanisms using the material point method. *Comput Geotech* **78**, 88–98.

Wang, B., Vardon, P. & Hicks, M. (2018). Rainfall-induced slope collapse with coupled material point method. *Eng Geol* **239**, 1–12.

Wang, B., Vardon, P. J., Hicks, M. A. & Chen, Z. (2016b). Development of an implicit material point method for geotechnical applications. *Comput Geotech* **71**, 159–167.

Wang, G. & Sassa, K. (2003). Pore-pressure generation and movement of rainfall-induced landslides: effects of grain size and fine-particle content. *Eng Geol* **69**, No. 1-2, 109–125.

6

Conclusions and Recommendations

6.1. CONCLUDING REMARKS

In this thesis, an investigation into the accuracy of the material point method (MPM) was presented, along with developments to make the method more useful in practice. It was demonstrated that basic MPM is able to simulate mechanical behaviour while conserving energy and momentum. Moreover, large deformation problems can be simulated, exhibiting reasonably realistic behaviour. Nevertheless, it was clear that MPM accuracy was far from desired levels, particularly in calculating the stresses. Therefore, further solutions were needed, not only to reduce the well-known numerical inaccuracies, but also to extend the available solutions to more efficient (and typically used) numerical schemes (i.e. from explicit to implicit).

Focusing on limitations of the numerical accuracy of MPM, a comprehensive analysis of the causes was carried out. In addition, several developments were made: (i) the composite material point method (CMPM), a technique which increases the solution domain when recovering stresses in order to improve the accuracy over using linear shape functions; (ii) double mapping (DM) procedures, which improve the accuracy of integration procedures, which has a particular influence on the stiffness matrix used in implicit MPM; and (iii) implicit contact procedures, in which an existing explicit methodology was extended and elaborated for implicit schemes to allow the interaction of bodies.

These improvements were tested against several analytical and numerical solutions, as well as used in simulations of complex geotechnical problems. These verification and test simulations demonstrated the advantages of the new developments, both in terms of the accuracy of the results, and in terms of the computational performance, both of which are valuable factors to consider for numerical simulations. The main achievements and conclusions of the research are summarised as follows.

6.1.1. MPM INACCURACIES AND CAUSES

It was found that MPM suffered from three main inaccuracies: the first (which is mentioned frequently in literature) due to the material points crossing cell boundaries, the second due to inaccurate numerical integration, and the third due to inaccurate stress recovery.

These inaccuracies were investigated for the explicit, implicit and quasi-static MPM variants. It was demonstrated that all of these schemes are broadly able to simulate mechanical and geotechnical problems, returning similar results (in terms of stresses and deformations) while conserving mass and energy. It was, however, also shown that the stresses oscillate, which limits substantially the use of history dependent constitutive models. It was demonstrated that some of these problems can be partially addressed through some minor changes, such as implementing a background stiffness, or by solving problems in terms of incremental stresses rather than total stresses. Nevertheless, these enhancements are neither generally applicable or rigorouos, nor can they fully solve the inaccuracies.

6.1.2. MPM IMPROVEMENTS TO INCREASE ACCURACY

To enhance basic MPM, two techniques were developed: CMPM and DM-G. CMPM improved the calculated material point stresses by using a higher order and larger solution

domain to interpolate material stresses and strains. DM-G improved integration and interpolation by adopting the GIMP method developed previously, which includes a material point domain (allowing it to influence more than one element) and a double mapping procedure which improves the numerical integration by using Gauss point locations. This virtually eliminates cell crossing errors and integration errors. By combining CMPM with DM-G procedures (DM-GC), the accuracy is improved throughout the entire solution.

The enhancement of MPM using DM-GC was demonstrated through axisymmetric and 1D benchmarks problems. Furthermore, the improvements were tested in a geotechnical vertical cutting problem, with good results obtained. It was observed that the mean and deviatoric stress distributions and the stiffness distributions inside the vertical cutting were smooth, even after a considerable deformation. Also, a series of stress path plots showed that the stresses inside the elastic and plastic regions in the vertical cutting do not drastically oscillate (as in standard MPM), but followed a smooth path. Inaccuracies were observed to remain in the regions of the analysis that had substantial plasticity, such as in shear bands.

6.1.3. MPM IMPLICIT CONTACT

A methodology to simulate contact between different bodies was developed and implemented, based on an existing explicit scheme. The method uses equations developed for the explicit scheme to detect contact and calculate contact forces, whilst the velocities computed from Newmark's time scheme are used to update contact forces during the Newton–Raphson iterative procedure. An additional condition based upon the interpartical distance has been added, which makes the contact algorithm mesh independent. Via a number of benchmarks the efficiency of the method was demonstrated. In most cases, the computational time was substantially reduced while keeping the same accuracy as the explicit solution. To demonstrate the geotechnical applicability of the developments, two geotechnical problems were also investigated: (i) a vertical cutting colliding against a rigid wall, and (ii) the penetration of a shallow footing through the soil. Both simulations demonstrated a realistic soil-structure interaction, exhibiting (in the footing problem) results close to the Terzaghi analytical bearing capacity solution.

6.1.4. GEOTECHNICAL SIMULATIONS USING IMPROVED MPM

It was shown that realistic geotechnical simulations could be simulated with the developed method. Two important types of geotechnical problems, i.e. landslides and protection structures, were analysed. These simulations contained complex geotechnical behaviour and involved construction stages, material seperating and re-joining, elasto-plasicity and extremely large deformations.

Due to the use of the contact algorithm, an extensive number of failure mechanisms were allowed to develop. In particular, passive and active failure mechanisms were observed at the soil-structure interface. The sliding and separation of the structures with respect to the soil were captured, as well as the ability of structures to transfer load to different soil volumes. Most typical slope failure mechanisms were observed, including circular, retrogressive and translational failures. In addition, by including the DM-GC technique, a large number of shear bands growing at the soil-structure and soil-boundary interface were able to be captured, rather than the more diffuse failure zones

often observed when using traditional MPM. Finally, through these simulations, it is observed that risk assessment studies can be performed, in which loads and forces acting on structures, run-out distances and overall damages can be assessed.

6.2. RECOMMENDATIONS FOR FURTHER RESEARCH

To further develop the accuracy and practical use of the material point method, further improvements are recommended. These are:

- Further include the deformation of the material point domain in the method. DM-G shows considerable improvement in the accuracy of the simulations. Nevertheless, since this solution uses GIMP SFs to perform mapping and integration procedures, the shape of the material point support domain is important. In this thesis, compression or extension of the support domain was considered, but further deformations, such as rotation and shearing, were ignored. Methods such as CPDI can deal with any sort of distortion of the support domain, indicating that CPDI could be combined with the methods developed here to increase the accuracy of MPM further. Additionally, recent studies have demonstrated that CPDI can be implemented using unstructured meshes, also giving the opportunity of implementing DM-G together with unstructured meshes.

- Large deformation constitutive models need to be further developed and laboratory calibration tests are needed. In this thesis, the von Mises constitutive model was used to simulate every geotechnical problem. The results obtained were realistic, and comparable to analytical solutions where available, but it is evident that more complex constitutive models are needed to represent more accurately complex soil behaviour. Prior to the work contained in this thesis, stress oscillations in MPM meant that there was little chance of accurately using advanced constitutive models, but considering the improvements reached in this thesis, the use of advanced constitutive models is now a possibility.

- The energy conservation behaviour of the contact algorithm needs to be improved. The results obtained with the implicit contact algorithm developed in this thesis were acceptable; similar to the results obtained with the explicit solution and, in most of the cases, with an improvement in the computational time. Nevertheless, it was observed that a drop in energy occurs at the instant of contact. As mentioned, this is attributed to the inconsistency between the internal loads and the contact loads. Since the internal loads resulting from the change of material point stresses during contact are not equal to the contact loads computed from the change of velocity, an inconsistency occurs, which results in a drop of energy. Including the change of internal forces in the formulation to improve the accuracy of the results is not an easy task, since the stress oscillation problem would interfere in the accuracy of the results, and even the improvements presented in this thesis do not solve this problem completely. Nevertheless, it is believed that this enhancement is needed to improve accuracy.

- Include multi-phase material behaviour. The research developed in this thesis uses a single-phase material (i.e. the water and air phases are not considered), which can

be seen as unrealistic since, in nature, most of the soil contains at least one other phase. One of the main disadvantages of including these phases, besides the elaborated formulation, is that the water phase can cause large stress oscillations, leading to highly inaccurate results. Nevertheless, it is believed that the developments in this thesis (and in a possible combination with other techniques to diminish volumetric locking) could reduce such oscillations, allowing the implementation of multi-phase material behaviour.

- Develop efficient parallel computational solutions. It was observed that using the implicit solution scheme, an improvement in the computational time is obtained. Nevertheless, if large domains are simulated with relatively small elements, the computational time increases, taking, in some cases, several days to reach the final solution. This is a consequence of dynamic simulations (made up of many steps) and of the additional mapping steps in MPM. Unfortunately, these simulation times are not feasible in most engineering projects. It is therefore recommended to develop advanced coding structures, such as parallel computing, in which several segments of the codes can be solved simultaneously, thereby reducing the computational time. This is compatible with standard desktop computers, which typically contain several processing cores. To further speed up the computation, GPU programming could be used.

- Ensuring mesh independence. Since MPM codes are based on FEM codes, the same mesh dependency inaccuracies are observed, especially when there is softening in constitutive models. It has been observed that localisations occur during the simulations, and that mesh dependence influences the outcome. Implementation techniques such as regularisation are recommended to address this issue.

A

Appendix A

A

A.1. PLANE STRAIN AND AXISYMMETRIC MATRICES

Figure A.1 shows the isoparametric element and the local coordinates (η, ξ)

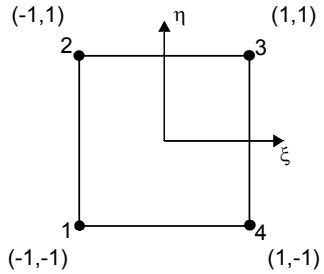

Figure A.1: Isoparametric parent element and coordinates

For plane strain conditions, the four noded element **N**, **B**, and **J** matrices are

$$\mathbf{N} = \begin{bmatrix} N_1 & 0 & N_2 & 0 & N_3 & 0 & N_4 & 0 \\ 0 & N_1 & 0 & N_2 & 0 & N_3 & 0 & N_4 \end{bmatrix} \tag{A.1}$$

$$\mathbf{B} = \begin{bmatrix} \frac{\partial N_1}{\partial x} & 0 & \frac{\partial N_2}{\partial x} & 0 & \frac{\partial N_3}{\partial x} & 0 & \frac{\partial N_4}{\partial x} & 0 \\ 0 & \frac{\partial N_1}{\partial y} & 0 & \frac{\partial N_2}{\partial y} & 0 & \frac{\partial N_3}{\partial y} & 0 & \frac{\partial N_4}{\partial y} \\ \frac{\partial N_1}{\partial y} & \frac{\partial N_1}{\partial x} & \frac{\partial N_2}{\partial y} & \frac{\partial N_2}{\partial x} & \frac{\partial N_3}{\partial y} & \frac{\partial N_3}{\partial x} & \frac{\partial N_4}{\partial y} & \frac{\partial N_4}{\partial x} \end{bmatrix} \tag{A.2}$$

$$[\mathbf{J}] = \begin{bmatrix} \frac{\partial x}{\partial \xi} & \frac{\partial y}{\partial \xi} \\ \frac{\partial x}{\partial \eta} & \frac{\partial y}{\partial \eta} \end{bmatrix} \tag{A.3}$$

where the Cartesian coordinates are defined as

$$x = N_1 x_1 + N_2 x_2 + N_3 x_3 + N_4 x_4 \tag{A.4}$$

$$y = N_1 y_1 + N_2 y_2 + N_3 y_3 + N_4 y_4 \tag{A.5}$$

and

$$\begin{aligned} N_1 &= \frac{1}{4}(1-\xi)(1-\eta);\ N_2 = \frac{1}{4}(1-\xi)(1+\eta); \\ N_3 &= \frac{1}{4}(1+\xi)(1+\eta);\ N_4 = \frac{1}{4}(1+\xi)(1-\eta); \end{aligned} \tag{A.6}$$

where the subscript indicates the node number. Then, the **D** matrix is computed as

$$\mathbf{D} = \frac{E(1-\upsilon)}{(1+\upsilon)(1-2\upsilon)} \begin{bmatrix} 1 & \frac{\upsilon}{1-\upsilon} & 0 \\ \frac{\upsilon}{1-\upsilon} & 1 & 0 \\ 0 & 0 & \frac{1-2\upsilon}{2(1-\upsilon)} \end{bmatrix} \tag{A.7}$$

The elastic relationship between stresses and strains ($\boldsymbol{\sigma} = \mathbf{D}\boldsymbol{\epsilon}$) is

$$\begin{Bmatrix} \sigma_x \\ \sigma_y \\ \sigma_{xy} \end{Bmatrix} = \frac{E}{(1+\nu)(1-2\nu)} \begin{bmatrix} 1-\nu & \nu & 0 \\ \nu & 1-\nu & 0 \\ 0 & 0 & \frac{1-2\nu}{2} \end{bmatrix} \begin{Bmatrix} \epsilon_x \\ \epsilon_y \\ \epsilon_{xy} \end{Bmatrix} \tag{A.8}$$

where the vector of strains ($\boldsymbol{\epsilon} = \mathbf{B}\bar{\mathbf{u}}$) is

$$\begin{Bmatrix} \boldsymbol{\epsilon}_x \\ \boldsymbol{\epsilon}_y \\ \boldsymbol{\epsilon}_{xy} \end{Bmatrix} = \begin{bmatrix} \frac{\partial N_1}{\partial x} & 0 & \frac{\partial N_2}{\partial x} & 0 & \frac{\partial N_3}{\partial x} & 0 & \frac{\partial N_4}{\partial x} & 0 \\ 0 & \frac{\partial N_1}{\partial y} & 0 & \frac{\partial N_2}{\partial y} & 0 & \frac{\partial N_3}{\partial y} & 0 & \frac{\partial N_4}{\partial y} \\ \frac{\partial N_1}{\partial y} & \frac{\partial N_1}{\partial x} & \frac{\partial N_2}{\partial y} & \frac{\partial N_2}{\partial xy} & \frac{\partial N_3}{\partial y} & \frac{\partial N_3}{\partial x} & \frac{\partial N_4}{\partial y} & \frac{\partial N_4}{\partial x} \end{bmatrix} \begin{Bmatrix} \bar{u}_{x,1} \\ \bar{u}_{y,1} \\ \bar{u}_{x,2} \\ \bar{u}_{y,2} \\ \bar{u}_{x,3} \\ \bar{u}_{y,3} \\ \bar{u}_{x,4} \\ \bar{u}_{y,4} \end{Bmatrix} \tag{A.9}$$

The vector of strains using CMPM extended domain (i.e. $\boldsymbol{\epsilon} = \mathbf{B}^2\bar{\mathbf{u}}^{\text{ext}}$) is computed as

$$\begin{Bmatrix} \boldsymbol{\epsilon}_x \\ \boldsymbol{\epsilon}_y \\ \boldsymbol{\epsilon}_{xy} \end{Bmatrix} = \begin{bmatrix} \frac{\partial N_1}{\partial x} & 0 & \cdots & \frac{\partial N_n}{\partial x} & 0 \\ 0 & \frac{\partial N_1}{\partial y} & \cdots & 0 & \frac{\partial N_n}{\partial y} \\ \frac{\partial N_1}{\partial y} & \frac{\partial N_1}{\partial x} & \cdots & \frac{\partial N_n}{\partial y} & \frac{\partial N_n}{\partial x} \end{bmatrix} \begin{Bmatrix} \bar{u}_{x,1} \\ \bar{u}_{y,1} \\ \bar{u}_{x,2} \\ \vdots \\ \bar{u}_{y,n-1} \\ \bar{u}_{x,n} \\ \bar{u}_{y,n} \end{Bmatrix} \tag{A.10}$$

where n is the number of nodes in the extended domain as shown in Figure A.2. Note that the extended domain can be constructed using square arrays of C^2 elements, where $C > 1$.

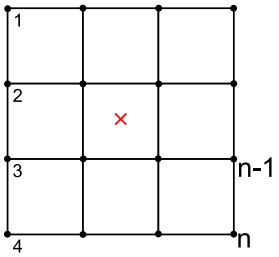

Figure A.2: Extended domain for a material point using an array of 3^2 elements

For axisymmetric conditions, cylindrical coordinates are used, and after integration over one radian the stiffness matrix becomes

$$\mathbf{K} = \sum_{p=1}^{nmp} \mathbf{B}^{axT}(\mathbf{x}_p)\mathbf{D}_p^{ax}\mathbf{B}^{ax}(\mathbf{x}_p)\,|\mathbf{J}|\,\mathrm{Wr}_p \tag{A.11}$$

The element (nodal) internal forces $\mathbf{F}^{\text{int}}$ are

$$\mathbf{F}^{\text{int}} = \sum_{\text{p}=1}^{\text{nmp}} \boldsymbol{\sigma}_{\text{p}}^{\text{ax}} \mathbf{B}^{\text{ax}}(\mathbf{x}_{\text{p}}) \, |\mathbf{J}| \, \text{Wr}_{\text{p}} \tag{A.12}$$

and the element (nodal) external forces $\mathbf{F}^{\text{ext}}$ considering only gravity are

$$\mathbf{F}^{\text{ext}} = \sum_{\text{p}=1}^{\text{nmp}} \rho_{\text{p}} \mathbf{N}^{\text{T}}(\mathbf{x}_{\text{p}}) \mathbf{g} \, |\mathbf{J}| \, \text{Wr}_{\text{p}} \tag{A.13}$$

where

$$\mathbf{B}^{\mathbf{ax}} = \begin{bmatrix} \frac{\partial N_1}{\partial r} & 0 & \frac{\partial N_2}{\partial r} & 0 & \frac{\partial N_3}{\partial r} & 0 & \frac{\partial N_4}{\partial r} & 0 \\ 0 & \frac{\partial N_1}{\partial y} & 0 & \frac{\partial N_2}{\partial y} & 0 & \frac{\partial N_3}{\partial y} & 0 & \frac{\partial N_4}{\partial y} \\ \frac{\partial N_1}{\partial y} & \frac{\partial N_1}{\partial r} & \frac{\partial N_2}{\partial y} & \frac{\partial N_2}{\partial r} & \frac{\partial N_3}{\partial y} & \frac{\partial Nr}{\partial r} & \frac{\partial N_4}{\partial y} & \frac{\partial N_4}{\partial r} \\ \frac{N_1}{r} & 0 & \frac{N_2}{r} & 0 & \frac{N_3}{r} & 0 & \frac{N_4}{r} & 0 \end{bmatrix} \tag{A.14}$$

$$\mathbf{D}^{\text{ax}} = \frac{\text{E}(1-\upsilon)}{(1+\upsilon)(1-2\upsilon)} \begin{bmatrix} 1 & \frac{\upsilon}{1-\upsilon} & 0 & \frac{\upsilon}{1-\upsilon} \\ \frac{\upsilon}{1-\upsilon} & 1 & 0 & \frac{\upsilon}{1-\upsilon} \\ 0 & 0 & \frac{1-2\upsilon}{2(1-\upsilon)} & 0 \\ \frac{\upsilon}{1-\upsilon} & \frac{\upsilon}{1-\upsilon} & 0 & 1 \end{bmatrix} \tag{A.15}$$

where $\mathbf{B}^{\text{ax}}$ refers to the axisymmetric strain-displacement matrix, $\mathbf{D}^{\text{ax}}$ refers to the stress-strain matrix, and r_{p} is the radial distance between the sampling point and the axisymmetric axis. In both cases (plane strain and axisymmetric conditions) the matrix of SF $\mathbf{N}$ remains the same.

A.2. ANALYTICAL AXISYMMETRIC SOLUTION

The radial, tangential and axial stress distributions (σ_r, σ_θ and σ_y, respectively) in the wall of a hollow cylinder at a radius r from the cylinder axis are computed as

$$\sigma_r = \frac{A}{r^2} + 2\Psi \tag{A.16}$$

$$\sigma_{theta} = -\frac{A}{r^2} + 2\Psi \tag{A.17}$$

$$\sigma_y = 4\nu\Psi \tag{A.18}$$

where A and Ψ are constants given by

$$A = 2(1-2\nu)\Psi r_e^2 \tag{A.19}$$

$$\Psi = \frac{EA_1}{2(1+\nu)(1-2\nu)} \tag{A.20}$$

in which A_1 is a function of the boundary conditions. For a cylinder that is fxed at the external boundary (r_e) and loaded at the internal boundary by a pressure p_s,

$$A_1 = \frac{p_s(1+\nu)(1-2\nu)}{r_e^2 E\left(-\frac{(1-2\nu)}{r_i^2} - \frac{1}{r_e^2}\right)} \tag{A.21}$$

B

APPENDIX B

B.1. DOUBLE MAPPING PROCEDURES

Table B.1 summarises the steps to perform stiffness integration using DM techniques (DM-MPM and DM-G). It is highlighted that both the DM and DM-G techniques follow the same steps. Making the following minor modifications, it is possible change between DM and DM-G: (i) Loop 3 loops 'over the material points affecting the element', which can be either all material points in the element (cmp) or all material points with support domain in the element (smp), for DM and DM-G respectively, (ii) the nodal shape function $\bar{\mathbf{H}}_i$ represents N_i or S_{ip^*}, for the DM and DM-G respectively, and (iii) the material point weight value $\bar{W}$ represents W^* or W, for DM and DM-G respectively. Summarising, SM uses cmo, N_i and W^*, whereas DM-G uses smp, S_{ip^*} and W.

Table B.1: Summary of steps followed to perform DM stiffness integration

$\mathbf{K}_v$ = zero
Loop 1: over all elements
  $\mathbf{K}_{el}$ = zero
  Loop 2: over the elements Gauss points (ngauss)
    $\mathbf{D}_g$ = zero
    Evaluate $\mathbf{N}(\mathbf{x}_g)$ = zero
    Evaluate $\mathbf{B}_g$
    Loop 3: over the material points affecting the element
      Compute $\mathbf{D}_p$
      Evaluate $\bar{\mathbf{H}}(\mathbf{x}_p)$
      $\mathbf{D}_g = \mathbf{D}_g + \mathbf{D}_p \sum_{i=1}^{nn} \mathbf{N}_i(\mathbf{x}_g)\bar{\mathbf{H}}_i(\mathbf{x}_p)$
    END Loop 3
    $\mathbf{K}_{el} = \mathbf{K}_{el} + \mathbf{B}_g^T \mathbf{D}_g \bar{W} \mathbf{B}_g |\mathbf{J}| W^{FE}$
  END Loop 2
  Assemble $\mathbf{K}_{el}$ into $\mathbf{K}_v$
END Loop 1

In Table B.2, the stress recovery steps are shown considering CMPM. It is highlighted that all matrices are related to the patch used, so are larger than in regular MPM. For example, for 4 noded elements the patch is 4x4 nodes, instead of 2x2.

To demonstrate the computational performance of the DM-G algorithm (which has a higher computational cost when compared to DM), a series test were conducted on square meshes, with the results presented in Figure B.1. The test consisted of computing the stiffness of meshes made up of 50, 75, 100, 150, and 200 elements per side, with each element filled with 4 equally distributed MPs. Each stiffness cycle was computed 200 times to obtain an accurate mean value of the time taken. In Figure B.1, the relationship between computational time using DM-G and regular MPM is plotted as a function of the number of equations. It is observed that the relationship is almost constant, with

DM-G taking about 50% longer than regular MPM. However, the overall increase of computational time for the problem studied is close to 5%, although this is dependent on the solver and characteristics of the problem solved.

Table B.2: Stress recovery steps using CMPM

Loop 1: over all elements
  Construct $\Delta\bar{\mathbf{u}}^{\text{ext}}$
  Loop 2: over all the material points inside the element
    Evaluate $\nabla\mathbf{N}^{\text{C}}_{\text{local}}$ - (using the derivatives of Eq. 3.11 or Eq. 3.12)
    Evaluate $\left[\mathbf{J}^{\text{mp}}\right] = \nabla\mathbf{N}^{\text{C}}_{\text{local}}\mathbf{x}^{\text{C}}$
    Compute $\nabla\mathbf{N}^{\text{C}}_{\text{local}} = \left[\mathbf{J}^{\text{mp}}\right]^{-1}\nabla\mathbf{N}^{\text{C}}_{\text{local}}$
    Construct $\mathbf{B}^{\text{C}}(\mathbf{x}_{\text{p}})$
    Compute $\Delta\boldsymbol{\sigma}_{\text{p}}$ - (Eq. 3.17)
    IF ($F_{\text{yield}} > 0$) THEN
      Use FEM procedures to compute plastic strains and return stresses to the yield surface
    END IF
  END Loop 2
END Loop 1

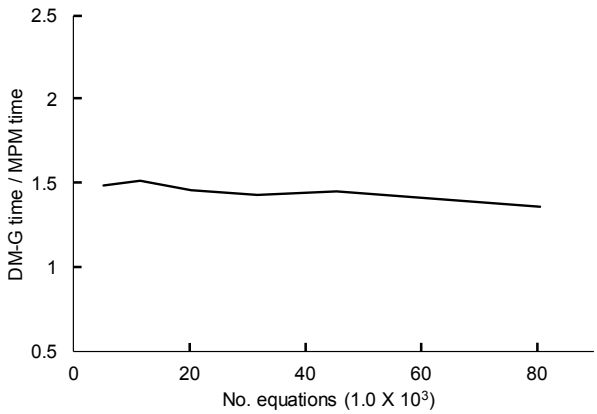

Figure B.1: Relationship between the computational times using DM-G and typical MPM

NOTATION

ACRONYMS

SB	Shear band
CDPI	Convected domain particle interpolation
CMPM	Composite material point method
DDMP	Dual domain material point
DM	Double mapping
DM-C	Double mapping using CMPM
DM-G	Double mapping using GIMP shape functions
DM-GC	Double mapping using GIMP shape functions and CMPM
FEM	Finite element method
FE	Finite element
FV	Failure volume
GIMP	Generalized interpolation material point
GM	Gauss mapping
KE	Kinetic energy
MP	Material point
MPM	Material point method
PE	Potential energy
SD	Material point support domain
SE	Strain energy
SF	Shape function
TE	Total energy
UL	Updated Lagrangian

LATIN SYMBOLS

$\mathbf{a}$	Acceleration vector
a_p	Material point acceleration
$\bar{\mathbf{a}}$	Vector of nodal accelerations
A	Constant derived from the axisymmetric solution
A_1	Constant derived from the axisymmetric boundary condition

$\mathbf{b}$	Body forces
$\mathbf{B}$	Strain-displacement matrix
$\mathbf{B^{ax}}$	Strain-displacement matrix for axisymmetric domain
$\mathbf{B^{C}}$	Strain-displacement matrix for CMPM patch
$\mathbf{B}_{\mathrm{d}}$	Elastic matrix at the Gauss point
$\mathbf{B}_{\mathrm{i}}$	Elastic matrix at the node i
$\mathbf{B}_{\mathrm{p}}$	Elastic matrix at the sampling point
$\mathbf{B}_{\mathrm{p}}^{\mathrm{ax}}$	Elastic matrix at the sampling point for axisymmetric domain
bod	Bodie
$\mathrm{c_p}$	Soil peak cohesion
$\mathrm{c_r}$	Soil residual cohesion
C	Subscript denotating combined values
cmp	Current number of material points in the element
d	Distance between the element boundary and the axisymmetric internal boundary
$\mathrm{d_{min}}$	Minimum distance requited to activate contact
$\mathrm{d_{max}^S}$, $\mathrm{d_{max}^S}$	Surface and embeded wall maximum displacement
$\mathbf{D}$	Material elastic matrix
$\mathbf{D}_{\mathrm{p}}$	Material point elastic matrix
E	Young's modulus
elmp	Material points affecting an element
$\mathbf{F}^{\mathrm{ext}}$	Vector of external nodal forces
$\mathrm{F}^{\mathrm{fric}}$	Vector of nodal frictional forces
$\mathbf{F}^{\mathrm{int}}$	Vector of internal nodal forces
$\mathrm{F}_{\mathrm{mag}}^{\mathrm{int}}$	Internal nodal force magnitude
F^{nc}	Vector of nodal contact forces
$\mathrm{F}^{\mathrm{stick}}$	Trial vector of nodal frictional forces
$\mathrm{F_{VM}}$	Von Mises yield function
$\mathrm{F}_{\mathrm{x}}^{\mathrm{int}}$	Nodal internal force in the horizontal direction
$\mathrm{F}_{\mathrm{y}}^{\mathrm{int}}$	Nodal internal force in the vertical direction
$\mathrm{F_{yield}}$	Yield function
$\mathbf{g}$	Gravity vector
H	Height of the vertical cut benchmark
$\bar{\mathbf{H}}$	Matrix of shape functions, representing either $\mathbf{N}$ or matrix of $\mathrm{S}_{\mathrm{ip}}^{*}$

H_s	Softening modulus
i	Subscript representing nodal values
ic	Subscript representing contact node
$\mathbf{J}$	Jacobian matrix
$\mathbf{J}^{mp}$	Jacobian matrix computed using material points shape functions derivatives
$\|\mathbf{J}\|$	Jacobian matrix determinant
k	Iteration number
$\mathbf{K}$	Stiffness matrix
$\mathbf{K}_{el}$	Element stiffness matrix
K_{mag}	Stiffness matrix magnitude
K_x	Diagonal entry of the stiffness matrix corresponding to the horizontal degree of freedom
K_y	Diagonal entry of the stiffness matrix corresponding to the vertical degree of freedom
$\mathbf{K}_v$	Global stiffness matrix
K_0	Coefficient of earth pressure at rest
lp	Half of the material point support domain
L	Length of the vertical cut benchmark
$\mathbf{M}$	Mass matrix
m_g	Mass concentrated at the central Gauss position
m_p	Material point mass
M_x	Diagonal entry of the mass matrix corresponding to the horizontal degree of freedom
M_y	Diagonal entry of the mass matrix corresponding to the vertical degree of freedom
$\bar{\mathbf{n}}$	Normal direction vector of one body
$\mathbf{n}$	Normal direction vector considering neighbouring bodies
N	Shape function
$\mathbf{N}$	Matrix of shape functions
N_i	Nodal shape function
ngauss	Number of Gauss points in the element
nmp	Number of material points inside an element
nn	Number of nodes
$\mathbf{N}^C_{global}$	Matrix of global CMPM shape functions
$\mathbf{N}^C_{local}$	Matrix of local CMPM shape functions

N^i	CMPM shape functions, where i is the C-continuity
$\mathbf{N}^i$	Matrix of CMPM shape functions, where i is the C-continuity
omp	Original number of material points in the element
p_s	Applied tric benchmark
r	Distance between the cylinder axis and any point inside the cylinder wall
r_e	Outer boundary of the axisymmetric benchmark
r_i	Internal boundary of the axisymmetric benchmark
r_{mp1}	Radial position of a material point at the boundary of the axisymmetric benchmark
r_p	Radial position of a material point
s	Internal boundary of the axisymmetric benchmark
s^s	Traction at the surface
s_p^s	Material point traction force
s_p	Soil peak shear strength
s_r	Soil residual shear strength
smp	Number of material points with a support domain inside an element
S_{ip}	GIMP shape functions
S_{ip}^*	Local GIMP shape functions
s_u	Soil shear strength
t	Superscript denoting value at current time step
tol	Newton-Raphson tolerance
t_c	Instant of contact
$t + \Delta t$	Superscript denoting value at next time step
u	Virtual displacement
$\bar{\mathbf{u}}$	Vector of nodal displacements
$\bar{\mathbf{u}}^{ext}$	Vector of nodal displacements in the extended domain using CMPM
$\mathbf{v}$	Velocity vector
$\bar{\mathbf{v}}$	Vector of nodal velocities
${}^*\mathbf{v}$	Corrected nodal velocity vector
V	Body volume
V_p	Material point volume
$\mathbf{v}_p$	Material point velocity

W	Material point integration
W^{FE}	Weight associated with the Gauss point
W^*	Modified material point integration weight
$\bar{W}$	Material point weight, representing either W or W^*
$\mathbf{x}^C$	Nodal coordinates of the CMPM patch
$\mathbf{x}^g$	Gauss position
$\mathbf{x}^p$	Material point position
Y	Yield function

GREEK SYMBOLS

α	Newmark time stepping parameter
χ_p	Characteristic function
δ	Newmark time stepping parameter
δu	Test function in terms of displacement
$\delta\bar{\mathbf{u}}$	Incremental displacement
$\delta\epsilon$	Test function in terms of strains
$\delta\bar{\mathbf{v}}$	Vector of nodal test function velocities
δ_{mpl}	Material point domain
Δq	Incremental deviatoric stress
Δp_s	Incremental applied pressure on the boundary of the axisymmetric benchmark
Δr	Mesh radial dimension for the axisymmetric domain
$\Delta\boldsymbol{\sigma}_p$	Stress increment vector at the material point
$\Delta\sigma_m$	Incremental mean stress
Δt	Time step
$\Delta\bar{\mathbf{u}}$	Vector of incremental nodal displacement
Δy	Mesh vertical dimension
Δx	Mesh horizontal dimension
$\boldsymbol{\epsilon}$	Vector of incremental strain
$\boldsymbol{\epsilon}^e$	Vector of incremental elastic strain
$\boldsymbol{\epsilon}^p$	Vector of incremental plastic strain
$\boldsymbol{\epsilon}_p$	Vector of material point incremental strain
γ_s	Soil unit weight
γ_w	Wall unit weight
Γ	Body surface
λ	Plastic strain increment
μ	Friction coefficient

η	Vertical position in local coordinates
ν	Poisson's ratio
ρ	Density
ρ_p	Material point density
Ψ	Constant derived from the axisymmetric solution
$\boldsymbol{\sigma}$	Cauchy stress tensor
σ_A	Analytical radial stress
$\boldsymbol{\sigma}^{ax}$	Cauchy stress tensor for axisymmetric domain
σ_L	Stress inside a linear axisymmetric element
σ_Q	Stress inside a quadratic axisymmetric element
σ_θ	Tangential stress
σ_r	Radial stress
σ_y	Vertical stress
σ_{xy}	shear stress
Ω	Simulation domain
Ω_p	Material point support domain
ξ	Horizontal position in local coordinates

ACKNOWLEDGEMENTS

It has been, to this date, almost five years since I began pursuing my PhD dissertation. It has been challenging to reaching this point but, thanks to the people around me, the journey has been enlightening, formative and fun.

First of all, I would like to thank my promotors, Prof Michael A. Hicks and Dr Philip J. Vardon, from whom I cannot express enough gratitude for their guidance and support during my studies. Prof. Hicks gave me his trust and the opportunity to pursue my doctoral studies. He has been truly patient with me (especially during those writing days), and learning from his experience has been priceless. Dr Vardon has been an exceptional leader. He has always guided me in the right direction, and his extensive knowledge of my PhD topic enriched my work substantially. I am convinced that my development as a researcher would not be the same without either of them; I could not ask for better supervisors.

To the people with whom I have shared many moments of my life during these years, I cannot express enough how much I appreciate every one of you. My colleagues are such remarkable people. You contributed so much to my research through advice, brainstorming, chats and jokes - activities which are highly recommendable for relaxing and allowing new ideas to bloom. The people I met outside of my academic circle is just fantastic. My Latin friends have become my second family. We have shared many experiences, and I know that you are trustworthy people whom I can count on at all times. My dancing friends are also worth a special mention. Some of you have become close friends, and we have created lots of good memories together.

Aunque lejos de aquí, mi familia también ha sido parte fundamental durante mis estudios. Quiero agradecerle a mi mamá por todo el apoyo que me ha dado, no solo durante mis estudios, sino que durante toda mi vida. Tú eres la persona más importante que tengo, y no hay palabras suficiente para decirte lo mucho que te quiero y necesito. Mi hermano, aunque no somos dados a platicar mucho, es claro que el cariño que nos tenemos es bastante. Además, aunque más pequeño que yo, también lleva un vida de grandes logros, lo cual me motiva a seguir creciendo. Quisiera también dedicarle mi trabajo a mi abuelo, Don Guillermo, que aunque la vida se lo llevo antes de que pudiera terminar mi doctorado, sé que sigue cuidándome desde otro lugar.

Infine, ma non per importanza, voglio confessare che la mia piu' grande fonte di forza per proseguire i miei studi, il mio lavoro e addirittura rimanere nei Paesi Bassi, spilla da una straordinaria persona a cui sono eternamente grato, Grazia. Solo ora sono circa due anni e mezzo dal nostro primo appuntamento e da allora sei stata parte fondamentale nella mia vita. Tu eri lí con me nei momenti piú tristi e piú felici della permanenza a Delft, donandomi sentito supporto e portando gioia nella mia vita. La pazienza che hai avuto per me é straordinaria; non avrei potuto chiedere una persona migliore con cui condividere le mie giornate.

CURRICULUM VITÆ

José León GONZÁLEZ ACOSTA

21-01-1987 Born in Ensenada, Baja California, México.

EDUCATION

2014–2019 Ph.D Candidate in Geotechnical Engineering
Technische Univeristeit Delft, the Netherlands
Thesis: Investigation of MPM inaccuracies, contact simulation and its implementation in geotechnical problems
Promotor: Prof. dr. M. (Michael) A. Hicks
Promotor: Dr. P. (Philip) J. Vardon

2011–2013 Master of Science, Geotechnical Engineering
Universidad Nacionál Autónoma de México, México

2005–2010 Bachelor's Degree, Civil Engineering
Universidad Autónoma de Baja California, México

WORK

2020–current	Geo-Engineering Consultant GustoMSC, Schiedam
2016–current	Ph.D Candidate Geo-Engineering Delft University of Technology, Delft
2014–2015	Geo-Engineering Consultant Bowerbird Engineering, México
2012–2014	Research Assistant UNAM Engineering Institute, México
2010–2011	Construction Manager Proyectos Integrales de Baja California, México

List of Publications

Journal Publications

- González Acosta, J.L., Vardon, P.J. & Hicks, M.A. (2020). An implicit contact technique for the material point method. *Submitted for review.*

- González Acosta, J.L., Vardon, P.J. & Hicks, M.A. (2020). Study of landslides and the interaction with structures using implicit MPM. *Submitted for review.*

- González Acosta, J.L. Vardon, P.J. Remmerswaal, G. & Hicks, M.A. (2020). An investigation of stress inaccuracies and proposed solution in the material point method. *Computational Mechanics* **65**(2), 555-581.

- González Acosta, J.L., Vardon, P.J. & Hicks, M.A. (2017). Composite material point method (CMPM) to improve stress recovery for quasi-static problems. *Procedia Engineering* **175**, 324-331.

Conference Publications

- González Acosta, J.L. Zheng, X. Vardon, P.J. Hicks, M.A. & Pisanò, F. (2019). On stress oscillation in MPM simulations involving one or two phases. *Proceedings of the Second International Conference on the Material Point Method for Modelling Soil-WaterStructure Interaction*; 135-139.

- González Acosta, J.L. Vardon, P.J. Hicks, M.A. & Pantev, I.A. (2018). The use of MPM to estimate the behaviour of rigid structures during landslides. *NUMGE 2018*; 651-656.

- Remmerswaal, G. Vardon, P.J. Hicks, M.A. & González Acosta, J.L.. (2017) Development and implementation of moving boundary conditions in the Material Point Method. *ALERT Geomaterials*; 28-29.

- González Acosta, J.L., Vardon, P.J. & Hicks, M.A. (2017). An evaluation of MPM, GIMP and CMPM in geotechnical problems considering large deformations. *Proceedings of the 15th International Conference of the International Association for Computer Methods and Advances in Geomechanics. IACMAG 2017.*